FUNCTIONAL MOLECULAR IMAGING WITH DNP-^{13}C-MRSI

Nicholas Perkons

A DISSERTATION

in

Bioengineering

Presented to the Faculties of the University of Pennsylvania

in

Partial Fulfillment of the Requirements for the

Degree of Doctor of Philosophy

2020

Supervisor of Dissertation

Terence P. Gade, MD, PhD
Assistant Professor of Radiology

Co-Supervisor of Dissertation

Mitchell Schnall, MD, PhD
Eugene P. Pendergrass Professor of Radiology
Chairman, Department of Radiology

Graduate Group Chairperson

Yale Cohen, MD, PhD
Professor of Otorhinolaryngology: Head and Neck Surgery

Dissertation Committee

Mitchell Schnall, MD, PhD
Eugene P. Pendergrass Professor of Radiology
Chairman, Department of Radiology

David Mankoff, MD, PhD
Gerd Muehllehner Professor of Radiology
Vice Chairman of Research, Department of Radiology

Lewis Chodosh, MD, PhD
Perelman Professor of Cancer Biology
Chairman, Department of Cancer Biology

Andrew Tsourkas, PhD
Professor of Bioengineering

FUNCTIONAL MOLECULAR IMAGING WITH DNP-^{13}C-MRSI

COPYRIGHT

2020

Nicholas Perkons

This work is licensed under the
Creative Commons Attribution-
NonCommercial-ShareAlike 3.0
License

To view a copy of this license, visit

https://creativecommons.org/licenses/by-nc-sa/3.0/us/

This thesis is dedicated to my parents, Rainer & Patricia Perkons.

ACKNOWLEDGMENT

First and foremost, I wish to acknowledge my advisor and mentor, Dr. Terence Gade, for his support of my development as a physician-scientist. His mentorship, optimism, and enthusiasm enabled my success in graduate school.

I wish to acknowledge my labmates in the Penn Image Guided Interventions Lab for their expertise and friendship, which was invaluable throughout my training. Thank you especially to Dr. Stephen Hunt, Dr. Gregory Nadolski, Dr. Dan Ackerman, Dr. Ryan Kiefer, Dr. Elliot Stein, Dr. David Tischfield, Dr. Kelley Weinfurtner, Michael Noji, Enri Profka, Michael Mercadante, Omar Johnson, Gabrielle Pilla, Kamiel Saleh, Chike Nwaezapu, Jen Crainic, and Wuyan Li. Additionally, I wish to acknowledge members of the Departments of Cancer Biology and Radiology for their mentorship and expertise, in particular: Dr. Celeste Simon, Dr. Rahim Rizi, Dr. Anthony Mancuso, Dr. Stephen Kadlecek, Dr. Donita Brady, Dr. Stephen Pickup, Dr. Mehrdad Pourfathi, and Dr. Sarmad Siddiqui. Thank you as well to the staff of the Medical Scientist Training Program—in particular Dr. Skip Brass, Dr. Dennis Kolson, Maggie Krall, David Bittner, Maura Tucker, and Maureen Kirsch—for helping me to integrate my medical and graduate training.

I wish to extend my sincere gratitude to members of my thesis committee—Dr. Mitchell Schnall, Dr. Lewis Chodosh, Dr. David Mankoff, and Dr. Andrew Tsourkas—for their insights and recommendations.

Lastly, I wish to acknowledge the love and support of my friends and family. Thank you—in particular Michelle, Steph, Mom, and Dad—for serving as a constant source of reason, encouragement, and motivation.

ABSTRACT

FUNCTIONAL MOLECULAR IMAGING WITH DNP-^{13}C-MRSI

Nicholas Perkons

Terence P. Gade, MD, PhD

Functional molecular imaging facilitates non-invasive tissue evaluation for the distinction of pathology from physiology on the basis of spatiotemporal variation in probe accumulation and conversion. Dynamic nuclear polarization (DNP) modifies the energy distribution of stable isotopes, including ^{13}C, enhancing available signal for magnetic resonance spectroscopic imaging (MRSI), an emerging functional molecular imaging technique. The guiding hypothesis of this compendium is that clinical adoption of DNP-^{13}C-MRSI for disease assessment and response evaluation in cancer will be accelerated by tailoring probe selection to the biology of the target disease. Genetic screening with CRISPR-Cas9 served as a high-throughput tool to identify disease-specific vulnerabilities in cancer according to gene dependency, informing DNP-^{13}C-MRSI probe selection based upon the relative essentiality of probe-specific metabolic enzymes. Subsequent investigations in an autochthonous rodent model of hepatocellular carcinoma (HCC) permitted study of intratumoral metabolism in a manner representative of human disease. Genetic screening identified lactate dehydrogenase (LDH) as a therapeutic vulnerability of HCC; DNP-^{13}C-MRSI with pyruvate quantified intratumoral LDH activity and predicted efficacy of LDH inhibition. Additionally, DNP-^{13}C-MRSI with pyruvate predicted efficacy of

transarterial embolization, a locoregional therapy for HCC, demonstrating enhanced sensitivity to tumor perfusion and persistent viability relative to conventional imaging approaches. To address concerns pertinent to clinical translation of quantitative DNP-^{13}C-MRSI of tumor metabolism, the significance of probe dose and persistence within the body were experimentally investigated. The presented precision imaging approach provides a framework for personalizing therapy selection and evaluating its efficacy non-invasively. Beyond demonstrating a theranostic imaging strategy for management of HCC, this body of work establishes a paradigm for functional metabolic imaging of metabolic diversity in cancer with DNP-^{13}C-MRSI.

TABLE OF CONTENTS

ACKNOWLEDGMENT IV

ABSTRACT V

LIST OF TABLES IX

LIST OF ILLUSTRATIONS X

CHAPTER 1: INTRODUCTION 1

1.1: Overview 1
1.2: Significance 1
1.3 Thesis Organization 3
1.4: References 6

CHAPTER 2: AN INTRODUCTION TO NUCLEAR MAGNETIC RESONANCE AND HYPERPOLARIZATION 7

2.1: Introduction 7
2.2: Principles of nuclear magnetic resonance 7
2.3: Magnetic resonance spectroscopy 10
2.4: Magnetic resonance imaging 11
2.5: Hyperpolarization of ^{13}C by dynamic nuclear polarization 13
2.6: DNP-[1-^{13}C]-pyruvate 17
2.7: Pulse sequences 18
2.8: Conclusion 20
2.9: References 21

CHAPTER 3: GENOME EDITING APPLICATIONS 23

3.1: Introduction 23
3.2: Background 23
3.3: Fundamentals of CRISPR-Cas9 genome editing 24
3.4: CRISPR-enabled scientific advances 27
3.5: Implications for Interventional Radiology 28
3.6: Implications for Molecular Imaging with DNP-^{13}C-MRSI 30
3.7: Conclusion 31
3.8: References 33

CHAPTER 4: FUNCTIONAL GENETIC SCREENING ENABLES THERANOSTIC MOLECULAR IMAGING IN CANCER 35

4.1: Introduction 35
4.2: Abstract 35
4.3: Introduction 36
4.4: Results 37
4.5: Discussion 42
4.6: Methods 44
4.7: Supplemental Figures 52
4.8: Supplemental Tables 53
4.9: References 62

CHAPTER 5: DNP-^{13}C-MRSI QUANTIFICATION CONSIDERATIONS 64

5.1: Introduction 64
5.2: Functional molecular imaging background 64
5.3: Ensuring accurate quantification of DNP Images 65
5.4: Standardizing delivery of the DNP agent 68
5.5: Fidelity of DNP Assessment to Biology: Background 69
5.6: Fidelity of DNP Assessment to Biology: Methods 71
5.7: Fidelity of DNP Assessment to Biology: Results 74
5.8: Fidelity of DNP Assessment to Biology: Conclusions 82
5.9: References 86

CHAPTER 6: HYPERPOLARIZED METABOLIC IMAGING DETECTS LATENT HEPATOCELLULAR CARCINOMA DOMAINS SURVIVING LOCOREGIONAL THERAPY 88

6.1: Introduction ... 88
6.2: Abstract ... 88
6.3: Introduction ... 89
6.4: Results ... 91
6.5: Discussion ... 102
6.6: Materials and Methods ... 106
6.7: Supplementary Figures ... 119
6.8: References ... 120

CHAPTER 7: CONCLUSIONS & FUTURE INVESTIGATIONS 123

7.1: Conclusions ... 123
7.2: Future Investigations ... 124

APPENDIX 1: ELECTROLYTIC ABLATION ENABLES CANCER CELL TARGETING THROUGH PH MODULATION 126

A1.1: Introduction ... 126
A1.2: Abstract ... 126
A1.3: Introduction ... 127
A1.4: Results ... 130
A1.5: Discussion ... 140
A1.6: Methods ... 143
A1.7: Supplementary Figures ... 149
A1.8: References ... 150

LIST OF TABLES

Table 2.1 Chemical shifts of frequently studied 13C nuclei[7]. *11*

Table 4.S1 Differentially essential genes by cancer type. *53*
This table, organized by cancer type, includes: (1) the top five differentially essential genes in each cancer type, (2) imaging-associated differentially essential genes (where $p<0.0005$), (3) DNP-probes associated with imaging genes identified in (2) as described by supplementary tables 2 and 3, and (4) identifies novel potential protein-probe pairs among genes listed in (1) when no imaging associated genes were identified in (3). Differentially essential genes must meet two criteria: (1) the mean CERES score for the cancer type must be < 0 and (2) the mean CERES score must be statistically less than that of all other cancer types studies ($p<0.0005$). *: HCC is a subset of liver cancers.

Table 4.S2 DNP probes used to measure metabolic flux. *54*
Each entry in this table consists of a distinct pair of parent and child metabolites, interconverted by the listed enzyme in a manner that has previously been measured (either directly or indirectly) by the DNP agent listed.

Table 4.S3 Paired list of proteins and affiliated DNP-probes that have been used to measure flux. *58*
This table, organized alphabetically, provides a list of genes, all of which are enzymes, whose flux has been measured by the listed DNP-probe (either directly or indirectly), according to the data provided in Table 4.S2.

Table A1.1 Temperature measurements following electrolytic ablation reveal a temperature-independent mechanism of action *132*
Temperature measurements were made immediately following ablation at four sites surrounding the two electrodes (Figure A1.2F).

Table A1.2 Electrolytic ablation performed with differing buffering capacities reveals pH-dependent viability boundaries surrounding the two electrodes *137*
The viability boundary for each experimental condition was calculated by determining the average pH along the boundary of an ellipse fitted to the viability images analyzed for each condition. pH below the level achieved at anode viability boundary or above the level achieved at the cathode viability boundary was found to induce cell death in the encapsulation assay.

LIST OF ILLUSTRATIONS

Figure 2.1 Measurement of NMR by Isaac Rabi in lithium chloride. (Reproduced with permission from [3]) 9

Figure 2.2 Schematic of how the first MRI was generated by Paul Lauterbur in 1973. (Reproduced with permission from [8]) 12

Figure 2.3 DNP 13C probes, their intermediates, and metabolic pathways they can facilitate measurement of. 16

Figure 2.4 Schematic of the interconversion of pyruvate, lactate, and alanine by ALT and LDH after hyperpolarization of [1-13C]-pyruvate. Yellow circles represent the 1-C in each molecule that retains the hyperpolarized label. 17

Figure 2.5 Pulse sequence diagram for FID-CSI, as reproduced in accordance with a Creative Commons CC BY license as adopted from [27]. 19

Figure 2.6 EPSI pulse sequence diagram with k-space dimensionality of 12 x 16 x 1 x 64 (n_x x n_y x n_z x n_{points}). 20

Figure 3.1 CRISPR-Cas9 genome editing enables sequence-specific modification. (A) Cas9-sgRNA complex scans the genome for a PAM-site in proximity to a sequence complementary to the sgRNA. (B) Following strand separation, PAM-dependent Cas9 endonuclease activation and DSB formation ensues. The spacer motif of the sgRNA (*) is complementary to the protospacer of the target DNA (#). (C) These DSBs can subsequently be repaired through either NHEJ or HDR. NHEJ involves error-prone ligation may yield small insertions or deletions. HDR involves introduction of a donor template with sequence complementarity (dashed lines) to the regions flanking the DSB, which enables sequence modification by incorporation of this template into the genome. 26

Figure 3.2 CRISPR enables translational screening approaches that guide therapy selection. Patient cells taken from biopsy and expanded in culture can be evaluated for dependencies with pooled screening approaches using thousands of sgRNAs that leverage CRISPR-Cas9 technology. In vivo models of patient derived disease can be prepared with patient derived xenografts where these in vitro dependencies can be confirmed, thereby guiding therapy selection. 30

Figure 4.1 Functional genetic screening enables simultaneous selection of therapeutic targets and imaging probes. 38
A. Schematic depicting metabolic pathways that can be analyzed with DNP probes. Purple nodes correspond to previously polarized probes. Pink nodes correspond to intermediates that have either been (i) directly visualized after injection of a DNP probe or (ii) have not been directly identified but precede a downstream intermediate that has been directly visualized. Yellow nodes correspond to metabolites that may serve as future molecular imaging probes, as suggested by the data provided in Supplementary Table 1. Dashed lines correspond to an enzyme or group of enzymes connecting DNP probes and/or intermediates. Colored semi-circles correspond to cancer types that may be imaged with a given DNP probe, as described in Table 4.S1. Figure 4.S1 situates this network of probes in the broader metabolome. B. Table highlighting the top five differentially essential genes in 20 HCC lines, when compared to other cancer types in the DepMap 19Q3 dataset. C. Dot plot depicting the relative essentiality of LDHA in different tumors types (as annotated in the DepMap 19Q3 dataset) based upon CERES score. Individual dots represent unique cell lines (n=625). Blue dots highlight HCC cell lines (n=20). Dark lines depict the median CERES score within tumor groups. D. Schematic illustrating the metabolism of DNP-[1-13C]-pyruvate by LDH and ALT to DNP-[1-13C]-lactate and DNP-[1-13C]-alanine, respectively.

Figure 4.2 DNP-13C-MRSI quantifies intra-tumoral LDH activity in vivo 40
A. DNP-MRS images following injection of hyperpolarized 1-13C-pyruvate enable the quantification of metabolism before (i-iv) and after (v-vii) administration of an LDHi. Panels i and v display spectra re-constructed from each voxel after EPSI overlaid on to T2W 1H images. Panels ii-iv and vi-viii display parametric maps of intratumoral pyruvate, lactate and alanine signals before and after LDHi. These data demonstrate an increase in intratumoral

pyruvate, decrease in intratumoral lactate, and increase in intratumoral alanine after LDHi. B. Stacked spectra demonstrate the evolution of intratumoral pyruvate (170.4 ppm), lactate (183.35 ppm), and alanine (176.5 ppm) before (i) and after (ii) LDHi, again demonstrating a marked reduction in lactate formation. The inserts in the upper-right correspond to integrals of each metabolite peak. C. Bar graph of changes in measured intratumoral metabolite ratios following LDHi administration, including: ↑pyruvate-to-total carbon (n=9, p<0.01), ↓lactate-to-total carbon (n=9, p<0.001), ↑alanine-to-total carbon (n=9, p<0.05), ↓lactate-to-pyruvate (n=9, p<0.01), ↑alanine-to-pyruvate (n=9, p<0.05) and ↑alanine-to-lactate (n=9, p<0.01).

Figure 4.3 LDHi slows HCC growth, as predicted by DNP-[1-13C]-pyruvate metabolism *41*
A. LDHi administration slowed tumor growth, leading to an increase in doubling time of these tumors (n=9, p<0.01). B. Bar graphs demonstrating dose-dependent tumor growth delay following LDHi, (n=6 at 10 mg/kg and n=3 at 20 mg/kg, p<0.05). C. Table showing the dependence of the tumor growth delay on the amount of Alanine measured after LDHi using a generalized linear model (n=9, p<0.01).

Figure 4.S1 Schematic depicting metabolic pathways that can be analyzed with DNP probes. The background of the figure is a representation of the KEGG human global metabolism map (01100) that was generated in R using Pathview. As in Figure 4.1A, purple nodes correspond to previously polarized probes. Pink nodes correspond to intermediates that have either been (i) directly visualized after injection of a DNP probe or (ii) have not been directly identified but precede a downstream intermediate that has been directly visualized. Yellow nodes correspond to metabolites that may serve as future molecular imaging probes, as suggested by the data provided in Table 4.S1. Dashed lines correspond to an enzyme or group of enzymes connecting DNP probes and/or intermediates. Colored semi-circles correspond to cancer types that may be imaged with a given DNP probe, as described in Table 4.S1. *52*

Figure 5.1 B_1 and Point Spread Function Corrections *67*
(A) A phantom containing sodium propionate used for estimation of the point spread function. (B) Stylization of the true signal corresponding to a point source. (C) Stylization of the signal measured from a point source located in a single voxel. (D) A 3D printed phantom filled with ethylene glycol and imaged using the double angle method for estimation of the B1 map for the surface coil located in the background of the image. (E) Stylization of signal anticipated from a uniform B1 field. (F) True signal measured from the phantom in (D) with a 20-degree excitation 2 cm from the center of the coil. (G, H, I) Raw, PSF corrected, and PSF + B1 corrected parametric maps of a rat with liver cancer (tumor located in upper left quadrant of image) with the foreground parametric map indicating signifying the integral of pyruvate signal.

Figure 5.2 System for automated delivery of DNP Substrate *70*
(A) Schematic of the automated injection setup, along with photos of the setup at the magnet (B) and polarizer (C).

Figure 5.3 Figure 5.3: Schematics of relevant anatomy and experimental setup *75*
(A) Schematic of relevant rat anatomy highlighting that DNP-^{13}C injections are performed through the tail vein. While the liver is predominantly supplied by the portal vein, HCC is supplied primarily by branches of the hepatic artery. Therefore, pyruvate arriving to the tumor takes the following path after injection: tail vein→inferior vena cava→right heart→pulmonary circuit→left heart/aorta→proper hepatic artery (via celiac artery)→tumor. (B) Schematic of a capillary bed within a tumor in the described model highlighting that the majority of measurable DNP-^{13}C signal is extracellular pyruvate, while the majority of measurable lactate and alanine is produced within tumor cells. (C) Schematic of the experimental setup that highlights a semi-automated method for DNP-[1-^{13}C]-pyruvate injection upon dissolution with the assistance of an HPLC pump. [This subpanel is a modification of Figure 5.2A.]

Figure 5.4 Apparent metabolism rates measured by inter-metabolite ratios are sensitive to probe dose. *77*
(A, C) Parametric maps of the intratumoral lactate-to-pyruvate ratio after LD (A) and HD (C) injections in the foreground with a T_2-weighted ^{1}H image in the background. The lactate-to-pyruvate ratio is markedly reduced in the HD injection relative to the LD injection. (B, D) Waterfall plots of intratumoral spectra after an LD (B) and HD (D) injection. Pyruvate (δ: 176.5 ppm) levels increase dramatically after HD injection (relative to LD injection), while lactate (δ: 183.35 ppm) and alanine (δ: 170.4 ppm) amounts remained relatively constant. (E) Comparison of metabolite fractions and inter-metabolite ratios with LD followed by HD pyruvate injections. Significant changes are noted for P/TCM (p=8.83e-3), L/TCM (p=2.94e-

3), L/P (p=1.48e-2), and A/L (p=1.92e-2). (F) Comparison of metabolite fractions and inter-metabolite ratios with sequential LD injections. No significant changes were appreciated. (G) Comparison of the fold-change in metabolite fractions and inter-metabolite ratios between an LD followed by HD injection and two sequential LD injections. Significant changes are noted for P/TCM (p=4.93e-3), L/TCM (p=3.60e-5), and L/P (p=1.65-4). [TCM = Total Carbon Metabolites = Pyruvate + Lactate + Alanine]

Figure 5.5 Pyruvate and radical are excreted in urine after a DNP injection *79*

(A) Graphical representation of serum concentrations of pyruvate after a single LD injection. Pyruvate concentration is significantly elevated 5- and 10-minutes following injections (p=8.07e-3, 3.41e-2). (B) Urine pyruvate concentration are elevated after a single LD injection (p=2.72e-3). (C) Urine before (left) and after (right) a single LD injection reveals a substantial, qualitative change. (D) EPR of a representative pair of urine samples before and after a single LD injection reveals the presence of the radical source in the urine after injection, as confirmed in (E) by quantification of all samples (p=1.01e-3).

Figure 5.6 DNP quantifications of metabolism are sensitive to change in intratumoral enzyme activity *81*

(A, C) DNP-MRSI representations of the intratumoral lactate-to-pyruvate ratio before (A) and after (C) a 20 mg/kg LDHi injection in the foreground with a T_2-weighted ^{1}H image in the background. The lactate-to-pyruvate ratio is markedly reduced after LDHi. (B, D) Waterfall plots of intratumoral spectra before (B) and after (D) a 20 mg/kg LDHi injection. Lactate (δ: 183.35 ppm) levels increase dramatically after LDHi injection (relative to LD injection), while pyruvate (δ: 176.5 ppm) and alanine (δ: 170.4 ppm) levels rise a small amount. (E) Comparison of metabolite fractions and ratios when a 20 mg/kg LDHi administration is interposed between two sequential LD injections. Significant changes are noted for P/TCM (p=1.39e-3), L/TCM (p=3.57e-4), L/P (p=1.55e-3), and A/L (p=9.77e-4). (F) Measurements of LDH activity in tumor extracts harvested at necropsy significantly correlate with DNP-facilitated measurement of LDH flux according to the L/P ratio (p=2.71e-2).

Figure 6.1 Post-TACE Ischemia Induces Growth Latency In Vivo. *92*

(A) Representative pre-embolization arteriogram demonstrates positioning of the microcatheter in the left hepatic artery (yellow arrow) with contrast extending to (green arrow) and staining the tumor (red arrow). Post-embolization fluoroscopy demonstrates stasis of contrast within the left hepatic branch artery feeding the tumor as well as persistent contrast staining the tumor. (B) Representative serial T2-weighted MR images of untreated, control HCCs and treated HCCs prior to and following TAE. (C) Growth curves derived from MR-based measurements of tumor volume in untreated HCCs and treated HCCs prior to and following TACE demonstrated a significant reduction in growth for TAE-treated tumors (p = 0.011 at posttreatment day 4; p = 0.029 at posttreatment day 7). Tumor volumes are normalized to the first measurement and reported as the average percent change in volume ± standard deviation. (D) Representative immunofluorescence images of untreated control and TAE treated (post-treatment day 7) tumors stained for PCNA (pink) and HIF-1α (green). (E) Bar graph demonstrating a significant reduction in the percentage of DAPI+ nuclei that are also PCNA+ in treated tumors relative to untreated tumors as well as increase in mean HIF-1α fluorescence intensity per DAPI+ stained nucleus (PCNA: 3.9 ± 4.6% vs 22.0 ± 3.7%, p=.006; HIF-1α: .75 ± .39 vs .11 ± .01, p=.048).

Figure 6.2 Latent HCC Cells Are Hypometabolic *94*

(A) Western blots demonstrating suppression of the mTOR pathway, as supported by decreased Phospho-S6 levels despite sustained mTOR levels, and activation of the AMPK pathway in three human HCC (449, 387 and HG2) cell lines and one rat (HR2) HCC cell line exposed to ischemic (I) as compared standard conditions (S). (B) Metabolomic profiling of cells grown under ischemic vs. standard conditions demonstrates a reduction in intermediates of purine and pyrimidine biosynthesis in human (SNU387) and rat (HR2) HCC cell lines. (C) NMR extracts of HR2 cells incubated with 1-13C-acetate and surviving ischemic conditions demonstrated significant reductions in the synthesis of de novo lipids as compared to cells grown under standard conditions (p = 0.0013). Similarly, bicinchoninic acid assay protein measurements demonstrated significant reductions in protein synthesis for HR2 cells surviving severe ischemia as compared to cells grown under standard conditions (p = 0.0086).

Figure 6.3 Latent HCC Cells Undergo Metabolic Reprogramming. *97*

(A) HR2 cells grown under severe ischemia with 1-13C-glucose demonstrated lower C13-labeled protein enrichment as compared to cells grown under standard conditions, indicating reduced translation from glucose-derived alanine (p<2.2e-16). (B) Abundance of total peptide

(C13 and C12 combined) graphed after normalization to mean peptide abundance for all peptides mapping to glycolytic enzymes reveals consistent increase in abundance of glycolytic enzymes under ischemia, despite overall reduction in translation. (C) Western blots demonstrating translational and post-translational alterations in the enzymes that metabolize pyruvate in the final step of glycolysis in cells surviving severe ischemia (I) relative to cells grown under standard conditions (S), including an increase in the levels of LDHA and its activated, phosphorylated form. In addition, phosphorylation of pyruvate dehydrogenase to its inactive form was observed as a band shift toward a higher molecular weight. (D) Despite these alterations, metabolic analyses demonstrated a reduction in glucose uptake for cells surviving severe ischemia ($p = 0.0004$). (E) NMR spectroscopy of cell extracts incubated with U-13C-glucose demonstrated alterations in glycolytic flux consistent with the above-described changes in protein expression with a significant reduction in the alanine:lactate ratio ($p = 0.03$). (F, G) Chemical inhibition of LDH (LDHi 737, 2.5 μM) resulted in the suppression of lactate excretion for HCC cells grown under standard and ischemic conditions within 24 hours of incubation; however, cells grown under ischemia were unable to survive these conditions when LDH was inhibited ($p < 0.0001$ for comparisons of lactate excretion rate under standard and ischemic conditions). (H) Schematic illustrating metabolic reprogramming of HCC cells surviving severe ischemia to limit anabolism and shunt glucose towards carbons toward lactate.

Figure 6.4 DNP-MRS Demonstrates Metabolic Reprogramming in Perfused HCC Cells Surviving Severe Ischemia In Vitro. *100*

(A, B) HCC cells grown under standard growth conditions demonstrated increasing levels of oxygen utilization and associated nucleoside triphosphate to inorganic phosphate (NTP/Pi) ratios which diminished rapidly when the growth environment is changed to ischemic conditions (anoxia with nutrient depleted medium, single arrow) for 6 hours mimicking TAE. The maintenance of cellular viability under these conditions is underscored by an increase in the oxygen utilization and the NTP/Pi ratio when the oxygen level is increased to 0.017 mM (double arrow). (C, D) DNP-MRS of hyperpolarized 1-13C-pyruvate demonstrates metabolic reprogramming of cells surviving TA(C)E-like ischemia (blue spectrum) with a reduction in the alanine to lactate ratio (n=2 injections per condition; $p = 0.023$).

Figure 6.5 DNP-MRSI Enables the Detection of Latent HCC Cells Surviving TAE In Vivo *101*

(A-C) DEN-induced tumors demonstrate imaging features consistent with the LI-RADS criteria used for image-based diagnosis of HCC in the patients including arterial phase enhancement (APHE) and washout on delayed phase imaging relative to uninvolved liver. Images from a representative animal demonstrate T2-weighted and post-contrast T1-weighted imaging features consistent with viable HCC (yellow arrow in the top row). Consistent with imaging features observed following a complete response to TAE as assessed using the mRECIST criteria applied to assess treatment response in patients, MR imaging of TAE-treated HCCs demonstrated (i) a >30% reduction in APHE as compared to uninvolved liver (n=3; *p=.001, **p<.0001, ***p=.002) and (ii) a significant reduction in size (n=6; *p=.023, **p=.016). (C) Images from a representative animal demonstrate that while conventional imaging failed to detect viable tumor cells, DNP-MRSI of hyperpolarized 1-13C-pyruvic acid enabled the detection of persistent metabolism at the tumor periphery corresponding to regions of the tumor that appear non-viable on conventional MRI. In these regions reduced levels of pyruvate (D; *p=.046, **p=.028), lactate (E; *p=.046, **p=.046) and alanine (F) were observed. (C,H) At each post-TAE time point, tumor regions considered non-viable (→, NV in final column) using conventional contrast-enhanced MRI demonstrated reduced alanine-to-lactate ratios as evidenced by a reduction in the associated coefficient using a generalized linear model. Interestingly, images from a representative animal demonstrate persistent conversion of pyruvate to lactate on day 4 prior to the development of the development of recurrence on conventional imaging (green arrow, V: Viable voxels, NV: Non-viable voxels). (G) H&E staining of a representative TAE-treated 14 days after embolization demonstrates persistent viability in regions of tumor that are considered non-viable based on mRECIST criteria but exhibit persistent metabolism on DNP-MRSI adjacent to regions of necrosis and recurrent HCC. (I) In the regions of tumor that appeared non-viable on conventional MRI, a linear regression of the percent tumor viability and intra-tumoral pyruvate levels at post-TAE day 14 demonstrates a significant positive correlation (R^2=.90, p=.0041). (J) Linear regression of percent tumor viability and the change in the intra-tumoral alanine-to-lactate ratio 14 days after TAE demonstrates a significant negative correlation (R^2=.69, p=.04).

Figure 6.S1 Post-TACE Ischemia Induces Growth Latency In Vitro *119*
(A, B) HR2 cells grown under standard conditions (21% O2 and standard medium), moderate and severe hypoxia (3% O2 and 1% O2 with standard medium), nutrient-limited conditions (21% O2 and SG medium), and moderate ischemia (3% O2 and SG medium) all demonstrated persistent growth. Cells grown under severe ischemia (1% O2 and SG medium) demonstrated no growth with a linear regression demonstrating a slope that was not significantly different than zero. The median estimated doubling time (30.1 ± 5.2 days) is included for the purpose of comparison (*p=.03). Cells initially grown under severe ischemia (1% O2 + SG) for 1 week followed by standard conditions for an additional week (1% SG x 168 hr repletion) demonstrated a period of latency followed by persistent growth. (C) Representative FACS plot of HR2 cells stained with DAPI and a fluorescent antibody to Ki-67 nuclear antigen demonstrating a significant increase in the percentage of cells in the G0 phase and a decrease in the percentage of cells in the S phase of the cell cycle for cells incubated under severe ischemia as compared to cells incubated under standard conditions (G0 phase: 55.5 ± 1.8% vs. 18.2 ± 0.6%, p<.0001; S phase: 8.4 ± 1.8% vs. 18.3 ± 0.6%, p=.001, respectively). (D) Analysis of flow cytometry data demonstrates an increase in the proportion of G0 phase cells and a decrease in the proportion of S phase cells following incubations under standard [S] versus severely ischemic [I] growth conditions. (E) Western blots of lysates from rat (HR2) and human (SNU-449, SNU-387, HG2) cells confirmed the induction of quiescence and a metabolic stress response based on the increased expression of p27kip1 as well as increased stabilization of HIF-1α for cells surviving severe ischemia [I] as compared to cells incubated under standard conditions [S] consistent with in vivo data.

Figure A1.1 Model system: HCC cells embedded in low melting temperature agarose with viability assessment using a dual reporter assay *131*
(A) The cell-encapsulation matrix was prepared as a 1:1 mixture of Huh-7 HCC cells and 3% low melting temperature agarose. (B) Staining with a pair of fluorescent viability reporters demonstrates that the encapsulation procedure does not impair cell viability (green fluorescence). [Scale bar = 5 mm] (C) Boiling of the preparation resulted in complete cell death (red fluorescence [recolored to appear magenta] in the absence of green fluorescence). [Scale bar = 5 mm]

Figure A1.2 Cell encapsulation assay enables the spatial resolution of electrolytic ablation-induced changes in temperature, transmembrane potential, and pH *133*
(A) Electrolytic ablation was performed by the application of direct current between a nitinol cathode (left) and platinum anode (right) held in place by a 3D-printed spacer sitting atop the cell encapsulation matrix that was cast in a 6 cm tissue culture dish. (B) Electrolytic ablation performed in this assay led to the observation of cell death in the regions surrounding the cathode (Ca) and anode (An). [Scale bar = 5 mm] (C, D) 10x magnification brightfield image with and without fluorescence reporter overlay at an increased cell density of 3 x 106 cells mL-1 to highlight changes at the border of the ablation zone. [Scale bar = 400 µm] (E) A custom insert was 3D-printed to sit atop the encapsulation assay prepared in a 6 cm dish. The insert holds the electrodes at a spacing of 1.5 cm and enables precise measurement of temperature, pH, and voltage potential (relative to the midpoint between the two electrodes). (F) Temperature measurement sites (circles). (G) pH and voltage potential measurement sites (triangles).

Figure A1.3 Measurement of voltage and pH in the encapsulation assay suggests the generation of acid and base as the mechanism of death following electrolytic ablation *135*
(A) 3D surface plot of 2D linear interpolation of voltage potential measurements. (B) 2D linear interpolation contour plot of transmembrane potential calculated from voltage potential measurements via linear interpolation of the gradient magnitude across the width of an HCC cell. None of the regions of the assay reached the threshold voltage of 1 V necessary for electroporation. (C) 3D surface plot of 2D linear interpolation of pH measurements. (D) 2D linear interpolation contour plot of pH measurements recorded surrounding the cathode and anode, revealing basic changes surrounding the cathode [Ca] and acidic changes surrounding the anode [An].

Figure A1.4 Modification of the buffering capacity confirms a pH-dependent mechanism of cell death in electrolytic ablation *138*
(A, D, G) Viability images in the region surrounding the cathode and anode following electrolytic ablation with HEPES concentrations of 10 mM, 50 mM, and 200 mM. [Scale bar = 5 mm] (B, E, H) pH contour maps in the region surrounding the cathode and anode following electrolytic ablation with HEPES concentrations of 10 mM, 50 mM, and 200 mM. (C, F, I) pH contour maps overlaid upon viability images in the region surrounding the cathode and anode

following electrolytic ablation with HEPES concentrations of 10 mM, 50 mM, and 200 mM, respectively. [Scale bar = 5mm] (J) Comparison of the total area of cell death in the three conditions reveals a decreasing area of cell death with increased assay buffering capacity (n = 4 for all tests; [ANOVA] F: 75.96 on 2 and 9 DF, p < 1 x 10-5; [10 mM v 50mM] t: 4.39 on 4.59 DF, Bonferroni adjusted p < .05; [10 mM v 200mM] t: 11.36 on 3.10 DF, Bonferroni adjusted p < .01; [50 mM v 200mM] t: 11.75 on 3.34 DF, Bonferroni adjusted p < .01) (K) Comparison of total charge deposition in the three conditions reveals a decreasing quantity of charge deposition with increased buffering capacity (n = 3 for all tests; [ANOVA] F: 72.38 on 2 and 6 DF, p < 1 x 10-4; [10 mM v 50mM] t: -0.25 on 3.25 DF, Bonferroni adjusted p: 1.0; [10 mM v 200mM] t: 9.36 on 3.48 DF, Bonferroni adjusted p < 0.01; [50 mM v 200mM] t: 12.95 on 3.95 DF, Bonferroni adjusted p < 0.001).

Figure A1.5 By permitting diffusion or using multiple cathodes, precise ablation geometries may be achieved with electrolytic ablation *140*
(A) An increased area of cell death was observed after allowing 60 minutes of diffusion following electrolytic ablation (dashed white lines indicate ablation margin immediately after treatment; t: 7.32 on 3.4 DF, p < 0.01). [Scale bar = 5 mm] (B) A multi-cathode design allows the prescription of the volume in which cell death occurs as demonstrated by performing electrolytic ablation at 10 V for 10 seconds resulting in cell death surrounding the 9 electrodes. [Scale bar = 5 mm]

Figure A1.S1 Electrolytic ablation is found to induce cell death in multiple HCC cell lines *149*
(A) Electrolytic ablation demonstrates evidence of cell death surrounding the cathode (Ca) and anode (An) in SNU-449 cells [Scale bar = 5 mm]. (B) Electrolytic ablation demonstrates evidence of cell death surrounding the cathode (Ca) and anode (An) in HepG2 cells [Scale bar = 5 mm]. (C) Comparison of the area of cell death observed in three HCC cell lines reveals no significant difference in response to electrolytic ablation (F: 2.29 on 2 and 11 DF, p = 0.15).

Figure A1.S2 Reactive oxygen species are present following electrolytic ablation *150*
(A) Following electrolytic ablation, assays stained with CellRox® Green demonstrated areas of fluorescence in the regions surrounding the cathode (Ca) and anode (An), suggesting the presence of ROS. [Scale bar = 5 mm] (C) Exposure to 5 mM NAC, an antioxidant, reduced the amount of fluorescence detected from the regions surrounding the electrodes. [Scale bar = 5 mm] (B, D) Viability staining with Calcein/Ethd-1 reveal cell death in the absence (B) or presence (D) of NAC. [Scale bar = 5 mm] (E) Summed fluorescence intensity around the two electrodes, compared according to the natural log fold change with respect to the background of the image, demonstrated a significant decrease in ROS detection (t: 4.32 on 2.2 DF, p < 0.05). (F) The mean area of cell death observed after electrolytic ablation following rescue with NAC decreased by 23%, though this change did not reach statistical significance (t: 2.76 on 3.3 DF, p = 0.06).

Chapter 1: Introduction

1.1: Overview

Functional metabolic imaging facilitates non-invasive, temporospatial quantification of metabolic activity. This work establishes that functional metabolic imaging can be leveraged to better understand the dependencies of disease, enabling targeted therapy selection and providing quantitative assessment of treatment response. Extending beyond the use of traditional radiologic hallmarks for disease assessment, I hypothesize that effective translation of functional metabolic imaging probes hinges upon applications with a basis in the biology of disease. Herein, I describe a paradigm for unbiased selection of dynamic nuclear polarization (DNP) ^{13}C nuclear magnetic resonance spectroscopic imaging (MRSI) probes that captures metabolic variation in cancer and leverage this phenomenon for treatment selection and therapy evaluation in hepatocellular carcinoma (HCC), the fastest rising cause of cancer death in the US whose incidence is rising globally. I provide a description of important considerations for use of DNP-^{13}C-MRSI to evaluate metabolism and describe another application of this technology for locoregional response assessment in HCC.

1.2: Significance

Diagnostic imaging assessment criteria in cancer have traditionally focused on anatomic signatures of actively proliferating cells, including tumor growth and vascularity. Metabolic imaging approaches that leverage the unique biology of cancer have begun to shift this paradigm over the past quarter century with the rapid adoption of ^{18}F-fluorodeoxyglucose positron emission tomography (^{18}F-FDG-PET)[1,2]. The next frontier in precision imaging is the functionalization of imaging biomarkers that permit non-invasive assessment of tumor composition to promote treatment selection and evaluation of therapeutic efficacy. To make this next leap, novel strategies are required to select disease-specific imaging agents with a higher sensitivity to biologic activity and therapeutic vulnerabilities.

This work leverages variations in enzyme activity and availability to motivate selection of imaging agents in order to provide functional, metabolic readouts of intra-tumoral biologic activity. DNP-MRSI is a technology capable of multi-modal assessment of metabolism *in vivo*. DNP enhances detection sensitivity for labeled nuclei of biologic metabolites, promoting simultaneous spatial and kinetic readouts of metabolic activity. The described platform leverages DNP-^{13}C-MRSI to extend beyond measurements of substrate accumulation accomplished with PET, to quantify metabolic flux. This technology is the foundation of a precision imaging strategy that facilitates treatment selection, therapeutic efficacy assessment, and post-treatment surveillance. This functional metabolic imaging platform may prove critical in effecting curative cancer treatment by informing and monitoring cancer therapy. In particular, as DNP-MRSI enables metabolism quantification *in vivo*, this work demonstrates the sensitivity of DNP assessment to the on-target efficacy of therapies based upon changes in enzyme flux. While most prior studies have used DNP-MRSI for indirect assessment of drug efficacy, the presented strategy quantifies response directly, providing a non-invasive method to quantify pharmacokinetics and pharmacodynamics *in vivo*[3–5].

This work implements the described strategy for the treatment and evaluation of hepatocellular carcinoma (HCC). While the incidence and mortality of most cancers has decreased over the past twenty years, the incidence and mortality of HCC has risen during this time[6–8]. In 2012, liver cancer was the second most frequent cause of cancer mortality. Worldwide this has been attributed to chronic Hepatitis B and C, particularly in Asia. In the

United States, where HCC is the fastest rising cause of cancer related death, incidence and mortality is expected to continue to rise with the increasing prevalence of non-alcoholic fatty liver disease[6,7]. Treatment options for HCC are limited and the 5-year survival is less than 12%. For late-stage disease when resection or transplant are not possible, systemic therapies provide only a modest increase in overall survival (~3 months)[6,9]. The described work identifies a therapeutic vulnerability of HCC that could be exploited with a systemic therapy and identify an imaging biomarker capable of quantifying local response to treatment. Furthermore, molecular imaging with DNP-[1-^{13}C]-pyruvate is utilized to evaluate response to locoregional therapy via transarterial embolization, demonstrating that local metabolism predicts histologic response. This work directly addresses an urgent, unmet need in the management of HCC by suggesting a new treatment option and by providing a biologically motivated imaging strategy for response evaluation to both systemic and locoregional therapy.

1.3 Thesis Organization

This thesis reflects the body of work completed in Dr. Terence Gade's lab under the supervision of Dr. Gade and Dr. Schnall in pursuit of research aims supported by the National Institutes of Health (F30CA232388, PI: NRP) and the Society of Interventional Radiology Foundation (Allied Scientist Grant, PI: NRP).

Chapters 2 and 3, “An Introduction to Nuclear Magnetic Resonance and Hyperpolarization” and “Genome Editing Applications,” provide an introduction to fundamental concepts and techniques leveraged for experiments detailed subsequently. Chapter 2 provides an overview of nuclear magnetic resonance, magnetic resonance imaging and hyperpolarization, including applications of these technologies as is relevant within the thesis. Chapter 3 provides an introduction to genome editing, placing a particular emphasis on CRISPR-Cas9 and how it can be used for functional screening of molecular imaging probes. Chapter 3 is an adaptation of a manuscript, for which I am the first author, published in the *Journal of Vascular and Interventional Radiology* in 2018[10].

Chapters 4-6 detail the experimental work completed with DNP-^{13}C-MRSI, building upon the foundation provided by Chapters 2 and 3. Chapter 4, “Functional genetic screening enables theranostic molecular imaging in cancer,” dives into experimental evidence that genetic screening with CRISPR-Cas9 can inform the selection of DNP-^{13}C-MRSI probes for a theranostic application. As a proof-of-concept in HCC, a screening hit motivated imaging probe and therapy selection; in the chapter, I demonstrate that the imaging probe provides a functional assessment of the therapy’s efficacy. Chapter 4 is an adaptation of a manuscript, for which I am the first author, under review at *Clinical Cancer Research* as of March 2020. Chapter 5, “DNP-^{13}C-MRSI Quantification Considerations,” details important considerations for the use of DNP-^{13}C-MRSI studies of metabolism with experimental justification. Chapter 5 is an adaptation of a manuscript, for which I am the first author, under review at *Magnetic Resonance in Medicine* as of March 2020. Chapter 6, “Hyperpolarized Metabolic Imaging Detects Latent Hepatocellular Carcinoma Domains Surviving Locoregional Therapy,” provides an additional example of how DNP-^{13}C-MRSI can be used to evaluate response to cancer therapy, demonstrating that intratumoral DNP-[1-^{13}C]-pyruvate metabolism predicts residual viability after transarterial embolization in HCC. Chapter 6 is an adaptation of a manuscript, for which I am the first author, published in *Hepatology* in 2020[11].

Chapter 7, “Conclusions & Future Investigations,” provides a summary of my principal findings and delineates potential avenues for future investigations.

Additional work completed that I have contributed to during graduate school that is outside of the scope of the formal thesis is presented in Appendix 1 and in manuscripts referenced in this chapter. Appendix 1, “Electrolytic ablation enables cancer cell targeting through pH modulation,” discusses a series of experiments elucidating the mechanism of an electrolytic ablation, a therapy used for solid tumors (including HCC)[12]. Appendix 1 is an adaptation of a manuscript, for which I am the first author, published in *Communications Biology* in 2018[12]. This work motivated subsequent development of an MR-compatible electrolytic ablation designed to allow non-invasive monitoring of therapeutic efficacy that was published in the *Journal of Vascular and Interventional Radiology* in 2020[13]. In collaboration with colleagues in the Gade laboratory and at MD Anderson, I co-authored two manuscripts on the use of patient-derived xenografts derived from percutaneous biopsies as a tool for personalized medicine in HCC in the *Journal of Vascular and Interventional Radiology*[14] in 2018 and *Scientific Reports*[15] in 2019. In collaboration with colleagues in the Gade laboratory and the Department of Cancer Biology, I co-authored two manuscripts leveraging imaging for assessment of treatment planning and/or response in *Nature Communications*[16] and the *Journal of Vascular and Interventional Radiology*[17], both in 2020.

1.4: References

1. Groheux, D., Espié, M., Giacchetti, S. & Hindié, E. Performance of FDG PET/CT in the clinical management of breast cancer. *Radiology* **266**, 388–405 (2013).
2. Menzel, M. I. *et al.* Multimodal assessment of in vivo metabolism with hyperpolarized [1-13C]MR spectroscopy and 18F-FDG PET imaging in hepatocellular carcinoma tumor-bearing rats. *J. Nucl. Med.* **54**, 1113–1119 (2013).
3. Keshari, K. R. *et al.* Metabolic Response of Prostate Cancer to Nicotinamide Phophoribosyltransferase Inhibition in a Hyperpolarized MR / PET Compatible Bioreactor. *Prostate* **75**, 1601–1609 (2015).
4. Wu, X. C. *et al.* A novel inhibitor of pyruvate dehydrogenase kinase stimulates myocardial carbohydrate oxidation in diet-induced obesity. *J. Biol. Chem.* **293**, 9604–9613 (2018).
5. Park, I. *et al.* Detection of Early Response to Temozolomide Treatment in Brain Tumors Using Hyperpolarized 13C MR Metabolic Imaging. *J. Magn. Reson. Imaging* **33**, 1284–1290 (2011).
6. El-Serag, H. B. Hepatocellular Carcinoma. *N. Engl. J. Med.* **365**, 1118–1127 (2011).
7. W., S. B. *World Cancer Report*. (2014).
8. Bertuccio, P. *et al.* Global trends and predictions in hepatocellular carcinoma mortality. *J. Hepatol.* **67**, 302–309 (2017).
9. Hilgard, P. *et al.* Sorafenib in Advanced Hepatocellular Carcinoma. *N. Engl. J. Med.* **359**, 378–390 (2008).
10. Perkons, N. R. *et al.* The Implications of CRISPR-Cas9 Genome Editing for IR. *J. Vasc. Interv. Radiol.* **29**, 1264–1267 (2018).
11. Perkons, N. R. *et al.* Hyperpolarized Metabolic Imaging Detects Latent Hepatocellular Carcinoma Domains Surviving Locoregional Therapy. *Hepatology* (2019). doi:10.1002/HEP.30970
12. Perkons, N. R. *et al.* Electrolytic ablation enables cancer cell targeting through pH modulation. *Commun. Biol.* **1**, 1–10 (2018).
13. Stein, E. J. *et al.* Magnetic Resonance Imaging Enables Real-Time Monitoring of In Vitro Electrolytic Ablation of Hepatocellular Carcinoma. *J. Vasc. Interv. Radiol.* **31**, 352–361 (2020).
14. Sheth, R. A. *et al.* Patient-Derived Xenograft Tumor Models: Overview and Relevance to IR. *J. Vasc. Interv. Radiol.* **29**, 880–882 (2018).
15. Tischfield, D. J. *et al.* Establishment of hepatocellular carcinoma patient-derived xenografts from image-guided percutaneous biopsies. *Sci. Rep.* **9**, 1–8 (2019).
16. Lee, P. *et al.* Targeting glutamine metabolism slows soft tissue sarcoma growth. *Nat. Commun.* **11**, 1–15 (2020).
17. Park, B. *et al.* Outcomes from 3D augmented reality visualization for transarterial embolization in rats. *J. Vasc. Interv. Radiol.* (2020).

Chapter 2: An Introduction to Nuclear Magnetic Resonance and Hyperpolarization

2.1: Introduction

Hyperpolarized (HP) ^{13}C magnetic resonance spectroscopic imaging (MRSI) was made possible by a series of discoveries and inventions in the physical sciences over the past century. This chapter provides a brief introduction to nuclear magnetic resonance (NMR), the invention of magnetic resonance imaging (MRI) and applications of these technologies with respect to spectroscopy before proceeding to discuss HP methods, advantages and applications. When not otherwise cited directly, material contributing to this chapter, particularly the fundamentals of NMR and MRI, draws from course materials on these topics[1,2].

2.2: Principles of nuclear magnetic resonance

NMR refers to the fundamental principle that nuclei can possess angular momentum, or *spin*, when there is an uneven number of nucleons (protons, and/or neutrons). Nuclei are described as possessing either: (1) no spin ($I = 0$) if there is an even number of protons and neutrons, (2) half-integer spin ($I = \frac{1}{2}, \frac{3}{2}, \ldots$), or (3) integer spin ($I = 1, 2, \ldots$) if there is an uneven number of protons and neutrons. As described by quantum mechanics, the magnetic moment of a nucleus can only possess a discrete value; the number of possible states for a nucleus is governed by the nuclear spin quantum number, I, such that: $\#\,of\ states = 2 * I + 1$. Spin ½ nuclei, including ^{1}H and ^{13}C which are the subject of this work, can occupy two energy states, $m = \pm\frac{1}{2}$. In the presence of an external magnetic field, the ratio of spins ${N_{m=-1/2}}\big/{N_{m=+1/2}}$ is governed by the

Boltzmann distribution such that ${N_{m=-1/2}}/{N_{m=+1/2}} = \exp\,({\Delta E}/{K * T})$. The energy difference between quantized states (ΔE) is a function of the gyromagnetic ratio of a nucleus (γ) and the strength of the external field (B_0) according to the equation $\Delta E = \gamma h B_0/(2\pi)$. In these equations, T represents absolute temperature, K represents the Boltzmann constant ($1.38e - 23\,{J}/{K}$), and h represents Plank's constant ($h = 6.626e - 34\,J * s$). As such, the relative fraction of spins aligned with an external field, ${N_{m=-1/2}}/{N_{m=+1/2}}$, scales proportionally with B_0 and inversely with T.

Isaac Rabi received the Nobel Prize in Physics in 1944 for discovering a method to measure NMR through a series of experiments in which lithium chloride was passed through a strong, uniform magnetic field and simultaneously subjected to an oscillating magnetic field perpendicular to the main field[3]. When the frequency (ω) of an oscillating field matches a field-dependent characteristic frequency of a nucleus, such that ($\omega = \omega_0 = \gamma B_0$), the net magnetic moment of a population of spins will precess about the axis of the oscillating field. In Rabi's experiments, he found that when ω was held constant and B_0 was varied, the magnetic moment was only deflected when $\omega = \omega_0 = \gamma B_0$ (Figure 2.1).

Several years after Rabi's initial work, Edward Purcell and Felix Bloch demonstrated the phenomena in less contrived systems, both demonstrating resonance of hydrogen nuclei. Purcell did so by measuring absorption of protons in paraffin at the predicted resonant frequency, analogous to Rabi's initial experiments with lithium chloride[4]. Bloch independently measured NMR of hydrogen in water using a combination of transmit and receive radiofrequency (RF) coils, measuring nuclear induction rather than absorbance[5,6]. The two were jointly awarded the Nobel Prize in Physics for their work in 1952.

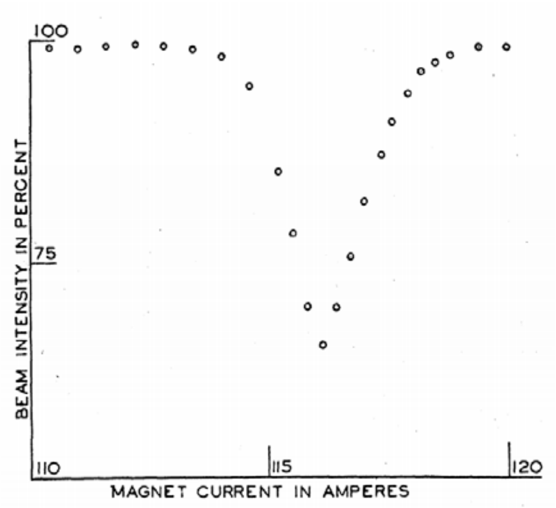

Figure 2.1:
Measurement of NMR by Isaac Rabi in lithium chloride. (Reproduced with permission from [3])

Bloch went on to describe a series of equations, which bear his name, that describe the response of an object's magnetic moment in a uniform external field to the presence of an oscillating RF field at the Larmor frequency (ω_0). In an x-y-z coordinate system where the uniform field is parallel to the z vector, an orthogonal RF field causes an apparent rotation of the magnetic moment into the x-y plane (where, of note, it continues to precess around the z vector). The flip angle (α), describes the extent of this rotation according to the formula $\alpha = \gamma \mathrm{B}_1 t$, dependent upon the length of time that the orthogonal field is present (t) and the strength of the orthogonal field (B_1). As equilibrium is restored, the rate at which the magnetic moment in the x-y plane decays after perturbation is described according to the formula: $M_{x,y}(t) = M_{x,y\,@\,t=0} * \exp\left(-{}^{t}\!/_{T_2}\right)$. The rate at which magnetization is restored in the z dimension is described according to the formula: $M_z(t) = M_0 + (M_{z\,@\,t=0} - M_0) * \exp\left(-{}^{t}\!/_{T_1}\right)$. T_1 and T_2 are constants that describe the longitudinal and transverse relaxation behavior of individual nuclei after perturbation in the presence of an external field; these constants vary with external field strength.

As a term, NMR not only describes the phenomenon of nuclear magnetic resonance, but also the technique by which this phenomenon is used to query the make-up of a sample for either spectroscopic or imaging applications.

2.3: Magnetic resonance spectroscopy

NMR (as a technique) is distinguished by its ability to provide an absolute quantification of a sample's elemental composition (for $I \neq 0$ nuclei) non-invasively. As the gyromagnetic ratio (γ), and hence the resonant frequency, is different for different nuclei it is possible to distinguish contributions of different elements to a sample with a broadband excitation and acquisition. Beyond this, the resonant frequency for individual atoms of identical nuclear composition can vary due to inter- and intramolecular interactions. This phenomenon is principally described by unique distributions of electron clouds around nuclei in different molecules and environments. These electron clouds slightly modify a nucleus' resonant frequency by shielding nuclear spins from the external magnetic field.

Chemical shift (δ) describes these variations in resonant frequency, which reflects the change in the effective magnetic field around a nucleus in the presence of local interactions, and is expressed in parts per million (ppm): $\delta = {(B_0 - B_{effective})}/{B_0}$. For convenience, it is typically quantified using frequencies relative to an agreed upon standard, tetramethylsilane, $\delta = {(\upsilon_{nucleus} - \upsilon_{standard})}/{\upsilon_{standard}}$. For example, a nucleus in close proximity to an electronegative atom will have a reduced electron density surrounding its nucleus and thus will experience reduced shielding and will have an increased resonant frequency, as compared to a more shielded nucleus. The chemical shifts of several commonly analyzed ^{13}C nuclei are provided in Table 2.1[7].

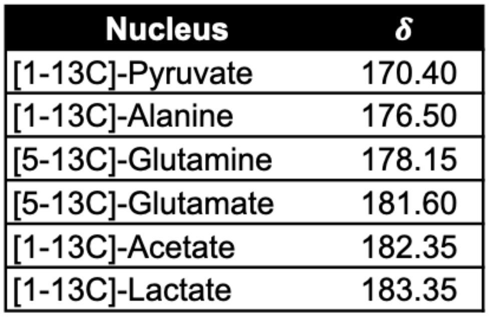

Nucleus	δ
[1-13C]-Pyruvate	170.40
[1-13C]-Alanine	176.50
[5-13C]-Glutamine	178.15
[5-13C]-Glutamate	181.60
[1-13C]-Acetate	182.35
[1-13C]-Lactate	183.35

Table 2.1:
Chemical shifts of frequently studied 13C nuclei[7].

2.4: Magnetic resonance imaging

In 1973 Paul Lauterbur described zeugmatography, Greek for “that which is used for joining,” as a method to obtain spatial distributions of an object’s spin density by combining a variable magnetic field to the above described approach of RF excitation and acquisition in the presence of a uniform magnetic field[8]. Through back-projections of multiple acquisitions generated in the presence of different variable magnetic fields (gradients) he described that it is possible to produce two-dimensional reconstructions of an object, and in doing so generated the first magnetic resonance image (MRI, Figure 2.2)[8]. Only several months later, Peter Mansfield independently published that the superposition of a linear magnetic field gradient on a static field could enable spatial resolution of signal when applying an inverse fourier transform to the free-induction decay (FID)[9]. In 1977, Mansfield described how alternation of gradients could be used to rapidly acquire images, a development critical for clinical use[10]. In recognition of this seminal work, Lauterbur and Mansfield were jointly awarded the Nobel Prize in Physiology or Medicine in 2003. Contributions by Raymond Damadian, including the discovery that characteristic relaxation rates for cancer tissue differed from healthy tissue[11] and collection of both the first human MRI[12] and first living animal tumor MRI[13], paved the way for use of the technique as a tool in clinical medicine.

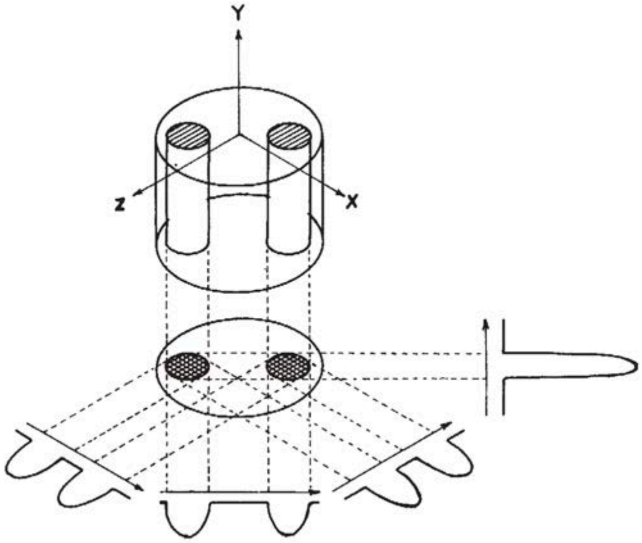

Figure 2.2:
Schematic of how the first MRI was generated by Paul Lauterbur in 1973. (Reproduced with permission from [8])

Since its invention, MRI has been rapidly adopted as a tool in clinical medicine for non-invasive examination of the body and identification of pathology. In contrast to several other medical imaging modalities, computerized tomography (CT) in particular, MRI does not use ionizing radiation. Further innovation in hardware and pulse sequence design over the past several decades has dramatically reduced technical complexity and requisite scan times, significantly accelerating clinical adoption. The development of contrast agents, particularly those that modify the characteristic relaxation rates of nuclei (T_1 and T_2) has been an effective means for accentuating signal differences between healthy and diseased tissues.

Clinically, MRI is predominantly used to examine hydrogen nuclei (^1H). This is primarily in the interest of maximizing sensitivity. ^1H, the predominant isotope of hydrogen, is a spin ½ nucleus and is the most abundant atom in the human body. Furthermore, of physiologically relevant nuclei, ^{1}H has a relatively large γ (42.58 MHz/T)[14].

2.5: Hyperpolarization of ^{13}C by dynamic nuclear polarization

In contrast to the sensitivity advantages of ^{1}H, carbon is far less abundant in the body and ^{13}C represents only 1.11% of this carbon, which also has a substantially smaller γ (10.71 MHz/T)[15]. As such, the *imageable* carbon signal is substantially smaller than the *imageable* hydrogen signal in the body. However, as ^{13}C NMR provides a unique opportunity to study the concentration and flux of carbon-based metabolites, there is a strong impetus to utilize methods that query these signals directly. Of note, the chemical shift (δ) range for frequently studied metabolites is much larger for ^{13}C nuclei (~200 ppm) than for ^{1}H nuclei (~10 ppm), enhancing the feasibility of signal deconvolution at standard field strengths[15]. While it is possible to use the thermal distribution of ^{13}C to study metabolism (as is done in NMR spectroscopy), the relative sensitivity penalties incurred require prolonged scan times (hours) to achieve a sufficient signal-to-noise ratio (SNR) for imaging applications that are limiting in the context of clinical practice.

Hyperpolarization techniques are used to skew the Boltzmann distribution of thermal equilibrium, increasing the relative fraction of imageable nuclei, ${}^{N_{m=-1/2}}\!/_{N_{m=+1/2}}$, by as much as 10^{5}. Dynamic nuclear polarization (DNP) is one such technique that achieves hyperpolarization by transferring the spin energy of an electron (in the form of a radical) to a ^{13}C nucleus. This is accomplished using nucleus specific microwave irradiation (~94MHz) of an amorphous solid (sometimes achieved via the addition of a glassing agent) of the ^{13}C labeled molecule of interest at a temperature close to absolute 0 (~1.4 K) in the presence of a free radical source, such as OX063 within an external magnetic field[16]. This leads to the transfer of spin polarization according to the Overhauser effect[17,18]. On a pre-clinical DNP apparatus, it is possible to hyperpolarize ~30-40% of the available ^{13}C nuclei, while newer machines designed for clinical use can achieve ~50-60% polarization efficiencies. For spectroscopic and imaging applications of DNP substrates, the solid-state mixture is rapidly melted in a heated buffer solution designed to normalize the pH to physiologic levels (7.4), attain a physiologic temperature (37 °C) and reduce the concentration to the mM range. The hyperpolarized state of these nuclei decays according to its longitudinal relaxation constant, T_1. Hence nuclei with prolonged T_1 are preferred[15,16]. In addition, once a nucleus is excited by an RF pulse (generating detectable signal in the transverse plane), it will not recover to its previously hyperpolarized state. Therefore, DNP experiments typically use a low flip angle (α), particularly when multiple excitations are performed.

Upon injection of the dissolute into a system of interest (i.e. physiologic buffer, *in vitro* cell population, *ex vivo* tissue sample, or *in vivo* blood vessel), the location and metabolic fate of the probe can be evaluated with standard NMR techniques for spectroscopy and imaging[16,19,20]. When the initial probe is metabolized to a new molecule or set of molecules, typically via an enzymatic reaction, the hyperpolarized spin state is retained on the carbon atom initially polarized. The distribution of molecules containing a hyperpolarized nucleus can be evaluated on the basis of chemical shift. Spectroscopic imaging permits quantification of this distribution in space and time (when multiple acquisitions are performed), enabling direct quantification of metabolism. Given the large relative range of chemical shifts for ^{13}C nuclei, a discrete advantage of this technique is that parallel assessment of multiple DNP probes is possible in s single acquisition. This is in direct contrast to positron emission tomography (PET), which relies upon coincidence detection of a single form of electromagnetic radiation that is common to all probes and precludes multiplexing.

The development of probes is guided by physical properties of individual molecules that are required for DNP, principally a long spin-lattice relaxation time (T_1) and the ability to form a glass at ~1.4 K, while the *in vivo* utility is governed by regional accumulation and metabolic conversion. More than 60 DNP-^{13}C-MRSI probes have been successfully polarized, and more than half have been used to directly measure metabolism[15]. Generated using Pathview, Figure 2.3 provides a schematic of DNP probes and the metabolic pathways they can directly quantify[21].

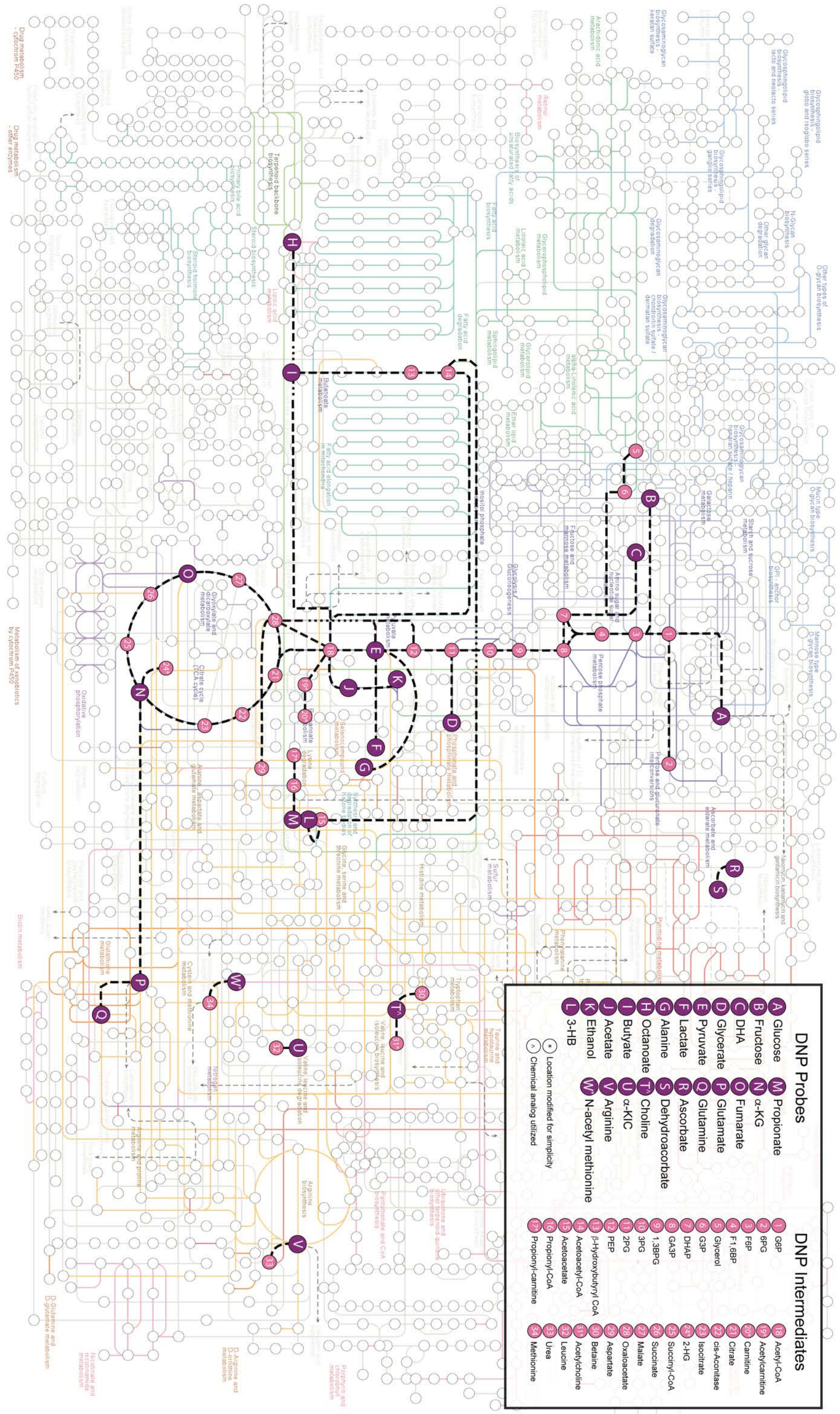
DNP Probes
A Glucose
B Fructose
C DHA
D Glycerate
E Pyruvate
F Lactate
G Alanine
H Octanoate
I Butyrate
J Acetate
K Ethanol
L 3-HB
M Propionate
N α-KG
O Fumarate
P Glutamate
Q Glutamine
R Ascorbate
S Dehydroascorbate
T Choline
U α-KIC
V Arginine
W N-acetyl methionine
* Location modified for simplicity
^ Chemical analog utilized
DNP Intermediates
1 G6P
2 6PG
3 F6P
4 F1,6BP
5 Glycerol
6 G3P
7 DHAP
8 GA3P
9 1,3BPG
10 3PG
11 2PG
12 PEP
13 β-Hydroxybutyryl CoA
14 Acetoacetyl-CoA
15 Acetoacetate
16 Propionyl-CoA
17 Propionyl-carnitine
18 Acetyl-CoA
19 Acetylcarnitine
20 Carnitine
21 Citrate
22 cis-Aconitase
23 Isocitrate
24 2-HG
25 Succinyl-CoA
26 Succinate
27 Malate
28 Oxaloacetate
29 Aspartate
30 Betaine
31 Acetylcholine
32 Leucine
33 Urea
34 Methionine

Figure 2.3:
DNP ^{13}C probes, their intermediates, and metabolic pathways they can facilitate measurement of.

2.6: DNP-[1-^{13}C]-pyruvate

Among DNP probes, DNP-[1-^{13}C]-pyruvate has been studied most extensively in preclinical and clinical applications. This issues from several key features of pyruvate, including: it forms a glass as a neat acid, the 1-C nucleus has a relatively long T_1 (~45 s), there is a large chemical shift separation between the 1-C nucleus and the corresponding nuclei of pyruvate's metabolites ($\delta_{[1\text{-}13C]\text{-pyruvate}}$: 170.4 ppm, $\delta_{[1\text{-}13C]\text{-lactate}}$: 183.35 ppm, $\delta_{[1\text{-}13C]\text{-alanine}}$: 176.5 ppm)[7]. Of principal focus for metabolic analyses, lactate dehydrogenase (LDH) is responsible for the interconversion of pyruvate and lactate, while alanine aminotransferase (ALT) is responsible for the interconversion of pyruvate and alanine (Figure 2.4). DNP-[1-^{13}C]-pyruvate can also be converted to pyruvate and acetyl-CoA, via pyruvate dehydrogenase, which generates DNP-bicarbonate (via CO_2). This fate is less frequently studied in imaging applications.

DNP-[1-^{13}C]-pyruvate has been utilized in a number of *in vitro*, *ex vivo*, and *in vivo* applications to measure enzyme activity, perfusion, and response to therapy[15,20,22]. This has been particularly useful in the study of cancer, as cancer cells are known to upregulate glycolysis and LDH, a phenomenon described as the Warburg effect[23,24]. Indeed, this principle has been leveraged for recent clinical trials in which conversion of DNP-[1-^{13}C]-pyruvate to DNP-[1-^{13}C]-lactate is used to predict tumor grade in human prostate cancer[25,26], identify metabolism in glioma[27], and quantify the lactate pool size in breast cancer[28].

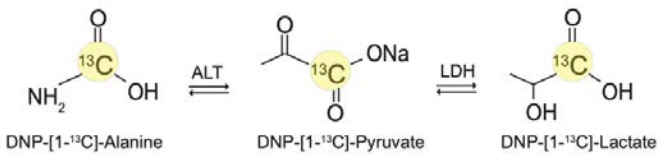

Figure 2.4:
Schematic of the interconversion of pyruvate, lactate, and alanine by ALT and LDH after hyperpolarization of [1-13C]-pyruvate. Yellow circles represent the 1-C in each molecule that retains the hyperpolarized label.

2.7: Pulse sequences

A magnetic resonance image is generated from inverse Fourier transformation of an acquisition, which traverses k-space according to a pulse sequence that describes the timing and intensity of RF pulses and gradient fields utilized in signal collection. The k-space trajectory and pulse sequence utilized are governed by the intended application. The two most frequently used pulse sequences for hyperpolarized imaging are free induction decay chemical-shift imaging (FID-CSI) and echo planar spectroscopic imaging (EPSI). EPSI is the principal pulse sequence used for the experiments described in this thesis for the reasons elaborated below.

FID-CSI

The FID-CSI pulse sequence is the most straightforward implementation of MRSI, collecting an FID from each point in k-space individually with an independent acquisition. The pulse sequence begins with an RF acquisition, at a low flip angle—particularly for HP acquisitions, superimposed upon a slice-selection gradient. While dephasing induced by the slice selection gradient is reversed, phase encoding gradients are applied to arrive at the desired point in k space before signal collection begins. Data acquisition occurs in the absence of any gradients and is followed up by an (optional) crusher gradient to kill any remaining transverse magnetization. The pulse sequence diagram for FID-CSI, reproduced in accordance with a Creative Commons CC BY license as adopted from [29], is presented in Figure 2.5.

Upon transformation to image space with inverse Fourier transforms in the spatial and spectral dimensions, FID-CSI produces an individual spectrum for each voxel. For HP applications, FID-CSI is relatively inefficient issuing from long requisite scan times and a high excitation burden. Minimizing both the acquisition length and number of excitations are principal concerns for HP-MRSI as both longitudinal relaxation (according to T_1) and RF excitation contribute to regression of the HP energy distribution to a Boltzmann distribution of thermal equilibrium.

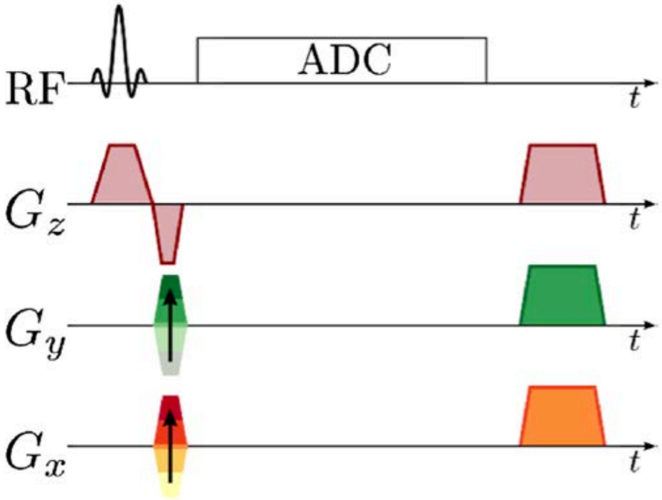

Figure 2.5:
Pulse sequence diagram for FID-CSI, as reproduced in accordance with a Creative Commons CC BY license as adopted from [29].

EPSI

EPSI is a more efficient strategy for MRSI, as it interleaves spatial and spectral data collection for a single spatial dimension (Figure 2.6)[29]. This reduces both the number of acquisitions and scan times (relative to a FID-CSI image) by a factor proportional to the number of k-space points sampled with each excitation (16 in Figure 2.6). In contrast to FID-CSI, a gradient is applied during signal acquisition to spatially encode data, a process which is repeated periodically either with a symmetric gradient or after a flyback gradient. Similar to FID-CSI, transformation in spatial and spectral dimensions produces an image in which each voxel has a corresponding spectrum. This technique, dependent upon robust gradients for data encoding, is particularly useful for HP MRSI applications as the reduced scan time and number of excitations preserves the HP state for subsequent acquisitions. Multiple sequential acquisitions permit assessment of how chemical species vary in both space and time. Implementations of MRSI in this thesis primarily utilize EPSI with a flyback gradient applied during acquisition of k_x. The pulse sequence diagram for the most straightforward implementation with linear traversal of k_y is presented in Figure 2.6; the k-space data has dimensionality of 12 x 16 x 1 x 64 (n_x x n_y x n_z x n_{points}).

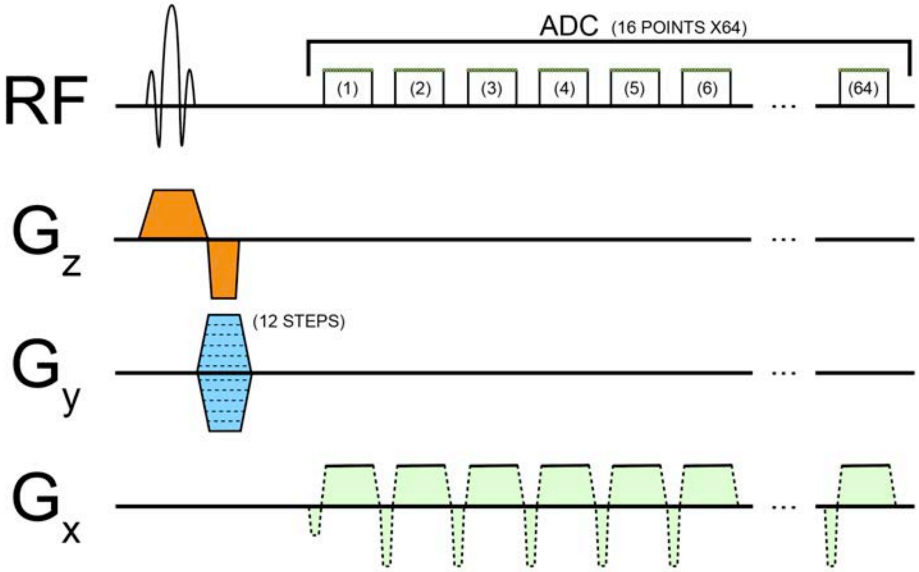

Figure 2.6:
EPSI pulse sequence diagram with k-space dimensionality of 12 x 16 x 1 x 64 (n_x x n_y x n_z x n_{points}).

2.8: Conclusion

The discovery of NMR and subsequent invention of MRI have profoundly changed the practice of medicine and science by providing techniques to non-invasively study structure and composition. The development of HP techniques, including DNP, has enabled the non-invasive study of physiologically relevant function particularly via DNP-^{13}C-MRSI.

2.9: References

1. Wehrli, F. & Song, H. K. Techniques of Magnetic Resonance Imaging: Bioengineering 581. (2017).
2. Tsourkas, A. Molecular Imaging: Bioengineering 583. (2018).
3. Rabi, I. I., Zacharias, J. R., Millman, S. & Kusch, P. A New Method of Measuring Nuclear Magnetic Moment. *Physcial Rev.* **53**, 318 (1938).
4. Purcell, E. M., Torrey, H. C. & Pound, R. V. Resonance Absorption by Nuclear Magnetic Moments in a Solid. *Physical Review* **69**, 37–38 (1946).
5. Bloch, F., Hansen, W. W. & Packard, M. The Nuclear Induction Experiment. *Phys. Rev.* **70**, 474–485 (1946).
6. Bloch F., Hansen W. W., and P. M. Nuclear Induction. *Physcial Rev.* **69**, 127 (1946).
7. UTSW. 13C Chemical Shifts Sorted by Compound Name. (2017). Available at: https://www.utsouthwestern.edu/education/medical-school/departments/airc/tools-references/chemical-shifts/chemical-shifts-sorted-by-compound-name.html.
8. Lauterbur, P. C. (SUNY). Image Formation by Induced Local Interactions: Examples Employing Nuclear Magnetic Resonance. *Nature* **242**, 190–191 (1973).
9. Mansfield, P. & Grannell, P. K. NMR 'diffraction' in solids? *J. Phys. C Solid State Phys.* **6**, 422–426 (1973).
10. Mansfield, P. & Maudsley, A. A. Planar Spin Imaging by NMR. *J. Magn. Reson.* **27**, 101–119 (1977).
11. Damadian, R. Tumor Detection by Nuclear Magnetic Resonance. *Science* **171**, 1151–1153 (1971).
12. Damadian, R., Goldsmith, M. & Minkoff, L. NMR in cancer: XVI. FONAR image of the live human body. *Physiol. Chem. & Phys.* **9**, 97–99 (1977).
13. Damadian, R., Minkoff, L., Goldsmith, M., Stanford, M. & Koutcher, J. Field Focusing Nuclear Magnetic Resonance (FONAR): Visualization of a Tumor in a Live Animal. *Science* **194**, 1430–1432 (1976).
14. Haacke, E. M., Brown, R. W., Thompson, M. R. & Venkatesan, R. *Magnetic Resonance Imaging: Physical Principles and Sequence Design*. (1999).
15. Keshari, K. R. & Wilson, D. M. Chemistry and biochemistry of 13C hyperpolarized magnetic resonance using dynamic nuclear polarization. *Chem. Soc. Rev.* **43**, (2014).
16. Perkons, N. R. *et al.* Hyperpolarized Metabolic Imaging Detects Latent Hepatocellular Carcinoma Domains Surviving Locoregional Therapy. *Hepatology* (2019). doi:10.1002/HEP.30970
17. Overhauser, A. W. Polarization of nuclei in metals. *Phys. Rev.* **92**, 411–415 (1953).
18. Abragam, A. & Goldman, M. Principles of dynamic nuclear polarisation. *Reports Prog. Phys.* **41**, 395–467 (1978).
19. Bohndiek, S. E. *et al.* Hyperpolarized [1-13C]-Ascorbic and Dehydroascorbic Acid: Vitamin C as a Probe for Imaging Redox Status in Vivo. *J. Am. Chem. Soc.* **133**, 11795–11801 (2011).
20. Salamanca-Cardona, L. & Keshari, K. R. 13C-labeled biochemical probes for the study of cancer metabolism with dynamic nuclear polarization-enhanced magnetic resonance imaging. *Cancer Metab.* **3**, 1–11 (2015).
21. Luo, W. & Brouwer, C. Pathview: An R/Bioconductor package for pathway-based data integration and visualization. *Bioinformatics* **29**, 1830–1831 (2013).
22. Chaumeil, M. M., Najac, C. & Ronen, S. M. Studies of Metabolism Using ^{13}C MRS

of Hyperpolarized Probes. *Methods Enzymol.* **561**, 1–71 (2015).

23. Hanahan, D. & Weinberg, R. A. Hallmarks of Cancer : The Next Generation. *Cell* **144**, 646–674 (2011).
24. Liberti, M. V. & Locasale, J. W. The Warburg Effect: How Does it Benefit Cancer Cells? *Trends Biochem. Sci.* **41**, 211–218 (2016).
25. Granlund, K. L. *et al.* Hyperpolarized MRI of Human Prostate Cancer Reveals Increased Lactate with Tumor Grade Driven by Monocarboxylate Transporter 1. *Cell Metab.* **31**, 105–114 (2020).
26. Nelson, S. J. *et al.* Metabolic imaging of patients with prostate cancer using hyperpolarized [1-^{13}C]Pyruvate. *Sci. Transl. Med.* **5**, 1–10 (2013).
27. Miloushev, V. Z. *et al.* Metabolic imaging of the human brain with hyperpolarized 13C Pyruvate demonstrates 13C lactate production in brain tumor patients. *Cancer Res.* **78**, 3755–3760 (2018).
28. Gallagher, F. A. *et al.* Imaging breast cancer using hyperpolarized carbon-13 MRI. *Proc. Natl. Acad. Sci.* **117**, 2092–2098 (2020).
29. Topping, G. J. *et al. Acquisition strategies for spatially resolved magnetic resonance detection of hyperpolarized nuclei*. *Magnetic Resonance Materials in Physics, Biology and Medicine* (Springer International Publishing, 2019). doi:10.1007/s10334-019-00807-6

Chapter 3: Genome Editing Applications

3.1: Introduction

This chapter is adopted from an article by Perkons et al. in the *Journal of Vascular and Interventional Radiology* that was published in 2018 entitled "The Implications of CRISPR-Cas9 Genome Editing for IR"[1]. The chapter provides a brief background to genome editing before elaborating upon the mechanism of CRISPR-Cas9 genome editing and its applications.

3.2: Background

The increasing accessibility and affordability of genome sequencing technologies have solidified the link between variations in the genetic code and human health. While pharmacologic targeting of the encoded proteins that are downstream effectors of genomic variation has been a mainstay, these recent advances in the understanding of the human genome underscore the power of genetic engineering for studying and treating disease. This recognition has led to the rapid development of tools for the direct modification of DNA through genome editing. The CRISPR-Cas9 system is the most recent addition to this toolset and holds great promise for both clinical and research applications (Figure 3.1).

Genome editing begins by targeting an endonuclease, such as zinc-finger nucleases (ZFNs), transcription activator-like effector nucleases (TALENs) and more recently, the Cas9 nuclease, to specific genomic sites. There, these nucleases cleave the DNA at the desired sites, resulting in double strand breaks (DSBs). The repair of these DSBs through the intrinsic cellular mechanisms of non-homologous end-joining (NHEJ) and homology directed repair (HDR) can be exploited to modify the genome at the cleavage sites (Figure 3.1C). NHEJ, a homology-independent pathway, is a relatively error-prone mechanism of DNA DSB repair. This infidelity is leveraged for the efficient generation of insertion/deletion mutations (indels) of nucleotides. These indels can lead to frameshift mutations, in-frame mutations, or premature stop codons that contribute to a loss of protein function. Homologous recombination (HR), the most common form of HDR, is the more accurate DNA repair mechanism due to its requirement for a high level of sequence homology between the fractured DNA strands. This requirement results in high fidelity repairs that enable precise genome editing. Among these mechanisms of repair, HR was among the first to be exploited for genome editing. This use was based on the discovery that synthesized DNA strands with sequence similarity to innate cellular DNA can replace the existing nuclear template to edit the genome through the insertion or removal of a desired gene. Controlling the location of DSBs using endonucleases increases the efficiency of HR-mediated gene modification. While the early use of TALENs and ZFNs for this application demonstrated the value of targeted DNA breaks in genome editing, these designer endonuclease strategies are laborious and inefficient limiting their application in biomedical research and clinical medicine. Nevertheless, these technologies set the stage for the recent development of the CRISPR-based genome editing approaches that are addressing these deficiencies to revolutionize the field of biomedicine and beyond[2].

3.3: Fundamentals of CRISPR-Cas9 genome editing

CRISPR, an acronym for Clustered Regularly Interspaced Short Palindromic Repeats, is a genome-editing technique born from discoveries in bacterial immunity. Ishino and colleagues first discovered a series of repeating bacterial genomic elements in 1987. Continued investigation revealed that these motifs contained short sequences of

DNA copied from the genomes of prior viral invaders. When translated into RNA in the presence of the Cas9 (another acronym, for CRISPR-associated protein 9) endonuclease, these RNA sequences and the Cas9 protein form a complex that binds to complementary DNA sequences to determine the location of DSB breaks. Repair of the DNA sequence can lead to mutations that inactivate proteins. The utility of CRISPR is underscored by its central role in the evolution of microbial immunity where it is used to disrupt the genome of invading bacteriophages.

These discoveries enabled the adaptation of the CRISPR-Cas9 platform as a tool for genome editing in other cell types. This approach is composed of two principal components: (i) the Cas9 protein and (ii) a single guide RNA (sgRNA) sequence. A sgRNA includes a scaffold sequence for Cas9-binding and a user-defined *spacer* sequence that is complementary to the *protospacer* sequence found on the target DNA. The design of the spacer sequence of a sgRNA is informed by the proximity of the target protospacer sequence to protospacer-adjacent motifs (PAMs), a series of nucleotides that are required for Cas9 binding (Figure 3.1)[3,4].

In vitro and/or *in vivo* genome editing using CRISPR-Cas9 begins with the introduction of the necessary CRISPR machinery (sgRNA and Cas9) to the target cell. This enables modification of the cell’s nuclear DNA at the site designated by the sgRNA sequence which guides the Cas9 endonuclease to this location. Following the DSB by the Cas9 protein, the cell’s innate machinery for DSB repair can lead to inactivation of the corresponding protein (“knock-out”) or gene insertion (“knock-in”) (Figure 3.1). With the capacity to remove, edit, or introduce DNA sequences, CRISPR-Cas9-based genome editing offers a facile system that enables functional studies of the genome. The power of this technique over previous approaches issues from its programmability. This programmability derives from the remarkable versatility enabled by CRISPR with respect to the diversity of potential gene targets. This versatility results from the fact that the Cas9 protein only requires that a PAM motif be in the vicinity of the gene target to which the sgRNA will bind, a motif that is relatively abundant within the genome. For example, the "NGG" PAM that is recognized by SpCas9 is encountered once in every eight base pairs, on average.

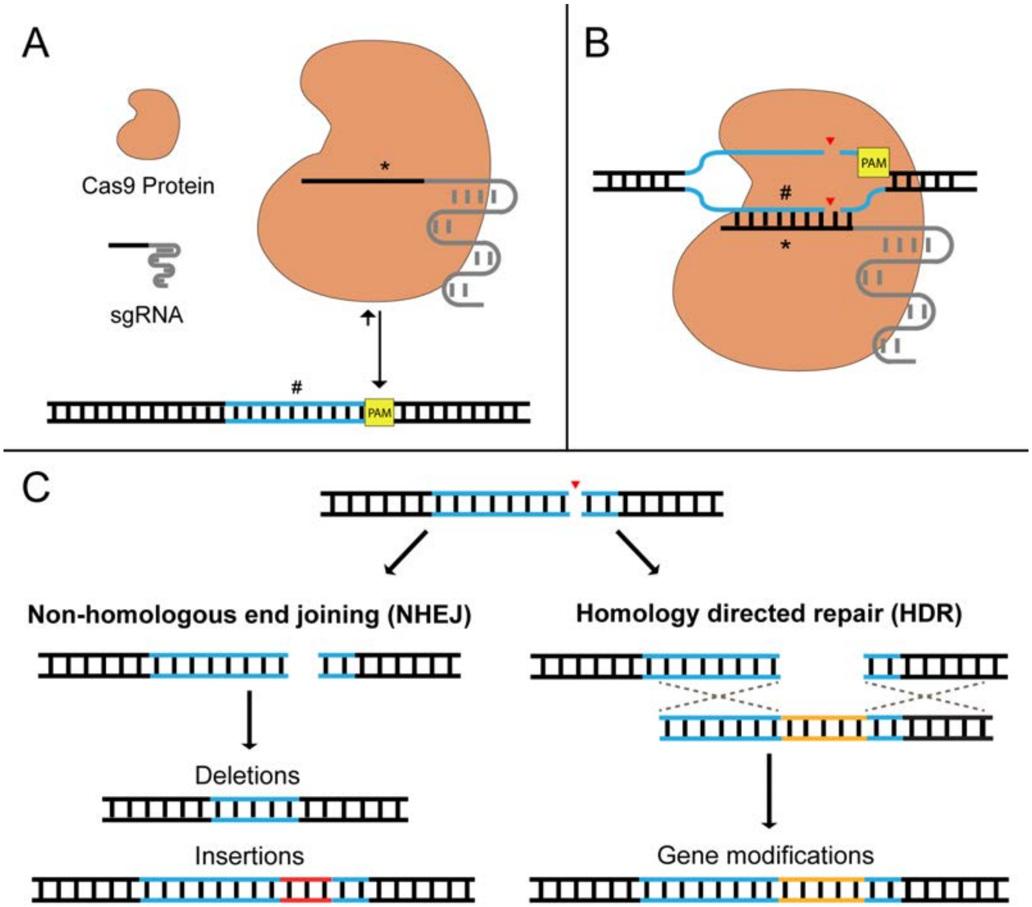
A
Cas9 Protein
sgRNA
*
#
PAM
B
PAM
#
*
C
Non-homologous end joining (NHEJ)
Homology directed repair (HDR)
Deletions
Insertions
Gene modifications

Figure 3.1
CRISPR-Cas9 genome editing enables sequence-specific modification. (A) Cas9-sgRNA complex scans the genome for a PAM-site in proximity to a sequence complementary to the sgRNA. (B) Following strand separation, PAM-dependent Cas9 endonuclease activation and DSB formation ensues. The spacer motif of the sgRNA (*) is complementary to the protospacer of the target DNA (#). (C) These DSBs can subsequently be repaired through either NHEJ or HDR. NHEJ involves error-prone ligation may yield small insertions or deletions. HDR involves introduction of a donor template with sequence complementarity (dashed lines) to the regions flanking the DSB, which enables sequence modification by incorporation of this template into the genome[3,4].

While offering significant advantages over prior techniques, there are important limitations to recognize in the use of CRISPR. As gene knock-outs and knock-ins depend upon cellular DSB repair machinery, resulting genome modifications are permanent, underscoring the importance of ensuring specificity and efficacy. Given these requirements, current initiatives are emphasizing the need to address four primary challenges including (i) the targeted delivery of the CRISPR machinery, (ii) the highly specific introduction of the intended gene alteration, (iii) the mitigation of off-target effects that may occur through unintended gene alterations and (iv) the improvement of editing efficiency of primary cells. In addition, as this technology advances toward clinical application, additional emphasis has been placed on limiting potential side effects by mitigating the immunogenicity of the CRISPR machinery as well as ensuring the fidelity of the intended gene modifications that may be influenced by the sequence variations that are characteristic of the human genome (e.g., small nucleotide polymorphisms)[3,4].

3.4: CRISPR-enabled scientific advances

Despite its recent development, CRISPR-based genome editing is already a mainstream technology in biomedical research enabling essential advances in biomedicine. The generation of cells lacking a functional copy of a gene is a common early step for delineating protein function. As genome modifications can target specific loci at a relatively low cost via sgRNA design, modifications made in parallel using tens of thousands of unique sgRNAs enables high-throughput genetic screening. Indeed, a variety of sgRNA libraries are now commercially available. Pooled knockout screens using these libraries help to identify genes essential for cellular survival[5–7]. By providing the ability to manipulate any gene of interest, CRISPR can be used to generate loss-of-function and gain-of-function mutations that will continue to elucidate disease mechanisms. This holds particular relevance to cancer biology where the identification of genes that are differentially required for oncogenesis and malignant phenotypes enables the development of novel diagnostic and treatment modalities[3,8].

The applications for this technology continue to emerge. In epigenetics, CRISPR can be used to modify DNA structure and accessibility without modifying the DNA itself[9,10]. In gene therapy, investigators use CRISPR to modify immune cells to enhance their effector function including the modification of the T-cell receptor of chimeric antigen receptor T (CAR-T) cells[11]. For *in vivo* modeling, this technology has enabled the development of animal models that are more representative of human disease[12–14]. Moreover, CRISPR is being adapted to drive the next generation of genome editing techniques by enabling the modification of single bases of DNA to yield even more specific, pin-point changes in DNA and RNA without the need for DNA cleavage[15,16]. These approaches dramatically enhance the safety profile of DNA editing and hold important implications for patient disease, where CRISPR-based methodologies can be applied to characterize the influence of genetic alterations and may hold the potential to correct these abnormalities[3,17–20].

3.5: Implications for Interventional Radiology

The advent of CRISPR-Cas9-based genome editing is largely responsible for the renewed enthusiasm around the clinical applications of gene therapy. Studies have already illustrated the potential of CRISPR gene editing to alter disease progression in an *in vivo* animal model of Duchenne muscular dystrophy [3]. Although advances brought about by CRISPR-Cas9-based technologies overcome many prior challenges and inefficiencies of genome editing techniques, the delivery of the necessary machinery to achieve successful application in humans remains a significant obstacle. Locoregional delivery of viral vectors via percutaneous or endovascular approaches is a potential solution that is drawing increased interest. In this regard, the CRISPR revolution is certain to impact the practice of Interventional Radiology (IR) as these specialists are asked to play a central role in the administration of gene therapies. The impending reality of CRISPR-Cas9-based genome editing in patients is underscored by the recent attention paid to the associated complex bioethical considerations about which physicians will also need to remain informed.

The integration of CRISPR-based diagnostic platforms into clinical practice also holds the potential to inform interventional therapies for a range of diseases. For example, a platform leveraging CRISPR technology to detect single molecules of RNA or DNA (attomolar sensitivity) has been applied for rapid detection of antibiotic resistance genes in clinical isolates, affording expedited antimicrobial agent selection compared to traditional culture and sensitivity assays. The platform has also been adapted for high throughput genetic profiling of malignancies using cell-free DNA from peripheral blood samples, to aid in the diagnostic characterization and in the identification of targetable genetic mutations. The molecular signatures derived from these assays could supplement current diagnostic imaging modalities for diagnosis and response assessment after locoregional therapy.

CRISPR-Cas9 based approaches to drug screening are also less expensive and labor intensive than traditional high throughput screening techniques and offer a unique tool for developing precision medicine treatment paradigms. The current Interventional Oncology treatment armamentarium has limited flexibility to address the specific biology of a patient’s individual tumor, but a CRISPR-based strategy could enable rapid identification of targetable vulnerabilities in tumor cells. This approach could be translated into personalized adjuvant therapies that potentiate existing treatments or lead to entirely new locoregional therapies. Screens could be abridged to identify targetable vulnerabilities to existing drugs, many of which may not previously have been considered as adjuvant therapies. In this manner, CRISPR-Cas9-based genome editing may enable the development of a functional screening paradigm that can be integrated into current clinical workflows (Figure 3.2). The implementation of this paradigm depends upon the acquisition of tumor biopsies. IR practitioners, as the most common operators for percutaneous biopsies, will be crucial in its realization.

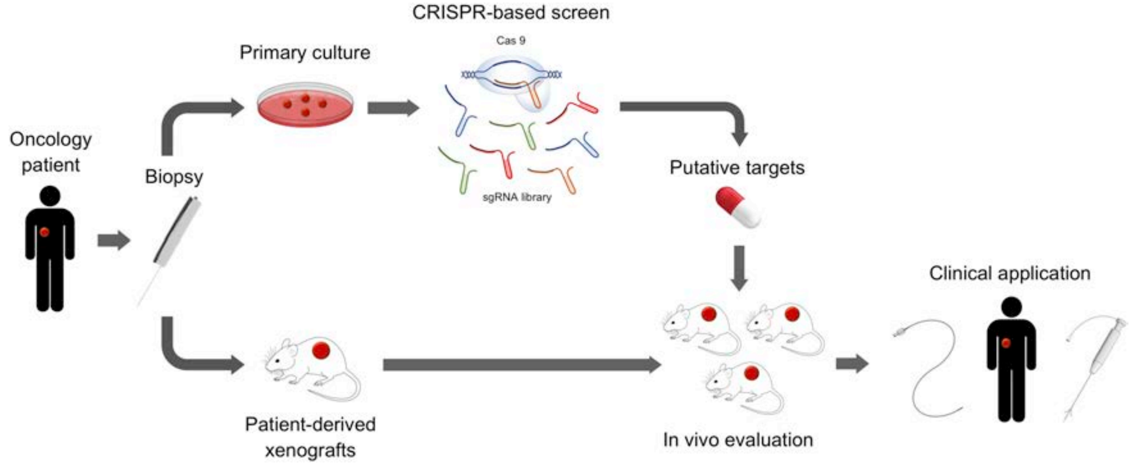
CRISPR-based screen
Primary culture
Cas 9
Oncology patient
Biopsy
sgRNA library
Putative targets
Clinical application
Patient-derived xenografts
In vivo evaluation

Figure 3.2:
CRISPR enables translational screening approaches that guide therapy selection. Patient cells taken from biopsy and expanded in culture can be evaluated for dependencies with pooled screening approaches using thousands of sgRNAs that leverage CRISPR-Cas9 technology. *In vivo* models of patient derived disease can be prepared with patient derived xenografts where these in vitro dependencies can be confirmed, thereby guiding therapy selection.

3.6: Implications for Molecular Imaging with DNP-^{13}C-MRSI

Treatment selection in cancer is increasingly motivated by the biology of the underlying disease. Molecular imaging enables non-invasive assessment of tumor biology, affording precision to therapy choice and response evaluation[21]. A unified approach to molecular imaging of tumor biology hinges on probe fidelity. Biologically motivated probe selection, which could potentially include leveraging CRISPR-Cas9 genome editing, requires determination of disease-specific dependencies. Distinguishing features of cancer cells that enable tumor growth—particularly differential utilization of metabolic pathways—provides the ability to move beyond diagnosis to identify therapeutic interventions that target these aberrancies. This strategy for hallmark identification frequently shapes treatment development, which has been remarkably successful for single gene diseases[22,23]. Leveraging molecular imaging to establish imaging biomarkers of such dependencies offers the promise of unifying a molecular imaging strategy that facilitates diagnosis, treatment selection, and—by extension—offers a direct metric of therapeutic efficacy for response quantification.

Relative enzyme abundance and activity have been shown to influence dynamic nuclear polarization (DNP) ^{13}C magnetic resonance spectroscopic imaging (MRSI) probe label conversion; isolating enzymatic dependencies of disease could be used facilitate selection of DNP-^{13}C-MRSI probes sensitive to the activity of those enzymes[24–26]. CRISPR-Cas9 negative selection screening can be utilized as a high-throughput approach to identify essential enzymes. By studying the effect of CRISPR-induced gene knock-outs on cell viability, negative selection screening can be used to identify enzymes important to proliferation in cancer[5]. Probes metabolized by these enzymes could serve as a functional readouts of disease activity and/or response to treatment, directly informing disease management. Figure 2.3, highlights DNP-^{13}C-MRSI probes that can be used as direct readouts of enzyme activities.

3.7: Conclusion

The field of molecular biology has rapidly advanced to include a diverse array of tools for modifying the genome. CRISPR-Cas9-based techniques enhance the programmability of these tools to enable the robust modification of the genome in a site-specific manner. Early implications of these developments for the practice of IR will manifest *as in vitro* tools for characterizing disease and response to therapy as well as the delivery of gene therapy. Moving forward, this technology will lead to medical therapies that work to enhance the specificity and efficacy of interventional oncology procedures. In addition, negative selection screening with CRISPR-Cas9 has the potential to inform these interventions through the selection of biologically relevant probes that facilitate functional assessments of cancer that include therapeutic response evaluation.

3.8: References

1. Perkons, N. R. *et al.* The Implications of CRISPR-Cas9 Genome Editing for IR. *J. Vasc. Interv. Radiol.* **29**, 1264–1267 (2018).
2. Gaj, T., Gersbach, C. A. & Barbas, C. F. ZFN, TALEN, and CRISPR/Cas-based methods for genome engineering. *Trends Biotechnol.* **31**, 397–405 (2013).
3. Hsu, P. D., Lander, E. S. & Zhang, F. Development and applications of CRISPR-Cas9 for genome engineering. *Cell* **157**, 1262–1278 (2014).
4. Doudna, J. A. & Charpentier, E. The new frontier of genome engineering with CRISPR-Cas9. *Science* **346**, 1258096 (2014).
5. Shalem, O., Sanjana, E. N., Hartenian, E. & Zhang, F. Genome-Scale CRISPR-Cas9 Knockout. *Science* **343**, 84–87 (2014).
6. Shi, J. *et al.* Discovery of cancer drug targets by CRISPR-Cas9 screening of protein domains. *Nat. Biotechnol.* **33**, 661–667 (2015).
7. Konermann, S. *et al.* Genome-scale transcriptional activation by an engineered CRISPR-Cas9 complex. *Nature* **517**, 583–588 (2015).
8. Zhou, Y. *et al.* High-throughput screening of a CRISPR/Cas9 library for functional genomics in human cells. *Nature* **509**, 487–91 (2014).
9. Baubec, T. *et al.* Genomic profiling of DNA methyltransferases reveals a role for DNMT3B in genic methylation. *Nature* **520**, 243–247 (2015).
10. Navarro, J. M. *et al.* Site- and allele-specific polycomb dysregulation in T-cell leukaemia. *Nat. Commun.* **6**, 1–11 (2015).
11. Keeler, A. M., ElMallah, M. K. & Flotte, T. R. Gene Therapy 2017: Progress and Future Directions. *Clin. Transl. Sci.* **10**, 242–248 (2017).
12. Xue, W. *et al.* CRISPR-mediated direct mutation of cancer genes in the mouse liver. *Nature* **514**, 380–384 (2014).
13. Platt, R. J. *et al.* CRISPR-Cas9 knockin mice for genome editing and cancer modeling. *Cell* **159**, 440–455 (2014).
14. Wang, H. *et al.* One-step generation of mice carrying mutations in multiple genes by CRISPR/cas-mediated genome engineering. *Cell* **153**, 910–918 (2013).
15. Dolgin, E. CRISPR hacks allow for pinpoint repairs. *Nature* **550**, 439–440 (2017).
16. Gaudelli, N. M. *et al.* Programmable base editing of A•T to G•C in genomic DNA without DNA cleavage. *Nature* **551**, 464–471 (2017).
17. Nathwani, A. C. *et al.* Long-Term Safety and Efficacy of Factor IX Gene Therapy in Hemophilia B. *N. Engl. J. Med.* **371**, 1994–2004 (2014).
18. Gruntman, A. M. & Flotte, T. R. Progress with Recombinant Adeno-Associated Virus Vectors for Gene Therapy of Alpha-1 Antitrypsin Deficiency. *Hum. Gene Ther. Methods* **26**, 77–81 (2015).
19. Bainbridge, J. W. B. *et al.* Long-Term Effect of Gene Therapy on Leber's Congenital Amaurosis. *N. Engl. J. Med.* **372**, 1887–1897 (2015).
20. Nelson, C. E. *et al.* In vivo genome editing improves muscle function in a mouse model of Duchenne muscular dystrophy. *Science* **351**, 403–407 (2016).
21. Pantel, A. R. A. R., Ackerman, D., Lee, S. C. S. C., Mankoff, D. A. D. A. & Gade, T. P. F. T. P. Imaging cancer metabolism: Underlying biology and emerging strategies. *J. Nucl. Med.* **59**, 1340–1349 (2018).
22. Druker, B. J. *et al.* Effects of a selective inhibitor of the Abl tyrosine kinase on the growth of Bcr-Abl positive cells. *Nat. Med.* **2**, 561–566 (1996).
23. Buchdunger, E. *et al.* Inhibition of the Abl Protein-Tyrosine Kinase in Vitro and in Vivo by a Derivative 2-Phenylaminopyrimidine Derivative. *Cancer Res.* **56**, 100–

104 (1996).

24. Gallagher, F. A. *et al.* Carbonic Anhydrase Activity Monitored in Vivo by Hyperpolarized 13C-Magnetic Resonance Spectroscopy Demonstrates Its Importance for pH Regulation in Tumors. *Cancer Res.* **75**, 4109–4118 (2015).
25. Chaumeil, M. M. *et al.* Non-invasive in vivo assessment of IDH1 mutational status in glioma. *Nat. Commun.* **4**, 1–12 (2013).
26. Witney, T. H., Kettunen, M. I. & Brindle, K. M. Kinetic modeling of hyperpolarized 13C label exchange between pyruvate and lactate in tumor cells. *J. Biol. Chem.* **286**, 24572–24580 (2011).

Chapter 4: Functional genetic screening enables theranostic molecular imaging in cancer

4.1: Introduction

This chapter is adopted from an article by Perkons et al. that was submitted for consideration for publication to *Clinical Cancer Research* in Spring 2020. The chapter demonstrates that genetic screens can facilitate selection of targeted imaging probes and therapies. As a proof-of-principle, in hepatocellular carcinoma (HCC), assessment of flux through lactate dehydrogenase (LDH), an essential enzyme, quantified intratumoral efficacy of a targeted inhibitor and predicted response.

4.2: Abstract

Contemporary precision medicine initiatives emphasize the importance of developing targeted therapies alongside matched diagnostic tests. We demonstrate that functional genetic screening can address this deficiency by integrating target identification with imaging probe selection. Analyses of genetic screening data identified metabolic vulnerabilities in 17 unique cancer types that could be imaged with existing probes. Among these data, LDH was identified as a specific dependency of HCC, suggesting pyruvate metabolism as a sensitive and functional biomarker of HCC. As a proof-of-principle, LDH inhibition (LDHi) and dynamic nuclear polarization magnetic resonance spectroscopic imaging (DNP-MRSI) of LDH enzymatic activity using hyperpolarized [1-^{13}C]-pyruvate were validated as an *in vivo*, disease-specific theranostic approach for HCC, enabling the quantification of intratumoral LDHi pharmacokinetics and the prediction of therapeutic efficacy.

4.3: Introduction

Targeted therapies developed through mechanism-based drug discovery are revolutionizing cancer care, enabling improved patient outcomes and motivating patient-specific treatment strategies that form the basis of precision medicine[1]. Despite this promise, early experiences with these approaches support the need for integrated response assessment to further inform therapy[2]. Current molecular imaging paradigms, including ^{18}Fluorodeoxyglucose Positron Emission Tomography (FDG-PET), enable functional readouts of cellular metabolism, but have limited specificity in evaluating therapeutic efficacy given that the imaging phenotype is frequently not a direct readout of the targeted vulnerability. This deficiency has limited the translation of molecular imaging approaches despite the development of a myriad of molecular probes among a spectrum of imaging modalities. Hepatocellular carcinoma (HCC), the fastest rising cause of cancer death in the United States, represents a compelling clinical example of this deficiency[3]. Despite proven survival benefits for targeted therapies, current clinical imaging fails to effectively quantify therapeutic response[4]. Integrated theranostic strategies that enable the selection of molecular imaging probes specific for targetable vulnerabilities in cancer hold the potential to overcome this fundamental limitation in targeted cancer therapy.

Massively parallelized biotechnologies are transforming the discovery and development of targeted therapeutics. Among these, genetic screens using CRISPR-based genome editing enable the high-throughput and unbiased identification of potentially targetable vulnerabilities[5]. In addition to identifying therapeutic dependencies, existing functional annotations may enable the simultaneous identification of functional imaging probes modified by the target. Until recently, existing molecular imaging technologies had limited capacity to assess *in vivo* enzyme function or inform drug pharmacodynamics given that doing so requires distinguishing the parent substrate from its product. The advent of dynamic nuclear polarization enhanced ^{13}C nuclear magnetic resonance spectroscopic imaging (DNP-^{13}C-MRSI) overcomes this limitation through the ability to measure multiple chemical species simultaneously. This technique increases the fraction of nuclei aligning with an external magnetic field relative to a Boltzmann prediction of thermal equilibrium, producing up to a 10^5-fold increase in signal-to-noise and enabling the detection of stable ^{13}C-labeled isotopes in real-time[6]. Relative enzyme abundance and activity influence DNP-^{13}C-MRSI label conversion so that cellular enzymatic dependencies may facilitate the selection of DNP-^{13}C-MRSI probes that specifically measure enzymatic activity[7,8].

We hypothesized that CRISPR-based negative selection screening of enzymes responsible for DNP-^{13}C-MRSI probe metabolism would simultaneously identify therapeutic targets and molecular imaging probes, enabling a novel and high-throughput theranostic paradigm with the potential to assess and predict response.

4.4: Results

To evaluate the utility of functional genetic screening for therapeutic target identification and probe selection, we analyzed the DepMap Public 19Q3 dataset, which includes negative selection CRISPR screens targeting >18K genes in 625 cancer lines[9,10]. Using the provided cancer type annotations, we tailored our analysis to isolate differential vulnerabilities, identifying proteins most essential to growth (Supplementary Table 1). These data were then filtered to isolate differentially essential enzymes for which DNP-^{13}C-MRSI probes are used to measure enzymatic flux (Figure 4.1A, Figure 4.S1, Table 4.S1). Of the 29 different cancer types investigated, 17 demonstrated targetable dependencies that may be imaged using an established DNP-^{13}C-MRSI probe (Figure 4.1A and 4.S1; Tables 4.S1, 4.S2 and 4.S3). In addition, analysis of the top five differentially essential genes revealed potential targets for 4 of the remaining cancer types (Figure 4.1A and 4.S1; Table 4.S1).

As proof-of-principle, these analyses were also performed for HCC, a subset of the liver related cancers in the DepMap data. Initial investigation of differentially essential genes identified lactate dehydrogenase A (LDHA)—the predominant isoform of LDH and a known molecular imaging target—as the most differentially essential enzyme (p=5.32e-

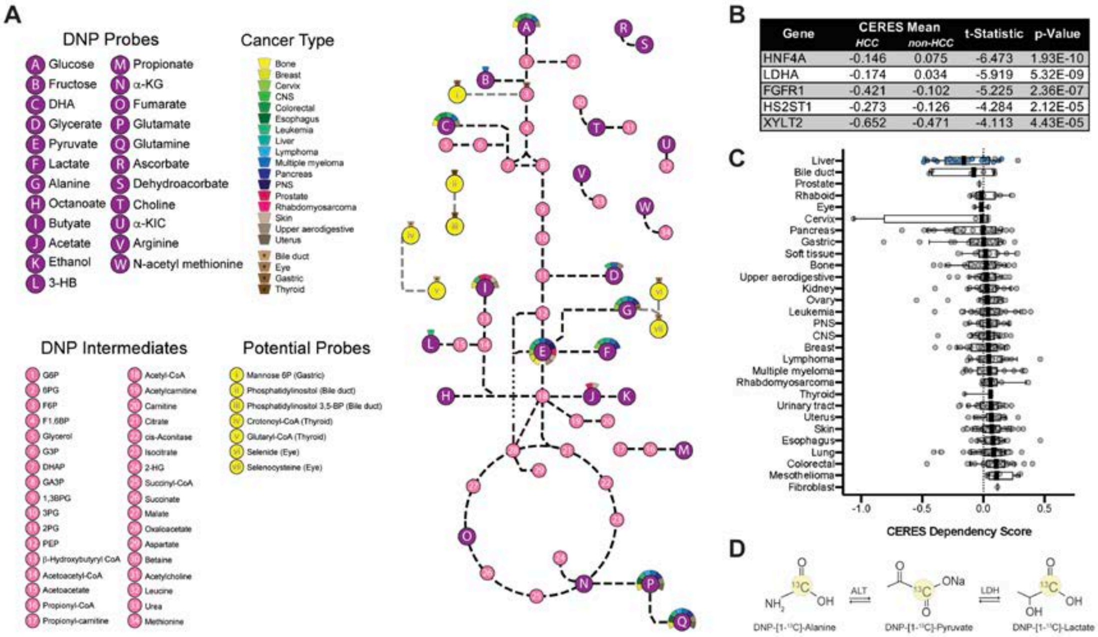
A
DNP Probes
A Glucose
B Fructose
C DHA
D Glycerate
E Pyruvate
F Lactate
G Alanine
H Octanoate
I Butyate
J Acetate
K Ethanol
L 3-HB
M Propionate
N α-KG
O Fumarate
P Glutamate
Q Glutamine
R Ascorbate
S Dehydroacorbate
T Choline
U α-KIC
V Arginine
W N-acetyl methionine
Cancer Type
Bone
Breast
Cervix
CNS
Colorectal
Esophagus
Leukemia
Liver
Lymphoma
Multiple myeloma
Pancreas
PNS
Prostate
Rhabdomyosarcoma
Skin
Upper aerodigestive
Uterus
Bile duct
Eye
Gastric
Thyroid
DNP Intermediates
1 G6P
2 6PG
3 F6P
4 F1,6BP
5 Glycerol
6 G3P
7 DHAP
8 GA3P
9 1,3BPG
10 3PG
11 2PG
12 PEP
13 β-Hydroxybutyryl CoA
14 Acetoacetyl-CoA
15 Acetoacetate
16 Propionyl-CoA
17 Propionyl-carnitine
18 Acetyl-CoA
19 Acetylcarnitine
20 Carnitine
21 Citrate
22 cis-Aconitase
23 Isocitrate
24 2-HG
25 Succinyl-CoA
26 Succinate
27 Malate
28 Oxaloacetate
29 Aspartate
30 Betaine
31 Acetylcholine
32 Leucine
33 Urea
34 Methionine
Potential Probes
i Mannose 6P (Gastric)
ii Phosphatidylinositol (Bile duct)
iii Phosphatidylinositol 3,5-BP (Bile duct)
iv Crotonoyl-CoA (Thyroid)
v Glutaryl-CoA (Thyroid)
vi Selenide (Eye)
vii Selenocysteine (Eye)
B
C
Liver
Bile duct
Prostate
Rhaboid
Eye
Cervix
Pancreas
Gastric
Soft tissue
Bone
Upper aerodigestive
Kidney
Ovary
Leukemia
PNS
CNS
Breast
Lymphoma
Multiple myeloma
Rhabdomyosarcoma
Thyroid
Urinary tract
Uterus
Skin
Esophagus
Lung
Colorectal
Mesothelioma
Fibroblast
-1.0
-0.5
0.0
0.5
CERES Dependency Score
D
NH2
OH
ONa
OH
ALT
LDH
DNP-[1-13C]-Alanine
DNP-[1-13C]-Pyruvate
DNP-[1-13C]-Lactate

Gene	CERES Mean		t-Statistic	p-Value
	HCC	non-HCC		
HNF4A	-0.146	0.075	-6.473	1.93E-10
LDHA	-0.174	0.034	-5.919	5.32E-09
FGFR1	-0.421	-0.102	-5.225	2.36E-07
HS2ST1	-0.273	-0.126	-4.284	2.12E-05
XYLT2	-0.652	-0.471	-4.113	4.43E-05

Figure 4.1: Functional genetic screening enables simultaneous selection of therapeutic targets and imaging probes.
A. Schematic depicting metabolic pathways that can be analyzed with DNP probes. Purple nodes correspond to previously polarized probes. Pink nodes correspond to intermediates that have either been (i) directly visualized after injection of a DNP probe or (ii) have not been directly identified but precede a downstream intermediate that has been directly visualized. Yellow nodes correspond to metabolites that may serve as future molecular imaging probes, as suggested by the data provided in Supplementary Table 1. Dashed lines correspond to an enzyme or group of enzymes connecting DNP probes and/or intermediates. Colored semi-circles correspond to cancer types that may be imaged with a given DNP probe, as described in Table 4.S1. Figure 4.S1 situates this network of probes in the broader metabolome. B. Table highlighting the top five differentially essential genes in 20 HCC lines, when compared to other cancer types in the DepMap 19Q3 dataset. C. Dot plot depicting the relative essentiality of LDHA in different tumors types (as annotated in the DepMap 19Q3 dataset) based upon CERES score. Individual dots represent unique cell lines (n=625). Blue dots highlight HCC cell lines (n=20). Dark lines depict the median CERES score within tumor groups. D. Schematic illustrating the metabolism of DNP-[1-^{13}C]-pyruvate by LDH and ALT to DNP-[1-^{13}C]-lactate and DNP-[1-^{13}C]-alanine, respectively.

9; Figure 4.1B, C)[9,10]. Interestingly, FGFR1, one of several proteins inhibited by HCC therapies lenvatinib and sorafenib, was the third most differentially gene (p=2.36e-7; Figure 4.1B); however, LDHA was the only imageable dependency isolated in HCC among significantly depleted genes (Table 4.S1)[11].

To validate these findings, we developed a focused CRISPR screening library adapted to enable high-throughput screening of theranostic probes including guides targeting enzymes that metabolize established DNP molecular imaging agents, and requiring as few as 4e6 cells (Figure 4.1A)[6,12]. To validate our library, we performed negative selection screens in an established HCC cell line included in the DepMap dataset (SNU-449). The results confirmed the essentiality of LDHA in these cells (LFC=-1.098, p=4.98e-6, FDR=6.3e-5). We then performed a negative selection CRISPR screen in a primary HCC cell line (PGM-898) generated in our laboratory from a patient-derived xenograft, further confirming an LDH dependency (LFC=-0.380, p=0.035, FDR=0.175).

LDHA enzymatically converts pyruvate to lactate, while also regenerating NAD+ (Figure 4.1D). DNP-[1-^{13}C]-pyruvate is a molecular imaging probe that, when metabolized to form lactate, quantifies local LDH activity[6,13,14]. To test a theranostic strategy combining LDH inhibition (LDHi) with DNP-^{13}C-MRSI assessment of LDH activity, autochthonous HCCs were chemically induced in male Wistar rats using diethylnitrosamine. To identify whether DNP-[1-^{13}C]-pyruvate could be used to measure LDHi pharmacodynamics, we performed MRSI of DNP-[1-^{13}C]-pyruvate before and after intravenous injection of an LDH inhibitor at either 10 mg/kg (n=6) or 20 mg/kg (n=3). In all cases, LDHi administration led to the near complete abrogation of lactate production, which manifested as decreases in the lactate-to-total carbon (t=6.20, df=8, p=2.58e-4, n=9) and lactate-to-pyruvate ratios (V=45, p=3.91e-3, n=9; Figure 4.2C). Consistent with the assumption of transport-limited metabolism of DNP-probes, LDH inhibition also led to increases pyruvate-to-total-carbon (t=4.40, df=8, p=2.28e-3, n=9), alanine-to-total-carbon (t=2.82, df=8, p=2.23e-2, n=9), alanine-to-pyruvate (t=2.34, df=8, p=4.71e-2, n=9), and alanine-to-lactate (t=4.35, df=9, p=2.45e-3, n=9).

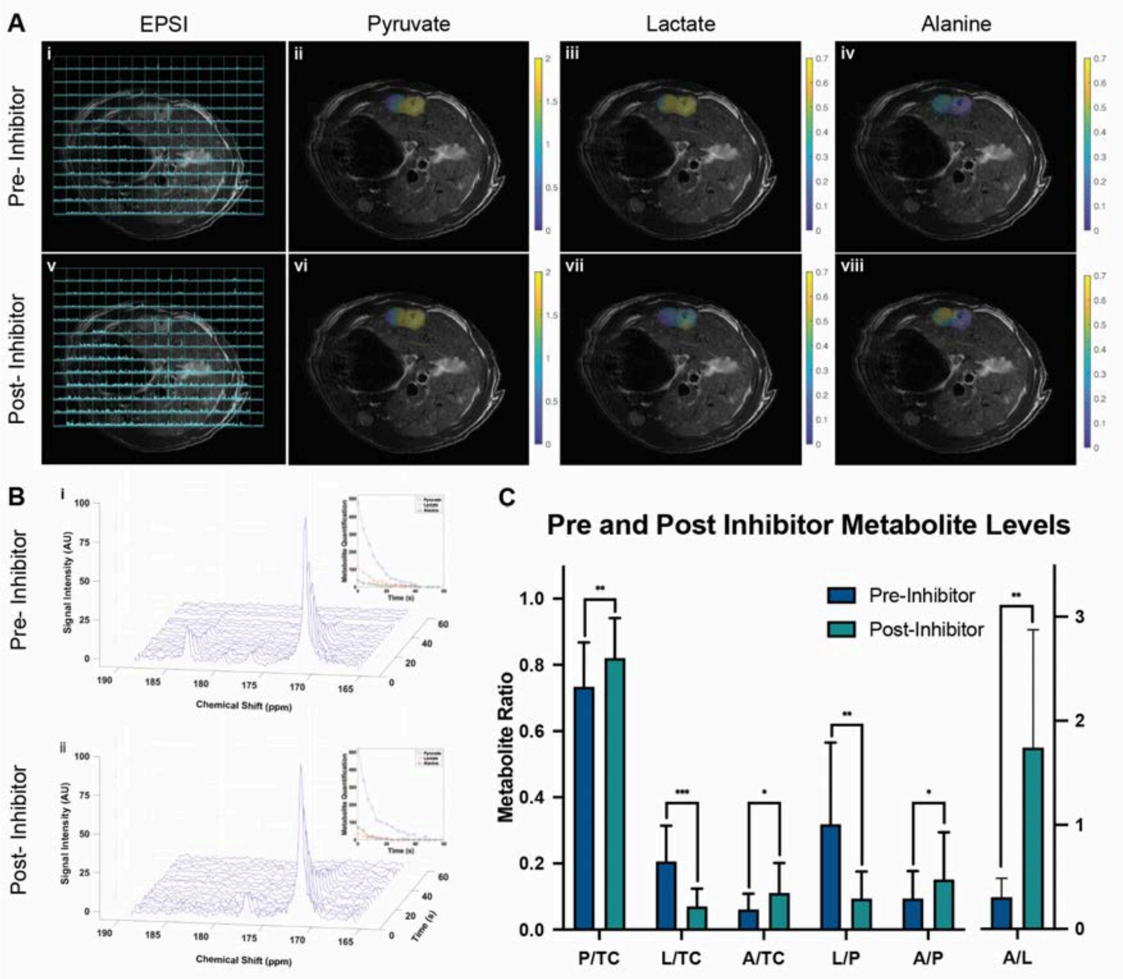

Figure 4.2: DNP-^{13}C-MRSI quantifies intra-tumoral LDH activity *in vivo*

A. DNP-MRS images following injection of hyperpolarized 1-^{13}C-pyruvate enable the quantification of metabolism before (i-iv) and after (v-vii) administration of an LDHi. Panels i and v display spectra re-constructed from each voxel after EPSI overlaid on to T2W ^{1}H images. Panels ii-iv and vi-viii display parametric maps of intratumoral pyruvate, lactate and alanine signals before and after LDHi. These data demonstrate an increase in intratumoral pyruvate, decrease in intratumoral lactate, and increase in intratumoral alanine after LDHi. B. Stacked spectra demonstrate the evolution of intratumoral pyruvate (170.4 ppm), lactate (183.35 ppm), and alanine (176.5 ppm) before (i) and after (ii) LDHi, again demonstrating a marked reduction in lactate formation. The inserts in the upper-right correspond to integrals of each metabolite peak. C. Bar graph of changes in measured intratumoral metabolite ratios following LDHi administration, including: ↑pyruvate-to-total carbon (n=9, p<0.01), ↓lactate-to-total carbon (n=9, p<0.001), ↑alanine-to-total carbon (n=9, p<0.05), ↓lactate-to-pyruvate (n=9, p<0.01), ↑alanine-to-pyruvate (n=9, p<0.05) and ↑alanine-to-lactate (n=9, p<0.01).

Given that LDH knock-out slowed HCC growth *in vitro*, the therapeutic efficacy of LDHi was assessed *in vivo*. Tumor volumes measured from T2-weighted images taken before and after inhibitor administration were used to quantify tumor doubling time. A single dose of an LDH inhibitor at either 10 mg/kg (n=6) or 20 mg/kg (n=3) was found to significantly slow tumor growth (V=44, p=7.81e-3, n=9; Figure 4.3A). The strength of this effect increased when using a 20 mg/kg injection compared to a 10 mg/kg injection (t=3.87, df=3.35, p=2.51e-2, n=6 at 10mg/kg and n=3 at 20 mg/kg; Figure 4.3B).

DNP-MRS data were further analyzed to assess the ability to predict therapeutic response at the time of drug administration. Interestingly, intratumoral alanine production after LDHi robustly predicted the degree of growth inhibition (p=4.04e-4). In addition, the intratumoral level of alanine following LDHi was confirmed as a predictive biomarker when

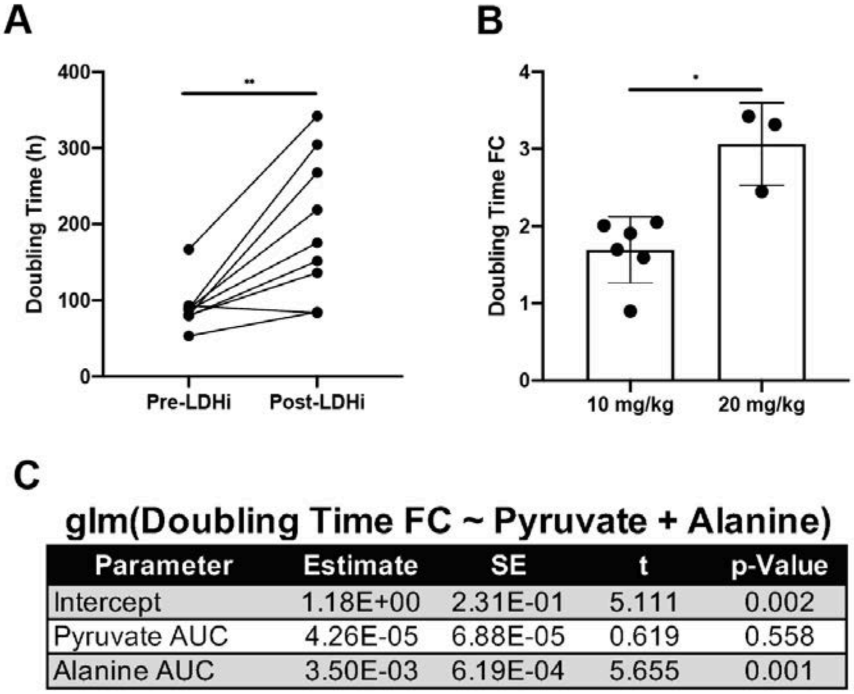

glm(Doubling Time FC ~ Pyruvate + Alanine)

Parameter	Estimate	SE	t	p-Value
Intercept	1.18E+00	2.31E-01	5.111	0.002
Pyruvate AUC	4.26E-05	6.88E-05	0.619	0.558
Alanine AUC	3.50E-03	6.19E-04	5.655	0.001

Figure 4.3: LDHi slows HCC growth, as predicted by DNP-[1-^{13}C]-pyruvate metabolism
A. LDHi administration slowed tumor growth, leading to an increase in doubling time of these tumors (n=9, p<0.01). B. Bar graphs demonstrating dose-dependent tumor growth delay following LDHi, (n=6 at 10 mg/kg and n=3 at 20 mg/kg, p<0.05). C. Table showing the dependence of the tumor growth delay on the amount of Alanine measured after LDHi using a generalized linear model (n=9, p<0.01).

controlling for multiple potential co-variates, including post-inhibitor pyruvate levels (p=1.31e-3; Figure 4.3C), pre-inhibitor alanine levels (p=5.59e-3), and post-inhibitor pyruvate and lactate levels (p=5.87e-3). Post-inhibition intratumoral lactate, which uniformly approached the limit of detection, did not predict response, likely secondary to insufficient sensitivity.

Taken together, these data demonstrate that functional genetic screening informs a theranostic paradigm leveraging DNP-^{13}C-MRSI to assess drug pharmacodynamics to predict therapeutic efficacy.

4.5: Discussion

Functional genetic screening identified imageable metabolic vulnerabilities in 17 unique cancer types. Among these, we demonstrate that LDHA is a differential vulnerability of HCC, highlighting DNP-[1-^{13}C]-pyruvate as a consequent functional biomarker of HCC and its response to LDH inhibition. This data is consistent with LDH's demonstrated role in enabling aerobic glycolysis in cancer, including in HCC[15]. Independently, clinical data has demonstrated that both serum lactate and serum LDH levels can be used as prognostic biomarkers of HCC[16,17]. The confirmation that LDH inhibition led to a change in the growth dynamics of HCC *in vivo* suggests the potential utility of pursuing LDH inhibition as a therapy for HCC. A single dose of LDHi increased tumor doubling times in a dose-dependent manner suggesting that higher doses, repeat injections or local administration may enable tumor regression and/or mitigate HCC recurrence.

The variability of individual dependencies both within and across cancer types, including LDHA, supports the potential of metabolic imaging to inform clinical use of targeted therapies. While a majority of HCC cell lines included in the DepMap 19Q3 dataset demonstrated a dependence on LDHA for growth, several did not. Moreover, a recent clinical study in prostate cancer demonstrated that lactate generation from DNP-[1-^{13}C]-pyruvate predicts tumor grade[18]. As a highly regulated metabolic enzyme, assessments of *in vivo* LDH flux with DNP-[1-^{13}C]-pyruvate MRSI may serve to stratify patients and predict response to targeted systemic or locoregional therapies beyond LDHi alone[14,19]. Future clinical studies will help assess the predictive value of DNP-[1-^{13}C]-pyruvate MRSI in this broader context.

Given inherent dependency variability within and between cancers, curated screens—including those performed with the DNP-focused library—minimize experimental complexity and requisite cell number, enabling confirmation of potential therapeutic and imaging targets in patient-derived samples. Moreover, unbiased screening—including screens within the DepMap datasets—can independently isolate alternative dependencies, suggesting avenues for future therapy and imaging probe development. Indeed, a wider, unbiased analysis limited to the top 5 differentially essential genes identified potential metabolic imaging targets for the four cancer types for which the DepMap screens did not identify a DNP-associated dependency. While the current study leveraged the unique capability of DNP-^{13}C-NMRS imaging to measure enzyme function based on direct measurements of the administered substrate and its metabolites, the described paradigm is generalizable to other imaging modalities. This screening approach can be readily expanded to include targets of other molecular imaging probes including the extensive repertoire of PET-based radiotracers already developed for oncologic imaging[20].

In summary, the described study demonstrates that biologically motivated therapeutic and imaging probe selection through genetic screening enables a high throughput theranostic paradigm in oncology. In the era of precision medicine, wherein patient-derived samples are increasingly utilized to inform management, this approach represents a novel strategy to overcome existing barriers and facilitate the application of molecular imaging at the bench as well as at the bedside.

4.6: Methods

CRISPR Screening

DepMap Analyses

The DepMap 19Q3 release was utilized for analysis of CRISPR screen data. All data cleaning and analyses were performed using RStudio Desktop 1.1.442[9,10]. The cancer types of individual cell lines in this dataset reflect the primary lineage included in the sample descriptions. HCC lines (n=20) were manually identified from the broader lineage of liver cancer lines (n=22). To isolate the most differentially essential genes in individual cancers, two group comparisons were performed. Empirical Bayes moderated t-statistics are reported[21] and genes are ranked based upon the p-value of these statistics. Differentially essential genes in a given cancer type are defined by those (i) maintain a mean CERES score < 0 and (ii) have a lower CERES score than that gene in other cancer types ($p<0.0005$; two-sided comparison).

Knock-out library generation

To isolate enzymatic dependencies of cancer cells that could be imaged with DNP-^{13}C-NMRS, a CRISPR knock-out (KO) library targeting enzymes capable of metabolizing DNP-^{13}C-NMRS probes was developed. The guide library was optimized to satisfy the following: (i) small overall library size (4000 guides) to facilitate high cell-per-guide (~1000) ratios during screening, (ii) a high guide-to-gene ratio (10) to enhance assessments of significance, and (iii) a high fraction of control guides in the population (~10%) to estimate drift. A list of DNP-^{13}C-NMRS probes that had been previously used *in* *vivo* or *in vitro*, and whose metabolism or conversion to at least one additional species had been confirmed previously was compiled[6,22]. These requirements were designed to ensure the biologic relevance of included probes, and further served to limit consideration of probes to those with sufficiently long T_1 relaxation times with high polarizability and solubility in a physiologic buffer required for application[6,12]. 36 unique DNP-^{13}C-NMRS probes met these criteria. To identify enzymes to include in the KO library, a list of metabolite pairs was created consisting of DNP-^{13}C-NMRS probes and their corresponding metabolites (or intermediates thereof) observed yielding 56 metabolite pairs. A Uniprot search was performed including both members of a given pair, filtering for human enzymes that had been reviewed as of January 2017, yielding 180 *primary* proteins [23]. In addition to these proteins, 66 *secondary* proteins pertinent to autophagy and the stability of hypoxia inducible factors were added. To facilitate redundancy in the library, 110 *tertiary* proteins were also added using String, a database of protein network interactions, enabling the identification of many as five proteins that serve as high confidence (>0.7) activators or inhibitors of the *primary* or *secondary* proteins previously isolated. In total, the protein library consisted of 356 unique proteins[24]. Using CRISPR Focus, 10 CRISPR-Cas9 spacer sequences for single guide RNAs (sgRNA) were generated per gene, which were pooled with 106 positive controls and 354 negative controls to produce a final library of 4,000 unique sequences[25]. These sequences were amplified based upon previously published protocols and subsequently cloned them into a LentiCRISPR v2 backbone, amplified and isolated the modified plasmid from bacteria, and generated lentivirus using HEK-293T cells[26–28].

Screen design

Using the targeted library, screening was performed for metabolic dependencies of two HCC lines (n=2 per cell line), SNU-449 and PGM-898. SNU-449 cells were purchased from ATCC. The PGM-898 cell line, developed by our laboratory, was derived from a percutaneous HCC biopsy of a human patient that was expanded in an immune-compromised mouse. The identity of this HCC cell line was confirmed via histology and targeted sequencing of known mutations in the original biopsy.

For each cell line, preliminary testing included quantification of puromycin sensitivity and calculation of viral titer of with the lentiviral library, permitting estimation of the viral amount required to achieve a target multiplicity of infection (MOI) of 0.3 so that the majority of infected cells would incur a single KO[29]. After quantifying viral titer and puromycin sensitivity, two screens were performed in each line, targeting a cell-per-guide (CPG) ratio >500 at a target MOI of 0.3; approximately 12e6 cells were required to initiate each screen. These cells were initially cultured on a tissue culture treated surface of either 182 cm^2 flasks for SNU-449 cells or 60.8 cm^2 plates pre-coated with 1% Matrigel in basal Dulbecco's Modified Eagle's medium (DMEM) for PGM-898 cells, targeting 15% confluence. SNU-449 cells were cultured at 21% O_2 in RPMI medium, with 10% fetal bovine serum (FBS), 1% penicillin-streptomycin, 10 mM D-glucose and 2 mM L-glutamine. PGM-898 cells were cultured at 3% O_2 in medium empirically determined to promote growth, which was composed of Advanced DMEM F/12, supplemented with 10% FBS, 10 μM Rock Inhibitor, 1% Glutamax, 1% HEPES, 1% Penstrep and 0.1% amphotericin B.

On the day following initial plating, media was removed, and the viral amount required to achieve a MOI of 0.3 in each cell line was added to flask in fresh culture media containing polybrene. Puromycin selection was performed for up to three days (at the concentration found to kill 95% of naïve cells within 72 hours) in fresh media. At the end of selection, cells were removed from culture plates by applying 0.25% Trypsin-EDTA for

10 minutes. The cells from all plates were pooled together. The MOI was calculated using control plates that had not received virus or/nor puromycin (average MOI: 0.23 for SNU-449, 0.31 for PGM-898), confirming sufficient CPG at the time of viral application. At this juncture, 4e6 cells (1000 CPG) or 50% of the cells recovered from trypsinization, whichever was fewer, were re-plated. The remaining cells were spun down, washed with PBS, and then stored at -80C for subsequent analyses; cell samples from this time point, prior to the initiation of screening, were used as a baseline in the subsequent measures of depletion. Re-plated cells were cultured for a minimum of 7 additional days, reflecting the screening period of the experiments. On day 3 or 4 of the screen (SNU-449 and PGM-898, respectively), all cell culture plates were again pooled together and 4e6 cells (1000 CPG) or 50% of the cells recovered from trypsinization, whichever was fewer, were re-plated while the remainder was washed and stored for subsequent analyses. On day 7 or 8 of the screen (SNU-449 and PGM-898, respectively), all remaining cells were washed and stored for subsequent analyses.

Targeted sequencing of sgRNA abundance

At the conclusion of each experiment, targeted sequencing of the sgRNA sequencing (flanked by a constant region common to all plasmids in the library) of cells obtained from each time point was performed. Briefly, genomic extraction from resuspended cell pellets from each of the timepoints of interest was performed followed by amplification of the spacer region of each sgRNA via PCR, attachment of next-generation sequencing adapters via PCR, gel extraction of the ~350 bp PCR product, and concentration-based pooling of samples for NGS[29,30].

Analyses of guide depletion using MAGECK

Analysis of negative selection screens was performed using MAGECK, which provides a composite measure of gene essentiality by analyzing the relative fold-change in replicate guide sequence representation for individual genes relative to negative control guides over time[31,32]. Significantly depleted guides were determined using the test function, comparing the abundance of guides between the initial and final screening time points. The relative abundance of the 354 negative control guides were also included for normalization. The alphamedian input option was used to compare gene log-fold changes with a gene-test-fdr-threshold of 0.05. Genes found to have a p-value <0.05 and FDR <0.25 were considered significantly depleted.

Animal experiments

Autochthonous rat model of Hepatocellular Carcinoma (HCC)

Induction of autochthonous HCCs in male Wistar rats was performed as described previously[33]**.** Briefly, two weeks after arrival to the colony, 0.01% diethylnitrosamine (DEN) was administered ad libitum for 12 weeks[14,33–35]. Beginning one week prior to the end of the diet, rats underwent screening MRI approximately twice per week with T2-weighted MRI (FOV: 70 mm x 70 mm, Grid size: 256 x 256, Slice thickness: 2 mm, TR minimum: 1.4 s (respiratory gated), TE: 59.1 ms, Minimum averages: 4) using an Agilent 4.7T, 40 cm horizontal bore MR Spectrometer with a 25 gauss/cm gradient tube interfaced to an Agilent DirectDrive console[14]. During all scans induction and maintenance of anesthesia was achieved using ~2% isoflurane in O_2, temperature was maintained at 37° C with a closed loop heating system (Small Animal Instruments), and respiration rate was monitored. Each animal was positioned within a Polarean proton-tuned (200.1 MHz) birdcage resonator. After individual HCC lesions reached ~100 mm^3 in size, they were used for subsequent study with an LDH inhibitor (737) graciously provided by Dr. Len

Neckers and the NCI Experimental Therapeutics Program[36,37]. Following inhibitor administration, animals underwent repeated screening with T_2-weighted MRI approximately twice per week.

DNP-[1-^{13}C]-pyruvate and LDHi injections

On the day of therapeutic treatment with LDHi, the animal was centered within a Polarean proton-tuned (200.1 MHz) birdcage resonator with a ^{13}C-tuned (50.525 MHz) surface coil positioned over the right upper quadrant. T2-weighted imaging (as described above) was performed to confirm positioning of the surface coil over the tumor of interest using a ^{13}C-urea phantom centered within the surface coil[14]. Each animal then received a baseline DNP-[1-^{13}C]-pyruvate injection followed by a LDHi injection within 15 minutes, and then a follow-up DNP-[1-^{13}C]-pyruvate injection within 90 minutes of LDHi administration (n=9).

The composition and timing of DNP-[1-^{13}C]-pyruvate injections were identical prior to and following LDHi administration for each single animal using a concentration of 80 mM DNP-[1-^{13}C]-pyruvate. DNP-[1-^{13}C]-pyruvate was prepared by polarizing a mixture of 14 M [1-^{13}C]-pyruvate (Cambridge Isotopes), 15 mM OX063 radical (GE Healthcare) and 1.5 mM of Dotarem (Guerbet LLC) at ~1.4 K and an excitation frequency of ~94.080 GHz in a HyperSense hyperpolarizer (Oxford Instruments). Upon saturation of polarization transfer, dissolution was performed in a buffer designed to ensure that the final injected solution was iso-osmolar to blood (300 mOsm) at pH of 7.4 with a final pyruvate concentration of 80 mM. Injections were either performed by hand (n=3) or with the assistance of a high-pressure liquid chromatography (HPLC) pump through PEEK tubing (n=6) at a dose of 4 mL/kg (n=5) or 6.7 mL/kg (n=4). DNP-^{13}C-NMRS was performed using a 2D spectroscopic imaging (EPSI) sequence with a spectral bandwidth of 1.1kHz and

128 points, enabling detection of a chemical shift range of 22 ppm [14,38]. The total FOV was 60 mm x 45 mm with 12 phase encoded steps and 16 frequency encoded steps, enabling an in-plane resolution of 3.75 mm x 3.75 mm with a slice thickness matching the thickness of the tumor in the coronal plane (~6-10 mm). Each image was acquired in ~1 s with consecutive images repeated every ~2 s for a minimum of 20 scans per study.

LDHi injections were performed at a concentration of 10 mg/mL and a dose of either 10 mg/kg (n=6) or 20 mg/kg (n=3). All LDHi injections were performed by hand through tail vein injection at a rate of 1 mL/min and were followed by a 2 mL saline flush.

Image reconstruction and metabolic flux analysis

Acquired proton images and EPSI spectra were reconstructed in MATLAB 2018B (Mathworks, Inc.). To ensure accurate quantitation of the carbon data, the following corrections were employed: B_1 correction, point spread function correction, polarization efficiency normalization, and baseline subtraction consistent with the methods as described previously and in Chapter 5[14]. Chemical shifts were determined relative to a ^{13}C-Urea reference standard (165.5 ppm) present in the ^{13}C surface coil. Intratumoral metabolites were determined using region of interest (ROI) analysis based on registration of EPSI images with T2-weighted images. To account for partial voxel effects, the sums of intratumoral resonances were determined from a 2D interpolation of the quantification corrected EPSI data using a cubic convolution (interpolation factor = 8). When intratumoral SNR for an individual image was ≥2, metabolite quantifications for individual images were calculated as the integral of metabolite peaks identified based on chemical shifts (pyruvate: 170.4 ppm, lactate: 183.35 ppm, alanine: 176.5 ppm). For images with insufficient SNR or for which metabolite integrals yielded negative values, metabolite quantifications were recorded as 0 for subsequent analyses. Total ^{13}C signal reflects the sum of quantified pyruvate, lactate, and alanine in an image. Kinetic analyses were performed by taking the AUC of metabolite quantifications from the EPSI series. Parametric maps were generated from cubic interpolation of metabolite quantifications (interpolation factor = 8).

Statistical analyses

Statistical analyses were performed in RStudio Desktop 1.1.442; graphical representations of these data were made using GraphPad Prism 8.2.1. Shapiro-Wilk tests for normality were performed for all two-group comparisons. Normally distributed data were compared with student t-tests, while non-normally distributed data were compared with Wilcoxon signed rank tests. A generalized linear model was used to assess prediction of growth slowing from imaging data.

4.7: Supplemental Figures

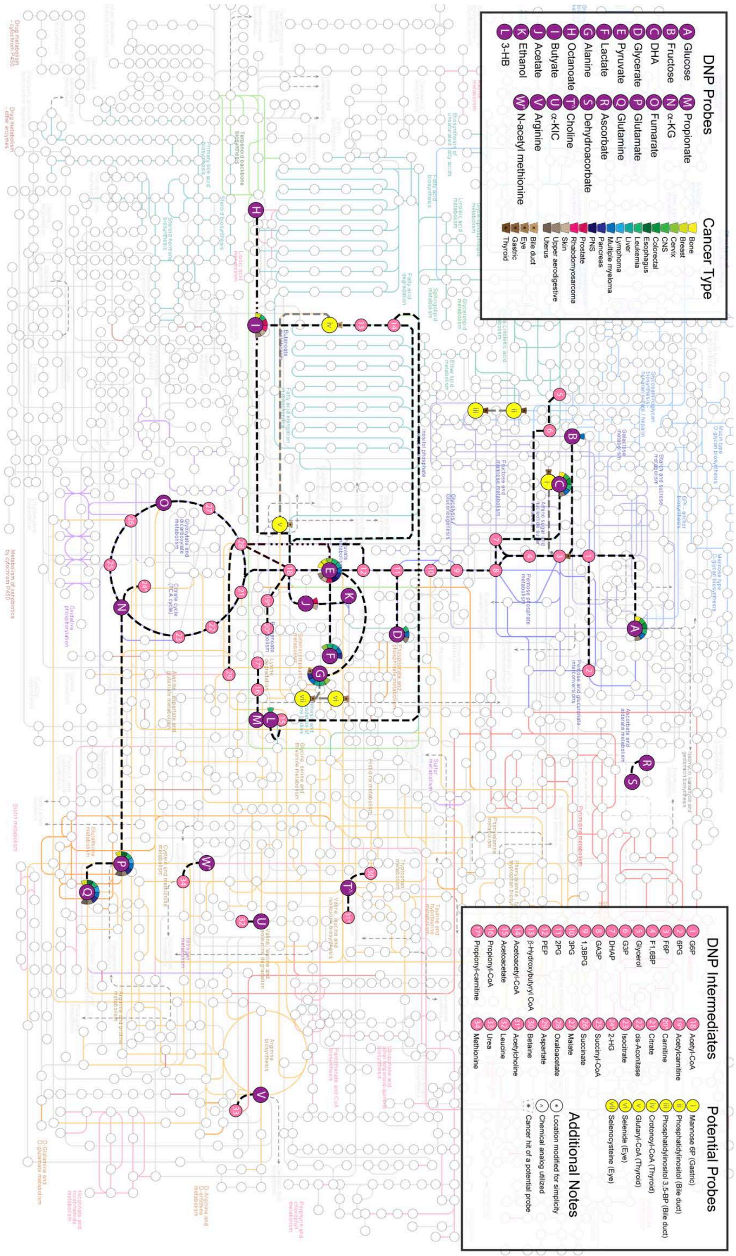
DNP Probes
A Glucose
B Fructose
C DHA
D Glycerate
E Pyruvate
F Lactate
G Alanine
H Octanoate
I Butyate
J Acetate
K Ethanol
L 3-HB
M Propionate
N α-KG
O Fumarate
P Glutamate
Q Glutamine
R Ascorbate
S Dehydroacorbate
T Choline
U α-KIC
V Arginine
W N-acetyl methionine
Cancer Type
Bone
Breast
Cervix
CNS
Colorectal
Esophagus
Leukemia
Liver
Lymphoma
Multiple myeloma
Pancreas
PNS
Prostate
Rhabdomyosarcoma
Skin
Upper aerodigestive
Uterus
Bile duct
Eye
Gastric
Thyroid
DNP Intermediates
1 G6P
2 6PG
3 F6P
4 F1,6BP
5 Glycerol
6 G3P
7 DHAP
8 GA3P
9 1,3BPG
10 3PG
11 2PG
12 PEP
13 β-Hydroxybutyryl CoA
14 Acetoacetyl-CoA
15 Acetoacetate
16 Propionyl-CoA
17 Propionyl-carnitine
18 Acetyl-CoA
19 Acetylcarnitine
20 Carnitine
21 Citrate
22 cis-Aconitase
23 Isocitrate
24 2-HG
25 Succinyl-CoA
26 Succinate
27 Malate
28 Oxaloacetate
29 Aspartate
30 Betaine
31 Acetylcholine
32 Leucine
33 Urea
34 Methionine
Potential Probes
i Mannose 6P (Gastric)
ii Phosphatidylinositol (Bile duct)
iii Phosphatidylinositol 3,5-BP (Bile duct)
iv Crotonoyl-CoA (Thyroid)
v Glutaryl-CoA (Thyroid)
vi Selenide (Eye)
vii Selenocysteine (Eye)
Additional Notes
* Location modified for simplicity
^ Chemical analog utilized
* Cancer hit of a potential probe

Figure 4.S1

Schematic depicting metabolic pathways that can be analyzed with DNP probes. The background of the figure is a representation of the KEGG human global metabolism map (01100) that was generated in R using Pathview. As in Figure 4.1A, purple nodes correspond to previously polarized probes. Pink nodes correspond to intermediates that have either been (i) directly visualized after injection of a DNP probe or (ii) have not been directly identified but precede a downstream intermediate that has been directly visualized. Yellow nodes correspond to metabolites that may serve as future molecular imaging probes, as suggested by the data provided in Table 4.S1. Dashed lines correspond to an enzyme or group of enzymes connecting DNP probes and/or intermediates. Colored semi-circles correspond to cancer types that may be imaged with a given DNP probe, as described in Table 4.S1.

4.8: Supplemental Tables

	Cancer type	Top 5 differentially essential genes	Imaging-associated differentially essential genes	DNP probes for imaging-associated differential essential genes	Potential novel protein-probe pairs *(when none otherwise identified)*
1	Bile Duct	VAC14, RAB10, FAM83H, TNPO2, TPCN2			VAC14: Phosphatidylinositol 3-phosphate, phosphatidylinositol 3,5-bisphosphate
2	Bone	TRIM8, ETV6, IGF2BP1, FLI1, STAG1	ALDOA, FTO	[2-13C]-Dihydroxyacetone, [U-2H, U-13C]-Glucose, [1-13C]-Pyruvate	
3	Breast	TRPS1, SPDEF, FOXA1, ESR1, TFAP2C	ACO2, GMPS, PFAS, SDHB	[1-13C]-Butyrate, [1-13C]-Glutamate, [1-13C]-Glutamine, [5-13C]-Glutamine, [1-13C]-Pyruvate, [2-13C]-Pyruvate	
4	CNS	RPP25L, JUN, VRK1, RPS21, PRKAR1A	GAPDH	[2-13C]-Dihydroxyacetone, [U-2H, U-13C]-Glucose	
5	Cervix	UBE3A, ZER1, LDHA, F2RL3, CKS1B	LDHA	[1-13C]-Alanine, [1-13C]-Lactate, [1-13C]-Pyruvate, [2-13C]-Pyruvate	
6	Colorectal	CTNNB1, TCF7L2, CDX2, KLF5, SATB2	ALDOC	[2-13C]-Dihydroxyacetone, [U-2H, U-13C]-Glucose	
7	Esophagus	REXO2, ERBB3, FIS1, TIMM17A, TP63	GATB, GATC	[1-13C]-Glutamate, [1-13C]-Glutamine, [5-13C]-Glutamine	
8	Eye	LHX3, OTX2, NEUROD1, SCLY, OTP			SCLY: Selenocysteine, alanine, selenium
9	Fibroblast	TERF2IP, FANCM, CHTF18, ATG16L1, RAB3GAP1			
10	Gastric	TCF7L2, CTNNB1, KLF5, MPI, HDAC4			MPI: Fructose-6-phosphate, mannose-6-phosphate
11	Kidney	PAX8, HNF1B, SEC23IP, CDH2, PARD3			
12	Leukemia	MYB, LMO2, RUNX1, GFI1, SLC5A3	CAD, CTPS1, DLD, GFPT1, GOT2, HMGCL, PFAS, PFKL, PPAT, SDHA, SDHB	[1,3-13C]-3-hydroxybutryate, [1-13C]-Alanine, [1-13C]-Butyrate, [2-13C]-Dihydroxyacetone, [U-2H, U-13C]-Glucose, [1-13C]-Glutamate, [1-13C]-Glutamine, [5-13C]-Glutamine, [1-13C]-Glycerate, [1-13C]-Lactate, [1-13C]-Pyruvate, [2-13C]-Pyruvate	
13	Liver	HNF4A, FGFR1, LDHA, HNF1A, HS2ST1	LDHA	[1-13C]-Alanine, [1-13C]-Lactate, [1-13C]-Pyruvate, [2-13C]-Pyruvate	
14	Lung	SMARCA2, NFE2L2, ASPM, ECM1, SUCO			
15	Lymphoma	SH3GL1, ITSN2, EBF1, BCL6, ATP1B3	GLS	[1-13C]-Glutamate, [1-13C]-Glutamine, [5-13C]-Glutamine	
16	Mesothelioma	PHLDB2, DUSP1, SLC19A2, FGFR1, KRTAP4			
17	Multiple myeloma	IRF4, PRDM1, POU2AF1, HERPUD1, NFKB1	CA14, CAD, GLS, HK2, PFAS	[1-13C]-Alanine, [2-13C]-Dihydroxyacetone, [2-13C]-Fructose, [U-2H, U-13C]-Glucose, [1-13C]-Glutamate, [1-13C]-Glutamine, [5-13C]-Glutamine, [1-13C]-Glycerate, [1-13C]-Lactate, [1-13C]-Pyruvate	
18	Ovary	PAX8, MECOM, PARD3, PARD6B, XPR1			
19	Pancreas	KRAS, DOCK5, ID1, WLS, ELMO3	GMPS, LDHA	[1-13C]-Alanine, [1-13C]-Glutamate, [1-13C]-Glutamine, [5-13C]-Glutamine, [1-13C]-Lactate, [1-13C]-Pyruvate, [2-13C]-Pyruvate	
20	PNS	ISL1, HAND2, MYCN, PHOX2B, PDK1	MDH1B	[1-13C]-Pyruvate	
21	Prostate	HOXB13, ERG, FKBP4, TLE3, GATA2	ACLY	[1-13C]-Acetate, [1-13C]-Butyrate, [1-13C]-Pyruvate, [2-13C]-Pyruvate	
22	Rhabdoid	DCAF5, NABP2, PUM3, SIVA1, QRICH1			
23	Rhabdomyosarcoma	MYOD1, PAX3, MYOG, SOX8, ZBTB18	HSD17B12	[1-13C]-Butyrate	
24	Skin	SOX10, MITF, BRAF, DUSP4, MAPK1	ACLY	[1-13C]-Acetate, [1-13C]-Butyrate, [1-13C]-Pyruvate, [2-13C]-Pyruvate	
25	Soft Tissue	MEOX2, SACS, CHRNA4, FOXC2, SS18			
26	Thyroid	GCDH, PDGFRA, LRMP, RPL26, RPS27			GCDH: Glutaryl-CoA, crotonyl-CoA
27	Upper aerodigestive	TP63, EGFR, ERBB2, ITGB1, ITGA3	ENO1, PC, PSAT1	[1-13C]-Butyrate, [2-13C]-Dihydroxyacetone, [U-2H, U-13C]-Glucose, [1-13C]-Glutamate, [1-13C]-Glutamine, [1-13C]-Glycerate, [1-13C]-Pyruvate, [2-13C]-Pyruvate	
28	Urinary tract	PPARG, SOX4, TP63, TEAD3, RXRA			
29	Uterus	CCNE1, PAX8, WRN, MECOM, CCDC102A	GLUL	[1-13C]-Glutamate, [1-13C]-Glutamine, [5-13C]-Glutamine	
30	HCC*	HNF4A, LDHA, FGFR1, HS2ST1, XYLT2	LDHA	[1-13C]-Alanine, [1-13C]-Lactate, [1-13C]-Pyruvate, [2-13C]-Pyruvate	

Table 4.S1: Differentially essential genes by cancer type.
This table, organized by cancer type, includes: (1) the top five differentially essential genes in each cancer type, (2) imaging-associated differentially essential genes (where $p<0.0005$), (3) DNP-probes associated with imaging genes identified in (2) as described by supplementary tables 2 and 3, and (4) identifies novel potential protein-probe pairs among genes listed in (1) when no imaging associated genes were identified in (3). Differentially essential genes must meet two criteria: (1) the mean CERES score for the cancer type must be < 0 and (2) the mean CERES score must be statistically less than that of all other cancer types studies ($p<0.0005$). *: HCC is a subset of liver cancers.

	Citation (First_Last_Year)	**DNP Agent**	**Parent metabolite(s)**	**Child metabolite(s)**	**Enzyme(s)**
1	Chen_Cunningham_2010	[1-13C]-N-acetyl-L-methionine	N-acetyl-L-methionine	Methionine	ACY1
2	Lerche_ArdenkjaerLarsen_2010	13C-Carbamazepine	Carbamazepine	Carbamazeipine-10,11-epoxide	CYP3A4
3	Keshari_Wilson_2011	[1-13C]-Dehydroascorbate	Dehydroascorbate	Ascorbate	GSTO1; GSTO2; PAM; DBH
4	Keshari_Wilson_2011	[1-13C]-Ascorbate	Dehydroascorbate	Ascorbate	GSTO1; GSTO2; PAM; DBH
5	Park_Spielman_2017	[1-13C]-Alanine	Pyruvate	Alanine	GPT; GPT2; AGXT; AGXT2
6	Park_Spielman_2017	[1-13C]-Alanine	Pyruvate	Lactate	LDHA; LDHB; LDHC; LDHD; LDHAL6A; LDHAL6B
7	Park_Spielman_2017	[1-13C]-Alanine	Pyruvate	CO2; Acetyl-CoA	PDHA1; PDHB; PDHA2; TYW1; TYW1B; PDHX; DLAT; DLD
8	Park_Spielman_2017	[1-13C]-Alanine	CO2	Bicarbonate	CA1; CA2; CA3; CA4; CA5A; CA5B; CA6; CA7; CA9; CA12; CA13; CA14
9	Dzien_Brindle_2015	[1-13C, U-2H5] Ethanol	Ethanol	Acetate	ALDH2; ALDH1B1; ALDH3B1; ALDH3B2; ADH5; ADH7; ADH1B; ADH1A; ADH1C; ADH4; ADH6
10	Golman_ArdenkjaerLarsen_2006	[1-13C]-Pyruvate	Pyruvate	Lactate	LDHA; LDHB; LDHC; LDHD; LDHAL6A; LDHAL6B
11	Golman_ArdenkjaerLarsen_2006	[1-13C]-Pyruvate	Pyruvate	Alanine	GPT; GPT2; AGXT; AGXT2
12	Hu_Vigneron_2011	[1-13C]-Pyruvate	Pyruvate	CO2; Acetyl-CoA	PDHA1; PDHB; PDHA2; TYW1; TYW1B; PDHX; DLAT; DLD
13	Hu_Vigneron_2011	[1-13C]-Pyruvate	CO2	Bicarbonate	CA1; CA2; CA3; CA4; CA5A; CA5B; CA6; CA7; CA9; CA12; CA13; CA14
14	Merritt_Burgess_2011	[1-13C]-Pyruvate	Pyruvate	Oxaloacetate	ME1; ME2; ME3; FAHD1; PC
15	Merritt_Burgess_2011	[1-13C]-Pyruvate	Pyruvate	Malate	ME1; ME2; ME3
16	Merritt_Burgess_2011	[1-13C]-Pyruvate	Pyruvate	Oxaloacetate	ME1; ME2; ME3; FAHD1; PC
17	Merritt_Burgess_2011	[1-13C]-Pyruvate	Fumarate	Malate	FH
18	Merritt_Burgess_2011	[1-13C]-Pyruvate	Malate	Oxaloacetate	MDH1; MDH2 PHGDH; MDH1B
19	Merritt_Burgess_2011	[1-13C]-Pyruvate	Oxaloacetate	Aspartate	GOT1; GOT2; DDO; GOT1L1; ASPDH
20	Merritt_Burgess_2011	[1-13C]-Pyruvate	Oxaloacetate	PEP; Bicarbonate	PCK1; PCK2
21	Merritt_Burgess_2011	[1-13C]-Pyruvate	Oxaloacetate; Acetyl-CoA	Citrate	ACLY; CS
22	Merritt_Burgess_2011	[1-13C]-Pyruvate	Citrate	CO2; alpha-KG	IDH3A; IDH3B; IDH3G; ACO1; ACO2; IDH1; IDH2
23	Merritt_Burgess_2011	[1-13C]-Pyruvate	alpha-KG	CO2; Succinate	FTO; ALKBH1; ALKBH3; ALKBH5; TMLHE; PHYH; PHF8
24	Merritt_Burgess_2011	[1-13C]-Pyruvate	Succinate	CO2; Fumarate	SDHA; SDHB; ASL
25	Koellisch_StokildeJorgensen_2015	[1-13C]-Acetate	Acetate	Acetyl-CoA	ACSS1; ACSS2; ACOT12; ACSS3
26	Koellisch_StokildeJorgensen_2015	[1-13C]-Acetate	Acetyl-CoA	Acetylcarnitine	CRAT; CPT1A; CPT1B; CPT1C; CPT2
27	Koellisch_StokildeJorgensen_2015	[1-13C]-Acetate	Oxaloacetate; Acetyl-CoA	Citrate	ACLY; CS
28	Koellisch_StokildeJorgensen_2015	[1-13C]-Acetate	Carnitine	Acetylcarnitine	CRAT

29	Jensen_Lerche_2009	[1-13C]-Propionate	Propionate	Propionyl-CoA	SIRT1; ACSS1; ACSS2
30	Jensen_Lerche_2009	[1-13C]-Propionate	Propionyl-CoA	Propionyl-carnitine	CRAT; CPT1A; CPT1B; CPT1C; CPT2
31	Gallagher_Brindle_2009	[1,4-13C2]-Fumarate	Fumarate	Malate	FH
32	SalamancaCardona_Keshari_2017	[1-13C]-Glutamine	Glutamine	Glutamate	GLUL; ASNS; GFPT1; GMPS; NADSYN1; GLS; GLS2; GFPT2; CAD; PPAT; CTPS1; PFAS; GATB; QRSL1; CTPS2; GATC
33	SalamancaCardona_Keshari_2017	[1-13C]-Glutamine	Glutamate	alpha-KG	GLUD1; GLUD2; ABAT; GPT; GPT2; GOT2; GOT1; TAT; AADAT; PSAT1; BCAT1; BCAT2; KYAT3; GOT1L1; KYAT1
34	Gallagher_Brindle_2008	[5-13C]-Glutamine	Glutamine	Glutamate	GLUL; ASNS; GFPT1; GMPS; NADSYN1; GLS; GLS2; GFPT2; CAD; PPAT; CTPS1; PFAS; GATB; QRSL1; CTPS2; GATC
35	Keshari_Kurhanewicz_2009	[2-13C]-Fructose	Fructose	Fructofuranose-6-phosphate	HK1; HK2; HK3
36	Ball_Tyler_2013	[1-13C]-Butyrate	beta-Hydroxybutryryl-CoA	Acetoacetyl-CoA	HADH; EHHADH; HSD17B10; HSD17B12; HADHA; HSD17B4; HADHB
37	Ball_Tyler_2013	[1-13C]-Butyrate	Acetoacetyl-CoA	Acetyl-CoA	ACAT1; ACAT2
38	Ball_Tyler_2013	[1-13C]-Butyrate	Acetoacetyl-CoA	Acetoacetate	OXCT1; AACS; OXCT2
39	Ball_Tyler_2013	[1-13C]-Butyrate	Acetoacetate	beta-Hydroxybutryate	BDH1; HMGCL; BDH2
40	Ball_Tyler_2013	[1-13C]-Butyrate	Acetyl-CoA	Acetylcarnitine	CRAT; CPT1A; CPT1B; CPT1C; CPT2
41	Ball_Tyler_2013	[1-13C]-Butyrate	Oxaloacetate; Acetyl-CoA	Citrate	ACLY; CS
42	Ball_Tyler_2013	[1-13C]-Butyrate	Citrate	CO2; alpha-KG	IDH3A; IDH3B; IDH3G; ACO1; ACO2; IDH1; IDH2
43	Ball_Tyler_2013	[1-13C]-Butyrate	Glutamate	alpha-KG	GLUD1; GLUD2; ABAT; GPT; GPT2; GOT2; GOT1; TAT; AADAT; PSAT1; BCAT1; BCAT2; KYAT3; GOT1L1; KYAT1
44	Hu_Vigneron_2012	[2-13C]-Pyruvate	Pyruvate	Lactate	LDHA; LDHB; LDHC; LDHD; LDHAL6A; LDHAL6B
45	Hu_Vigneron_2012	[2-13C]-Pyruvate	Pyruvate	CO2; Acetyl-CoA	PDHA1; PDHB; PDHA2; TYW1; TYW1B; PDHX; DLAT; DLD
46	Hu_Vigneron_2012	[2-13C]-Pyruvate	Acetyl-CoA	Acetylcarnitine	CRAT; CPT1A; CPT1B; CPT1C; CPT2
47	Hu_Vigneron_2012	[2-13C]-Pyruvate	Oxaloacetate; Acetyl-CoA	Citrate	ACLY; CS
48	Hu_Vigneron_2012	[2-13C]-Pyruvate	Citrate	CO2; alpha-KG	IDH3A; IDH3B; IDH3G; ACO1; ACO2; IDH1; IDH2
49	Hu_Vigneron_2012	[2-13C]-Pyruvate	Glutamate	alpha-KG	GLUD1; GLUD2; ABAT; GPT; GPT2; GOT2; GOT1; TAT; AADAT; PSAT1; BCAT1; BCAT2; KYAT3; GOT1L1; KYAT1

50	Hu_Vigneron_2012	[2-13C]-Pyruvate	Acetoacetyl-CoA	Acetyl-CoA	ACAT1; ACAT2
51	Hu_Vigneron_2012	[2-13C]-Pyruvate	Acetoacetyl-CoA	Acetoacetate	OXCT1; AACS; OXCT2
52	Merritt_Burgess_2011	[1-13C]-Pyruvate	PEP	Pyruvate	PKLR; PKM
53	Moreno_Merritt_2014	[2-13C]-Dihydroxyacetone	Glucose	G6P	GCK; HK1; HK2; HK3; ADPGK; G6PC3; G6PC; SLC37A4; G6PC2
54	Moreno_Merritt_2014	[2-13C]-Dihydroxyacetone	G6P	F6P	GPI
55	Moreno_Merritt_2014	[2-13C]-Dihydroxyacetone	3PG	2PG	PGAM2; PGAM1; PGAM5; BPGM; PGAM4
56	Moreno_Merritt_2014	[2-13C]-Dihydroxyacetone	2PG	PEP	ENO1; ENO2; ENO3; ENO4
57	Moreno_Merritt_2014	[2-13C]-Dihydroxyacetone	13BPG	3PG	PGK1; PGK2
58	Moreno_Merritt_2014	[2-13C]-Dihydroxyacetone	F6P	F16BP	PFKL; PFKM; PFKP; PFKFB2; PFKFB1; PFKFB3; PFKFB4; FBP1; FBP2; TIGAR
59	Moreno_Merritt_2014	[2-13C]-Dihydroxyacetone	DHAP	GA3P	TPI1
60	Moreno_Merritt_2014	[2-13C]-Dihydroxyacetone	DHAP	G3P	GPD1; GPD2
61	Moreno_Merritt_2014	[2-13C]-Dihydroxyacetone	G3P	Glycerol	PGP; GK
62	Moreno_Merritt_2014	[2-13C]-Dihydroxyacetone	GA3P	13BPG	GAPDH
63	Moreno_Merritt_2014	[2-13C]-Dihydroxyacetone	F16BP	GA3P	ALDOA; ALDOB; ALDOC
64	Karlsson_Lerche_2010	[13C]-Ketoisocaproate	KIC	Leucine	BCAT1; BCAT2
65	AllloucheArnon_KatzBrull_2010	CMP2-CholineAnalog	Choline	Acetylcholine	CHAT; BCHE
66	AllloucheArnon_KatzBrull_2013	CMP2-CholineAnalog	Choline	Betaine aldehydyde hydrate	CHDH
67	AllloucheArnon_KatzBrull_2013	CMP2-CholineAnalog	Betaine aldehydyde hydrate	Betaine	ALDH7A1; CHDH
68	Yoshihara_Schwitter_2015	[1-13C]-Octanoate	Octanoate	Acetyl-CoA	ACOT8; ACAA2
69	Yoshihara_Schwitter_2015	[1-13C]-Octanoate	Acetyl-CoA	Acetylcarnitine	CRAT; CPT1A; CPT1B; CPT1C; CPT2
70	Hata_Sando_2015	[1-13C]-Ala-NH2	Ala-NH2	Ala-NH2-APN	ANPEP
71	Najac_Ronen_2016	[1-13C]-Arginine	Arginine	Urea	ARG1; ARG2
72	Karlsson_Lerche_2012	[1,3-13C]-3-hydroxybutryate	Acetoacetate	beta-Hydroxybutryate	BDH1; HMGCL; BDH2
73	Chaumeil_Ronen_2013	[1-13C]-alpha-KG	alpha-KG	2-HG	IDH1; IDH2
74	Rodrigues_Brindle_2014	[U-2H, U-13C]-Glucose	Glucose	G6P	GCK; HK1; HK2; HK3; ADPGK; G6PC3; G6PC; SLC37A4; G6PC2
75	Rodrigues_Brindle_2014	[U-2H, U-13C]-Glucose	G6P	F6P	GPI
76	Rodrigues_Brindle_2014	[U-2H, U-13C]-Glucose	F6P	F16BP	PFKL; PFKM; PFKP; PFKFB2; PFKFB1; PFKFB3; PFKFB4; FBP1; FBP2; TIGAR
77	Rodrigues_Brindle_2014	[U-2H, U-13C]-Glucose	F16BP	GA3P	ALDOA; ALDOB; ALDOC
78	Rodrigues_Brindle_2014	[U-2H, U-13C]-Glucose	DHAP	GA3P	TPI1
79	Rodrigues_Brindle_2014	[U-2H, U-13C]-Glucose	GA3P	13BPG	GAPDH
80	Rodrigues_Brindle_2014	[U-2H, U-13C]-Glucose	13BPG	3PG	PGK1; PGK2
81	Rodrigues_Brindle_2014	[U-2H, U-13C]-Glucose	3PG	2PG	PGAM2; PGAM1; PGAM5; BPGM; PGAM4
82	Rodrigues_Brindle_2014	[U-2H, U-13C]-Glucose	2PG	PEP	ENO1; ENO2; ENO3; ENO4
83	Rodrigues_Brindle_2014	[U-2H, U-13C]-Glucose	PEP	Pyruvate	PKLR; PKM
84	Rodrigues_Brindle_2014	[U-2H, U-13C]-Glucose	Pyruvate	CO2; Acetyl-CoA	PDHA1; PDHB; PDHA2; TYW1; TYW1B; PDHX; DLAT; DLD

85	Rodrigues_Brindle_2014	[U-2H, U-13C]-Glucose	CO2	Bicarbonate	CA1; CA2; CA3; CA4; CA5A; CA5B; CA6; CA7; CA9; CA12; CA13; CA14
86	Rodrigues_Brindle_2014	[U-2H, U-13C]-Glucose	G6P	6PG	G6PD
87	Chaumeil_Ronen_2014	[1-13C]-Glutamate	Glutamine	Glutamate	GLUL; ASNS; GFPT1; GMPS; NADSYN1; GLS; GLS2; GFPT2; CAD; PPAT; CTPS1; PFAS; GATB; QRSL1; CTPS2; GATC
88	Gallagher_Brindle_2011	[1-13C]-Glutamate	Glutamate	alpha-KG	GLUD1; GLUD2; ABAT; GPT; GPT2; GOT2; GOT1; TAT; AADAT; PSAT1; BCAT1; BCAT2; KYAT3; GOT1L1; KYAT1
89	Chen_Vigneron_2008	[1-13C]-Lactate	Pyruvate	Lactate	LDHA; LDHB; LDHC; LDHD; LDHAL6A; LDHAL6B
90	Chen_Vigneron_2008	[1-13C]-Lactate	Pyruvate	Alanine	GPT; GPT2; AGXT; AGXT2
91	Chen_Vigneron_2008	[1-13C]-Lactate	Pyruvate	CO2; Acetyl-CoA	PDHA1; PDHB; PDHA2; TYW1; TYW1B; PDHX; DLAT; DLD
92	Chen_Vigneron_2008	[1-13C]-Lactate	CO2	Bicarbonate	CA1; CA2; CA3; CA4; CA5A; CA5B; CA6; CA7; CA9; CA12; CA13; CA14
93	Park_Billingsley_2017	[1-13C]-Glycerate	DHAP	GA3P	TPI1
94	Park_Billingsley_2017	[1-13C]-Glycerate	DHAP	G3P	GPD1; GPD2
95	Park_Billingsley_2017	[1-13C]-Glycerate	G3P	Glycerol	PGP; GK
96	Park_Billingsley_2017	[1-13C]-Glycerate	13BPG	3PG	PGK1; PGK2
97	Park_Billingsley_2017	[1-13C]-Glycerate	3PG	2PG	PGAM2; PGAM1; PGAM5; BPGM; PGAM4
98	Park_Billingsley_2017	[1-13C]-Glycerate	2PG	PEP	ENO1; ENO2; ENO3; ENO4
99	Park_Billingsley_2017	[1-13C]-Glycerate	PEP	Pyruvate	PKLR; PKM
100	Park_Billingsley_2017	[1-13C]-Glycerate	Pyruvate	CO2; Acetyl-CoA	PDHA1; PDHB; PDHA2; TYW1; TYW1B; PDHX; DLAT; DLD
101	Park_Billingsley_2017	[1-13C]-Glycerate	CO2	Bicarbonate	CA1; CA2; CA3; CA4; CA5A; CA5B; CA6; CA7; CA9; CA12; CA13; CA14

Table 4.S2: DNP probes used to measure metabolic flux.
Each entry in this table consists of a distinct pair of parent and child metabolites, interconverted by the listed enzyme in a manner that has previously been measured (either directly or indirectly) by the DNP agent listed.

	Protein	DNP Probe(s)
1	AACS	[1-13C]-Butyrate, [2-13C]-Pyruvate
2	AADAT	[1-13C]-Butyrate, [1-13C]-Glutamate, [1-13C]-Glutamine, [2-13C]-Pyruvate
3	ABAT	[1-13C]-Butyrate, [1-13C]-Glutamate, [1-13C]-Glutamine, [2-13C]-Pyruvate
4	ACAA2	[1-13C]-Octanoate
5	ACAT1	[1-13C]-Butyrate, [2-13C]-Pyruvate
6	ACAT2	[1-13C]-Butyrate, [2-13C]-Pyruvate
7	ACLY	[1-13C]-Acetate, [1-13C]-Butyrate, [1-13C]-Pyruvate, [2-13C]-Pyruvate
8	ACO1	[1-13C]-Butyrate, [1-13C]-Pyruvate, [2-13C]-Pyruvate
9	ACO2	[1-13C]-Butyrate, [1-13C]-Pyruvate, [2-13C]-Pyruvate
10	ACOT12	[1-13C]-Acetate
11	ACOT8	[1-13C]-Octanoate
12	ACSS1	[1-13C]-Acetate, [1-13C]-Propionate
13	ACSS2	[1-13C]-Acetate, [1-13C]-Propionate
14	ACSS3	[1-13C]-Acetate
15	ACY1	[1-13C]-N-acetyl-L-methionine
16	ADH1A	[1-13C, U-2H5] Ethanol
17	ADH1B	[1-13C, U-2H5] Ethanol
18	ADH1C	[1-13C, U-2H5] Ethanol
19	ADH4	[1-13C, U-2H5] Ethanol
20	ADH5	[1-13C, U-2H5] Ethanol
21	ADH6	[1-13C, U-2H5] Ethanol
22	ADH7	[1-13C, U-2H5] Ethanol
23	ADPGK	[2-13C]-Dihydroxyacetone, [U-2H, U-13C]-Glucose
24	AGXT	[1-13C]-Alanine, [1-13C]-Lactate, [1-13C]-Pyruvate
25	AGXT2	[1-13C]-Alanine, [1-13C]-Lactate, [1-13C]-Pyruvate
26	ALDH1B1	[1-13C, U-2H5] Ethanol
27	ALDH2	[1-13C, U-2H5] Ethanol
28	ALDH3B1	[1-13C, U-2H5] Ethanol
29	ALDH3B2	[1-13C, U-2H5] Ethanol
30	ALDH7A1	CMP2-CholineAnalog
31	ALDOA	[2-13C]-Dihydroxyacetone, [U-2H, U-13C]-Glucose
32	ALDOB	[2-13C]-Dihydroxyacetone, [U-2H, U-13C]-Glucose
33	ALDOC	[2-13C]-Dihydroxyacetone, [U-2H, U-13C]-Glucose
34	ALKBH1	[1-13C]-Pyruvate
35	ALKBH3	[1-13C]-Pyruvate
36	ALKBH5	[1-13C]-Pyruvate
37	ANPEP	[1-13C]-Ala-NH2
38	ARG1	[1-13C]-Arginine
39	ARG2	[1-13C]-Arginine
40	ASL	[1-13C]-Pyruvate
41	ASNS	[1-13C]-Glutamate, [1-13C]-Glutamine, [5-13C]-Glutamine
42	ASPDH	[1-13C]-Pyruvate
43	BCAT1	[1-13C]-Butyrate, [1-13C]-Glutamate, [1-13C]-Glutamine, [13C]-Ketoisocaproate, [2-13C]-Pyruvate
44	BCAT2	[1-13C]-Butyrate, [1-13C]-Glutamate, [1-13C]-Glutamine, [13C]-Ketoisocaproate, [2-13C]-Pyruvate
45	BCHE	CMP2-CholineAnalog
46	BDH1	[1-13C]-Butyrate, [1,3-13C]-3-hydroxybutryate
47	BDH2	[1-13C]-Butyrate, [1,3-13C]-3-hydroxybutryate
48	BPGM	[1-13C]-Glycerate, [2-13C]-Dihydroxyacetone, [U-2H, U-13C]-Glucose
49	CA1	[1-13C]-Alanine, [1-13C]-Glycerate, [1-13C]-Lactate, [1-13C]-Pyruvate, [U-2H, U-13C]-Glucose
50	CA12	[1-13C]-Alanine, [1-13C]-Glycerate, [1-13C]-Lactate, [1-13C]-Pyruvate, [U-2H, U-13C]-Glucose
51	CA13	[1-13C]-Alanine, [1-13C]-Glycerate, [1-13C]-Lactate, [1-13C]-Pyruvate, [U-2H, U-13C]-Glucose
52	CA14	[1-13C]-Alanine, [1-13C]-Glycerate, [1-13C]-Lactate, [1-13C]-Pyruvate, [U-2H, U-13C]-Glucose
53	CA2	[1-13C]-Alanine, [1-13C]-Glycerate, [1-13C]-Lactate, [1-13C]-Pyruvate, [U-2H, U-13C]-Glucose

54	CA3	[1-13C]-Alanine, [1-13C]-Glycerate, [1-13C]-Lactate, [1-13C]-Pyruvate, [U-2H, U-13C]-Glucose
55	CA4	[1-13C]-Alanine, [1-13C]-Glycerate, [1-13C]-Lactate, [1-13C]-Pyruvate, [U-2H, U-13C]-Glucose
56	CA5A	[1-13C]-Alanine, [1-13C]-Glycerate, [1-13C]-Lactate, [1-13C]-Pyruvate, [U-2H, U-13C]-Glucose
57	CA5B	[1-13C]-Alanine, [1-13C]-Glycerate, [1-13C]-Lactate, [1-13C]-Pyruvate, [U-2H, U-13C]-Glucose
58	CA6	[1-13C]-Alanine, [1-13C]-Glycerate, [1-13C]-Lactate, [1-13C]-Pyruvate, [U-2H, U-13C]-Glucose
59	CA7	[1-13C]-Alanine, [1-13C]-Glycerate, [1-13C]-Lactate, [1-13C]-Pyruvate, [U-2H, U-13C]-Glucose
60	CA9	[1-13C]-Alanine, [1-13C]-Glycerate, [1-13C]-Lactate, [1-13C]-Pyruvate, [U-2H, U-13C]-Glucose
61	CAD	[1-13C]-Glutamate, [1-13C]-Glutamine, [5-13C]-Glutamine
62	CHAT	CMP2-CholineAnalog
63	CHDH	CMP2-CholineAnalog
64	CPT1A	[1-13C]-Acetate, [1-13C]-Butyrate, [1-13C]-Octanoate, [1-13C]-Propionate, [2-13C]-Pyruvate
65	CPT1B	[1-13C]-Acetate, [1-13C]-Butyrate, [1-13C]-Octanoate, [1-13C]-Propionate, [2-13C]-Pyruvate
66	CPT1C	[1-13C]-Acetate, [1-13C]-Butyrate, [1-13C]-Octanoate, [1-13C]-Propionate, [2-13C]-Pyruvate
67	CPT2	[1-13C]-Acetate, [1-13C]-Butyrate, [1-13C]-Octanoate, [1-13C]-Propionate, [2-13C]-Pyruvate
68	CRAT	[1-13C]-Acetate, [1-13C]-Butyrate, [1-13C]-Octanoate, [1-13C]-Propionate, [2-13C]-Pyruvate
69	CS	[1-13C]-Acetate, [1-13C]-Butyrate, [1-13C]-Pyruvate, [2-13C]-Pyruvate
70	CTPS1	[1-13C]-Glutamate, [1-13C]-Glutamine, [5-13C]-Glutamine
71	CTPS2	[1-13C]-Glutamate, [1-13C]-Glutamine, [5-13C]-Glutamine
72	CYP3A4	13C-Carbamazepine
73	DBH	[1-13C]-Ascorbate, [1-13C]-Dehydroascorbate
74	DDO	[1-13C]-Pyruvate
75	DLAT	[1-13C]-Alanine, [1-13C]-Glycerate, [1-13C]-Lactate, [1-13C]-Pyruvate, [2-13C]-Pyruvate, [U-2H, U-13C]-Glucose
76	DLD	[1-13C]-Alanine, [1-13C]-Glycerate, [1-13C]-Lactate, [1-13C]-Pyruvate, [2-13C]-Pyruvate, [U-2H, U-13C]-Glucose
77	EHHADH	[1-13C]-Butyrate
78	ENO1	[1-13C]-Glycerate, [2-13C]-Dihydroxyacetone, [U-2H, U-13C]-Glucose
79	ENO2	[1-13C]-Glycerate, [2-13C]-Dihydroxyacetone, [U-2H, U-13C]-Glucose
80	ENO3	[1-13C]-Glycerate, [2-13C]-Dihydroxyacetone, [U-2H, U-13C]-Glucose
81	ENO4	[1-13C]-Glycerate, [2-13C]-Dihydroxyacetone, [U-2H, U-13C]-Glucose
82	FAHD1	[1-13C]-Pyruvate
83	FBP1	[2-13C]-Dihydroxyacetone, [U-2H, U-13C]-Glucose
84	FBP2	[2-13C]-Dihydroxyacetone, [U-2H, U-13C]-Glucose
85	FH	[1-13C]-Pyruvate, [1,4-13C2]-Fumarate
86	FTO	[1-13C]-Pyruvate
87	G6PC	[2-13C]-Dihydroxyacetone, [U-2H, U-13C]-Glucose
88	G6PC2	[2-13C]-Dihydroxyacetone, [U-2H, U-13C]-Glucose
89	G6PC3	[2-13C]-Dihydroxyacetone, [U-2H, U-13C]-Glucose
90	G6PD	[U-2H, U-13C]-Glucose
91	GAPDH	[2-13C]-Dihydroxyacetone, [U-2H, U-13C]-Glucose
92	GATB	[1-13C]-Glutamate, [1-13C]-Glutamine, [5-13C]-Glutamine
93	GATC	[1-13C]-Glutamate, [1-13C]-Glutamine, [5-13C]-Glutamine
94	GCK	[2-13C]-Dihydroxyacetone, [U-2H, U-13C]-Glucose
95	GFPT1	[1-13C]-Glutamate, [1-13C]-Glutamine, [5-13C]-Glutamine
96	GFPT2	[1-13C]-Glutamate, [1-13C]-Glutamine, [5-13C]-Glutamine
97	GK	[1-13C]-Glycerate, [2-13C]-Dihydroxyacetone
98	GLS	[1-13C]-Glutamate, [1-13C]-Glutamine, [5-13C]-Glutamine
99	GLS2	[1-13C]-Glutamate, [1-13C]-Glutamine, [5-13C]-Glutamine
100	GLUD1	[1-13C]-Butyrate, [1-13C]-Glutamate, [1-13C]-Glutamine, [2-13C]-Pyruvate
101	GLUD2	[1-13C]-Butyrate, [1-13C]-Glutamate, [1-13C]-Glutamine, [2-13C]-Pyruvate
102	GLUL	[1-13C]-Glutamate, [1-13C]-Glutamine, [5-13C]-Glutamine
103	GMPS	[1-13C]-Glutamate, [1-13C]-Glutamine, [5-13C]-Glutamine
104	GOT1	[1-13C]-Butyrate, [1-13C]-Glutamate, [1-13C]-Glutamine, [1-13C]-Pyruvate, [2-13C]-Pyruvate
105	GOT1L1	[1-13C]-Butyrate, [1-13C]-Glutamate, [1-13C]-Glutamine, [1-13C]-Pyruvate, [2-13C]-Pyruvate
106	GOT2	[1-13C]-Butyrate, [1-13C]-Glutamate, [1-13C]-Glutamine, [1-13C]-Pyruvate, [2-13C]-Pyruvate
107	GPD1	[1-13C]-Glycerate, [2-13C]-Dihydroxyacetone

108	GPD2	[1-13C]-Glycerate, [2-13C]-Dihydroxyacetone
109	GPI	[2-13C]-Dihydroxyacetone, [U-2H, U-13C]-Glucose
110	GPT	[1-13C]-Alanine, [1-13C]-Butyrate, [1-13C]-Glutamate, [1-13C]-Glutamine, [1-13C]-Lactate, [1-13C]-Pyruvate, [2-13C]-Pyruvate
111	GPT2	[1-13C]-Alanine, [1-13C]-Butyrate, [1-13C]-Glutamate, [1-13C]-Glutamine, [1-13C]-Lactate, [1-13C]-Pyruvate, [2-13C]-Pyruvate
112	GSTO1	[1-13C]-Ascorbate, [1-13C]-Dehydroascorbate
113	GSTO2	[1-13C]-Ascorbate, [1-13C]-Dehydroascorbate
114	HADH	[1-13C]-Butyrate
115	HADHA	[1-13C]-Butyrate
116	HADHB	[1-13C]-Butyrate
117	HK1	[2-13C]-Dihydroxyacetone, [2-13C]-Fructose, [U-2H, U-13C]-Glucose
118	HK2	[2-13C]-Dihydroxyacetone, [2-13C]-Fructose, [U-2H, U-13C]-Glucose
119	HK3	[2-13C]-Dihydroxyacetone, [2-13C]-Fructose, [U-2H, U-13C]-Glucose
120	HMGCL	[1-13C]-Butyrate, [1,3-13C]-3-hydroxybutryate
121	HSD17B10	[1-13C]-Butyrate
122	HSD17B12	[1-13C]-Butyrate
123	HSD17B4	[1-13C]-Butyrate
124	IDH1	[1-13C]-alpha-KG, [1-13C]-Butyrate, [1-13C]-Pyruvate, [2-13C]-Pyruvate
125	IDH2	[1-13C]-alpha-KG, [1-13C]-Butyrate, [1-13C]-Pyruvate, [2-13C]-Pyruvate
126	IDH3A	[1-13C]-Butyrate, [1-13C]-Pyruvate, [2-13C]-Pyruvate
127	IDH3B	[1-13C]-Butyrate, [1-13C]-Pyruvate, [2-13C]-Pyruvate
128	IDH3G	[1-13C]-Butyrate, [1-13C]-Pyruvate, [2-13C]-Pyruvate
129	KYAT1	[1-13C]-Butyrate, [1-13C]-Glutamate, [1-13C]-Glutamine, [2-13C]-Pyruvate
130	KYAT3	[1-13C]-Butyrate, [1-13C]-Glutamate, [1-13C]-Glutamine, [2-13C]-Pyruvate
131	LDHA	[1-13C]-Alanine, [1-13C]-Lactate, [1-13C]-Pyruvate, [2-13C]-Pyruvate
132	LDHAL6A	[1-13C]-Alanine, [1-13C]-Lactate, [1-13C]-Pyruvate, [2-13C]-Pyruvate
133	LDHAL6B	[1-13C]-Alanine, [1-13C]-Lactate, [1-13C]-Pyruvate, [2-13C]-Pyruvate
134	LDHB	[1-13C]-Alanine, [1-13C]-Lactate, [1-13C]-Pyruvate, [2-13C]-Pyruvate
135	LDHC	[1-13C]-Alanine, [1-13C]-Lactate, [1-13C]-Pyruvate, [2-13C]-Pyruvate
136	LDHD	[1-13C]-Alanine, [1-13C]-Lactate, [1-13C]-Pyruvate, [2-13C]-Pyruvate
137	MDH1	[1-13C]-Pyruvate
138	MDH1B	[1-13C]-Pyruvate
139	MDH2PHGDH	[1-13C]-Pyruvate
140	ME1	[1-13C]-Pyruvate
141	ME2	[1-13C]-Pyruvate
142	ME3	[1-13C]-Pyruvate
143	NADSYN1	[1-13C]-Glutamate, [1-13C]-Glutamine, [5-13C]-Glutamine
144	OXCT1	[1-13C]-Butyrate, [2-13C]-Pyruvate
145	OXCT2	[1-13C]-Butyrate, [2-13C]-Pyruvate
146	PAM	[1-13C]-Ascorbate, [1-13C]-Dehydroascorbate
147	PC	[1-13C]-Pyruvate
148	PCK1	[1-13C]-Pyruvate
149	PCK2	[1-13C]-Pyruvate
150	PDHA1	[1-13C]-Alanine, [1-13C]-Glycerate, [1-13C]-Lactate, [1-13C]-Pyruvate, [2-13C]-Pyruvate, [U-2H, U-13C]-Glucose
151	PDHA2	[1-13C]-Alanine, [1-13C]-Glycerate, [1-13C]-Lactate, [1-13C]-Pyruvate, [2-13C]-Pyruvate, [U-2H, U-13C]-Glucose
152	PDHB	[1-13C]-Alanine, [1-13C]-Glycerate, [1-13C]-Lactate, [1-13C]-Pyruvate, [2-13C]-Pyruvate, [U-2H, U-13C]-Glucose
153	PDHX	[1-13C]-Alanine, [1-13C]-Glycerate, [1-13C]-Lactate, [1-13C]-Pyruvate, [2-13C]-Pyruvate, [U-2H, U-13C]-Glucose
154	PFAS	[1-13C]-Glutamate, [1-13C]-Glutamine, [5-13C]-Glutamine
155	PFKFB1	[2-13C]-Dihydroxyacetone, [U-2H, U-13C]-Glucose
156	PFKFB2	[2-13C]-Dihydroxyacetone, [U-2H, U-13C]-Glucose
157	PFKFB3	[2-13C]-Dihydroxyacetone, [U-2H, U-13C]-Glucose
158	PFKFB4	[2-13C]-Dihydroxyacetone, [U-2H, U-13C]-Glucose
159	PFKL	[2-13C]-Dihydroxyacetone, [U-2H, U-13C]-Glucose
160	PFKM	[2-13C]-Dihydroxyacetone, [U-2H, U-13C]-Glucose

161	PFKP	[2-13C]-Dihydroxyacetone, [U-2H, U-13C]-Glucose
162	PGAM1	[1-13C]-Glycerate, [2-13C]-Dihydroxyacetone, [U-2H, U-13C]-Glucose
163	PGAM2	[1-13C]-Glycerate, [2-13C]-Dihydroxyacetone, [U-2H, U-13C]-Glucose
164	PGAM4	[1-13C]-Glycerate, [2-13C]-Dihydroxyacetone, [U-2H, U-13C]-Glucose
165	PGAM5	[1-13C]-Glycerate, [2-13C]-Dihydroxyacetone, [U-2H, U-13C]-Glucose
166	PGK1	[1-13C]-Glycerate, [2-13C]-Dihydroxyacetone, [U-2H, U-13C]-Glucose
167	PGK2	[1-13C]-Glycerate, [2-13C]-Dihydroxyacetone, [U-2H, U-13C]-Glucose
168	PGP	[1-13C]-Glycerate, [2-13C]-Dihydroxyacetone
169	PHF8	[1-13C]-Pyruvate
170	PHYH	[1-13C]-Pyruvate
171	PKLR	[1-13C]-Glycerate, [1-13C]-Pyruvate, [U-2H, U-13C]-Glucose
172	PKM	[1-13C]-Glycerate, [1-13C]-Pyruvate, [U-2H, U-13C]-Glucose
173	PPAT	[1-13C]-Glutamate, [1-13C]-Glutamine, [5-13C]-Glutamine
174	PSAT1	[1-13C]-Butyrate, [1-13C]-Glutamate, [1-13C]-Glutamine, [2-13C]-Pyruvate
175	QRSL1	[1-13C]-Glutamate, [1-13C]-Glutamine, [5-13C]-Glutamine
176	SDHA	[1-13C]-Pyruvate
177	SDHB	[1-13C]-Pyruvate
178	SIRT1	[1-13C]-Propionate
179	SLC37A4	[2-13C]-Dihydroxyacetone, [U-2H, U-13C]-Glucose
180	TAT	[1-13C]-Butyrate, [1-13C]-Glutamate, [1-13C]-Glutamine, [2-13C]-Pyruvate
181	TIGAR	[2-13C]-Dihydroxyacetone, [U-2H, U-13C]-Glucose
182	TMLHE	[1-13C]-Pyruvate
183	TPI1	[1-13C]-Glycerate, [2-13C]-Dihydroxyacetone, [U-2H, U-13C]-Glucose
184	TYW1	[1-13C]-Alanine, [1-13C]-Glycerate, [1-13C]-Lactate, [1-13C]-Pyruvate, [2-13C]-Pyruvate, [U-2H, U-13C]-Glucose
185	TYW1B	[1-13C]-Alanine, [1-13C]-Glycerate, [1-13C]-Lactate, [1-13C]-Pyruvate, [2-13C]-Pyruvate, [U-2H, U-13C]-Glucose

Table 4.S3: Paired list of proteins and affiliated DNP-probes that have been used to measure flux.
This table, organized alphabetically, provides a list of genes, all of which are enzymes, whose flux has been measured by the listed DNP-probe (either directly or indirectly), according to the data provided in Table 4.S2.

4.9: References

1. Santos, R. *et al.* A comprehensive map of molecular drug targets. *Nat. Rev. Drug Discov.* **16**, 19–34 (2017).
2. Mankoff, D. A., Farwell, M. D., Clark, A. S. & Pryma, D. A. Making molecular imaging a clinical tool for precision oncology: A review. *JAMA Oncol.* **3**, 695–701 (2017).
3. El-Serag, H. B. Hepatocellular Carcinoma. *N. Engl. J. Med.* **365**, 1118–1127 (2011).
4. van der Pol, C. B. *et al.* Accuracy of the Liver Imaging Reporting and Data System in Computed Tomography and Magnetic Resonance Image Analysis of Hepatocellular Carcinoma or Overall Malignancy—A Systematic Review. *Gastroenterology* **156**, 976–986 (2019).
5. Shi, J. *et al.* Discovery of cancer drug targets by CRISPR-Cas9 screening of protein domains. *Nat. Biotechnol.* **33**, 661–667 (2015).
6. Keshari, K. R. & Wilson, D. M. Chemistry and biochemistry of 13C hyperpolarized magnetic resonance using dynamic nuclear polarization. *Chem. Soc. Rev.* **43**, (2014).
7. Chaumeil, M. M. *et al.* Non-invasive in vivo assessment of IDH1 mutational status in glioma. *Nat. Commun.* **4**, 1–12 (2013).
8. Witney, T. H., Kettunen, M. I. & Brindle, K. M. Kinetic modeling of hyperpolarized 13C label exchange between pyruvate and lactate in tumor cells. *J. Biol. Chem.* **286**, 24572–24580 (2011).
9. Meyers, R. M. *et al.* Computational correction of copy number effect improves specificity of CRISPR-Cas9 essentiality screens in cancer cells. *Nat. Genet.* **49**, 1779–1784 (2017).
10. Broad Institute. DepMap. (2019).
11. Kudo, M. *et al.* Lenvatinib versus sorafenib in first-line treatment of patients with unresectable hepatocellular carcinoma: a randomised phase 3 non-inferiority trial. *The Lancet* **391**, 1163–1173 (2018).
12. Wildenberg, J., Perkons, N. R., Pilla, G., Kadlecek, S. & Gade, T. P. Computational Pipeline for Estimation of Small-Molecule T1 Relaxation Times [Under Review, Unpublished]. *J. Magn. Reson.* (2020).
13. Düwel, S. *et al.* Multiparametric human hepatocellular carcinoma characterization and therapy response evaluation by hyperpolarized 13C MRSI. *NMR Biomed.* **29**, 952–960 (2016).
14. Perkons, N. R. *et al.* Hyperpolarized Metabolic Imaging Detects Latent Hepatocellular Carcinoma Domains Surviving Locoregional Therapy. *Hepatology* (2019). doi:10.1002/HEP.30970
15. Liberti, M. V. & Locasale, J. W. The Warburg Effect: How Does it Benefit Cancer Cells? *Trends Biochem. Sci.* **41**, 211–218 (2016).
16. Chen, Y. *et al.* Plasma metabolomic analysis of human hepatocellular carcinoma: Diagnostic and therapeutic study. *Oncotarget* **7**, 47332–47342 (2016).
17. Faloppi, L. *et al.* The role of LDH serum levels in predicting global outcome in HCC patients treated with sorafenib: Implications for clinical management. *BMC Cancer* **14**, 1–8 (2014).
18. Granlund, K. L. *et al.* Hyperpolarized MRI of Human Prostate Cancer Reveals Increased Lactate with Tumor Grade Driven by Monocarboxylate Transporter 1. *Cell Metab.* **31**, 105–114 (2020).
19. Zacharias, N. M. *et al.* Assessing metabolic intervention with a glutaminase inhibitor

in real-time by hyperpolarized magnetic resonance in acute myeloid leukemia. *Mol. Cancer Ther.* **18**, 1937–1946 (2019).

20. Rauscher, I., Eiber, M., Souvatzoglou, M., Schwaiger, M. & Beer, A. J. PET/MR in Oncology: Non-18F-FDG tracers for routine applications. *J. Nucl. Med.* **55**, 25S-31S (2014).
21. Ritchie, M. E. *et al.* Limma powers differential expression analyses for RNA-sequencing and microarray studies. *Nucleic Acids Res.* **43**, 1–13 (2015).
22. Chaumeil, M. M., Najac, C. & Ronen, S. M. Studies of Metabolism Using ^{13}C MRS of Hyperpolarized Probes. *Methods Enzymol.* **561**, 1–71 (2015).
23. Uniprot. UniProt : a worldwide hub of protein knowledge. *Nucleic Acids Res.* **47**, 506–515 (2019).
24. Szklarczyk, D. *et al.* The STRING database in 2017: quality-controlled protein–protein association networks, made broadly accessible. *Nucleic Acids Res.* **45**, 362–368 (2017).
25. Cao, Q. *et al.* CRISPR-FOCUS: A web server for designing focused CRISPR screening experiments. *PLoS One* **12**, 1–8 (2017).
26. Chen, S. *et al.* Genome-wide CRISPR screen in a mouse model of tumor growth and metastasis. *Cell* **160**, 1246–1260 (2015).
27. Wang, T., Wei, J., Sabatini, D. & Lander, E. Genetic Screens in Human Cells Using. *Science* **80**, 80–85 (2014).
28. Lin, K. H. *et al.* Systematic Dissection of the Metabolic-Apoptotic Interface in AML Reveals Heme Biosynthesis to Be a Regulator of Drug Sensitivity. *Cell Metab.* **29**, 1217–1231 (2019).
29. Shalem, O., Sanjana, E. N., Hartenian, E. & Zhang, F. Genome-Scale CRISPR-Cas9 Knockout. *Science* **343**, 84–87 (2014).
30. Parnas, O. *et al.* A Genome-wide CRISPR Screen in Primary Immune Cells to Dissect Regulatory Networks. *Cell* **162**, 675–686 (2015).
31. White, E. & DiPaola, R. S. The double-edged sword of autophagy modulation in cancer. *Clin. Cancer Res.* **15**, 5308–5316 (2009).
32. Robinson, M. D., McCarthy, D. . & Smyth, G. K. edgeR: A Bioconductor package for differential expression analysis of digital gene expression data. *Bioinformatics* **26**, 139–140 (2009).
33. Kiefer, R. M. *et al.* Relative Initial Weight Is Associated with Improved Survival without Altering Tumor Latency in a Translational Rat Model of Diethylnitrosamine-Induced Hepatocellular Carcinoma and Transarterial Embolization. *J. Vasc. Interv. Radiol.* **28**, 1043–1050 (2017).
34. Gade, T. P. F. F. *et al.* Segmental Transarterial Embolization in a Translational Rat Model of Hepatocellular Carcinoma. *J. Vasc. Interv. Radiol.* **26**, 1229–1237 (2015).
35. Thièry, J. P. *et al.* Hepatocellular carcinoma cell lines from diethylnitrosamine phenobarbital-treated rats. Characterization and sensitivity to endothall, a protein serine/threonine phosphatase-2A inhibitor. *Hepatology* **29**, 1406–1417 (1999).
36. Yeung, C. *et al.* Targeting Glycolysis through Inhibition of Lactate Dehydrogenase Impairs Tumor Growth in Preclinical Models of Ewing Sarcoma. *Cancer Res.* **79**, 5060–5073 (2019).
37. Rai, G. *et al.* Discovery and Optimization of Potent, Cell-Active Pyrazole-Based Inhibitors of Lactate Dehydrogenase (LDH). *J. Med. Chem.* **60**, 9184–9204 (2017).
38. Basic Practical NMR Concepts : A Guide for the Modern Laboratory. *Max T. Rogers NMR Facility* 1–41 (2013).

Chapter 5: DNP-^{13}C-MRSI Quantification Considerations

5.1: Introduction

The chapter discusses considerations relevant to the quantification of metabolism with DNP-^{13}C-MRSI, including experimental evidence when appropriate. It begins by discussing concerns pertinent to ensuring accurate quantification of spectroscopic images. Several sections of this chapter are adopted from an article by Perkons et al. that was submitted for consideration for publication in *Magnetic Resonance in Medicine* in Spring 2020 and the supplemental information of an article by Perkons et al. in *Hepatology* that was published in 2019 entitled “Hyperpolarized Metabolic Imaging Detects Latent Hepatocellular Carcinoma Domains Surviving Locoregional Therapy”[1]. The principal conclusion of these sections is that DNP-MRSI facilitates real-time *in vivo* metabolism quantification that is repeatable and reflective of intracellular processes noting that interpretation requires careful consideration of probe dose and administration frequency.

5.2: Functional molecular imaging background

Functional molecular imaging enables non-invasive assessment of tissue composition and energy use, promoting distinction of pathology independent of histopathologic approaches. Superimposed upon anatomic images acquired using computed tomography (CT) or magnetic resonance imaging (MRI), functional molecular imaging measures how the administration of a probe—frequently an isotope or analog of a naturally abundant molecule—interacts with a tissue of interest. Radioactivity and hyperpolarization (HP) are among the most frequent techniques to label a probe. In positron emission tomography (PET), the location of a radioactively labeled nucleus—such as ^{18}F or ^{11}C—is measured by back projection of anti-parallel characteristic electromagnetic radiation (at 511 keV) emitted when a positron collides with an electron[2]. In dynamic nuclear polarization (DNP) enhanced magnetic resonance spectroscopy (MRS), the location and biochemical fate of an HP nucleus—such as ^{13}C—is measured on the basis of chemical shift[3]. PET and DNP provide distinct advantages and limitations but share the common goal of functionally characterizing a tissue on the basis of *in situ* probe modification. Compared to PET, DNP is uniquely capable of directly measuring probe metabolism because chemical reactions preserve a nucleus' HP state while altering its chemical shift. The subsequent discussion and experimental evidence outline special considerations for DNP based assessments of metabolism.

5.3: Ensuring accurate quantification of DNP Images

Ensuring that raw spectroscopic signals obtained after reconstruction provide quantitative representations of the underlying data requires special consideration. This is particularly important in cases where longitudinal comparisons or inter-subject comparisons are desired. Several prominent corrections utilized for this work, as discussed in both Chapters 4 and 6, include (i) point spread function correction, (ii) B_1 correction, (iii) polarization efficiency correction, (iv) baseline subtraction, and (v) normalization to a known standard prior to quantification.

Point spread function correction

The point spread function (PSF) describes the distribution of signal detected from a single point source. For imaging applications, such as those described herein, PSF correction rectifies the tendency for signal emanating from one voxel to be detected in nearby voxels[4]. Point spread correction was performed in this work using the Lucy-Richardson deconvolution method with a [1-^{13}C]-Propionate phantom utilized for the acquisition of a reference map (Figure 5.1A, 5.1B, 5.1C). Figure 5.1B provides a schematic of the true distribution of signal corresponding to a point source, whereas figure 5.1C demonstrates the measured signal using the surface coil described herein. Figure 5.1C also represents the input matrix used for Lucy-Richardson deconvolution. Figure 5.1H demonstrates the effect of PSF correction on the raw image in Figure 5.1G. This correction results in a consolidation of non-specific signal to regions of the image corresponding to tumor or blood vessels.

B_1-Correction

As the induced magnetic field, B_1, of a surface coil is not spatially uniform, B_1-correction is necessary to rectify spatial dependence in sensitivity. B_1 correction was performed based upon a map generated from a double angle method (88°, 176°) of an ethylene glycol phantom (Figure 5.1D, 5.1E, 5.1F)[5]. Prior to acquisitions with the phantom, pulse widths and flip angles were calibrated according to the measured flips of a sodium propionate bulb positioned 2 cm from the surface coil (the average distance of a tumor in the liver from the surface coil) in an otherwise equivalent ethylene glycol phantom.

For images that were to be B_1 corrected, the surface coil was calibrated to achieve a 20° excitation at the center of the tumor (or area of interest) on the day of imaging. Spatial dependence of flip angle was calculated using: the generated B_1 map from the ethylene glycol phantom, the location of the tumor relative to a fixed reference located within the surface coil encasement (a glass bulb filled with ^{13}C-Urea), and extent of rotation of the surface coil relative to its position during B_1 mapping. This matrix was used to scale individual EPSI spectra to reflect the signal expected from a 20° excitation. Figure 5.1I demonstrates the effect of B_1 correction on the image in Figure 5.1H for which only PSF correction had been performed. Signals further from the coil are amplified, while those closer to the coil are diminished.

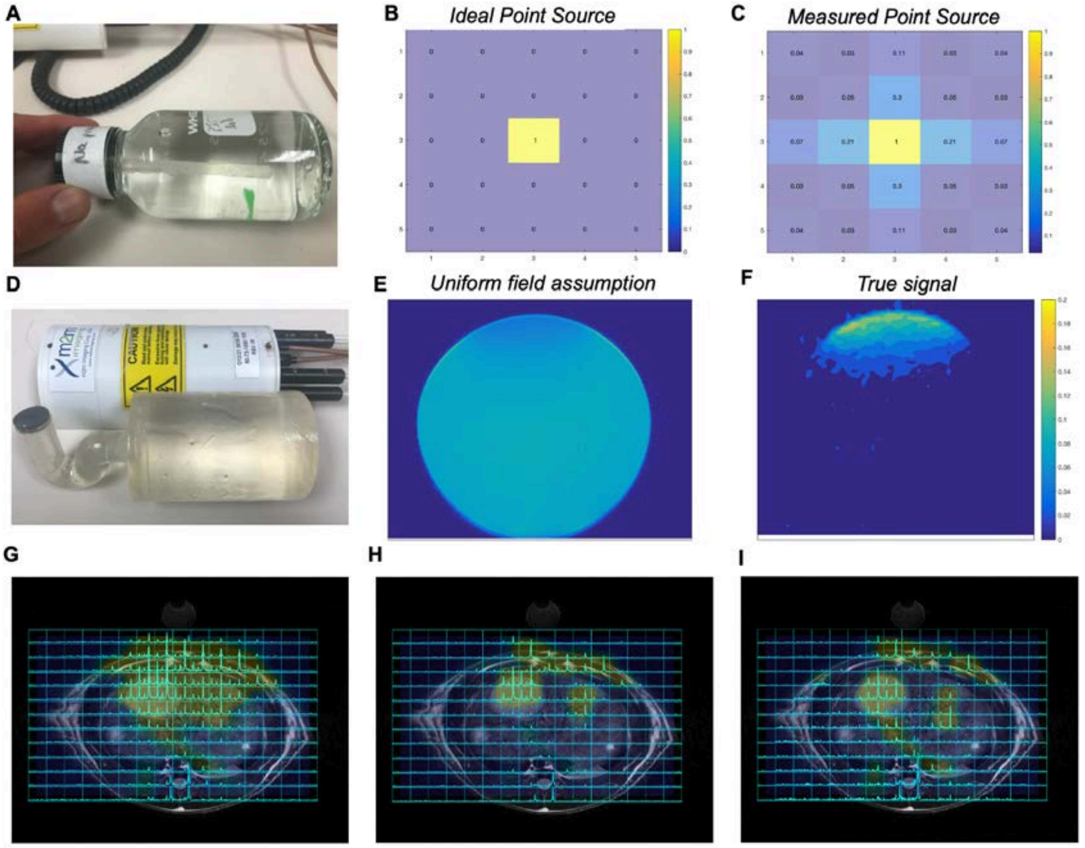

Figure 5.1: B_1 and Point Spread Function Corrections
(A) A phantom containing sodium propionate used for estimation of the point spread function. (B) Stylization of the true signal corresponding to a point source. (C) Stylization of the signal measured from a point source located in a single voxel. (D) A 3D printed phantom filled with ethylene glycol and imaged using the double angle method for estimation of the B1 map for the surface coil located in the background of the image. (E) Stylization of signal anticipated from a uniform B1 field. (F) True signal measured from the phantom in (D) with a 20-degree excitation 2 cm from the center of the coil. (G, H, I) Raw, PSF corrected, and PSF + B1 corrected parametric maps of a rat with liver cancer (tumor located in upper left quadrant of image) with the foreground parametric map indicating signifying the integral of pyruvate signal.

Polarization efficiency correction

Polarization efficiency correction accounts for slight variations in the performance of th hyperpolarizer. The Hypersense pre-clinical hyperpolarizer routinely achieves a polarization efficiency of approximately 30% (representing the percentage of ^{13}C nuclei in a hyperpolarized state). Immediately prior to injection, the efficiency of each polarization was recorded and used for normalization in post-processing to avoid confounding non-ratiometric analyses.

Baseline correction

Baseline correction of spectroscopic data is required to remove any voxel-specific biases in signal that are present across images; to do this, the average signal (magnitude data was used) obtained from each of the tumor voxels in the baseline EPSI scan was subtracted from each subsequent scan of a given study. In the event that signal from tumors or other structures was quantified from interpolated regions of interest rather than the sum of complete voxels, the average signal from the corresponding region in the baseline scan was used for subtraction.

Normalization to a known standard

Normalization to a known standard is required to permit comparison of quantified metabolite resonances between studies. To do this, acquired data was normalized to the signal acquired from a baseline scan performed at each imaging session, capturing a ^{13}C-urea reference present in the surface coil. This ^{13}C-urea standard was also used as a chemical shift reference (δ**:** 165.5**)**.

5.4: Standardizing delivery of the DNP agent

As the hyperpolarized state of a nucleus decays according to its T_1 relaxation time, shortening the time to injection and standardizing the time course of delivery from the polarizer are important considerations for repeatability as well as for optimization of the signal-to-noise ratio. In this work, I implemented a system to standardize delivery utilizing a high-pressure liquid chromatography (HPLC) pump. Hyperpolarized substrate dispensed from the polarizer is deposited in a conical tube connected to the inlet of the pump. Upon delivery of the substrate, the pump is turned on using an Arduino microcontroller and then ramps to a speed of 10 mL/min and pumps the substrate

through low-diameter, high-pressure PEEK tubing (I.D. = 0.01") into the room containing the MRI within ~7 s. Prior to injections, all PEEK tubing was primed with saline. A three-port valve was used to capture the saline contained in the line prior to the arrival of the hyperpolarized substrate by connecting one port to a syringe with a capacity equivalent to the dead volume in the line. Once the syringe is filled, it generates enough resistance to drive flow of the HP substrate through a second port and into the magnet. The Arduino microcontroller automatically turned off the HPLC pump based upon the volume of substrate intended to be delivered. Figure 5.2 provides a schematic and photos of this setup.

5.5: Fidelity of DNP Assessment to Biology: Background

As discussed previously in Chapter 2, DNP is achieved by transferring the spin polarization of an electron source to a nucleus with ≥2 unique energy levels (i.e. $I \neq 0$) through microwave irradiation of an amorphous solid mixture that is maintained at a temperature near absolute 0 within an external magnetic field, facilitated by the Overhauser effect[6,7]. More than 60 DNP-^{13}C probes have been reported in the literature, of which the majority are small metabolites[3]. Such probes are used to quantify *in situ* metabolism based on the spatial and temporal conversion of a probe to its metabolites. DNP-[1-^{13}C]-pyruvate is the most frequently studied probe, whose metabolism to lactate, alanine, and bicarbonate can be readily quantified. Ongoing trials in human prostate

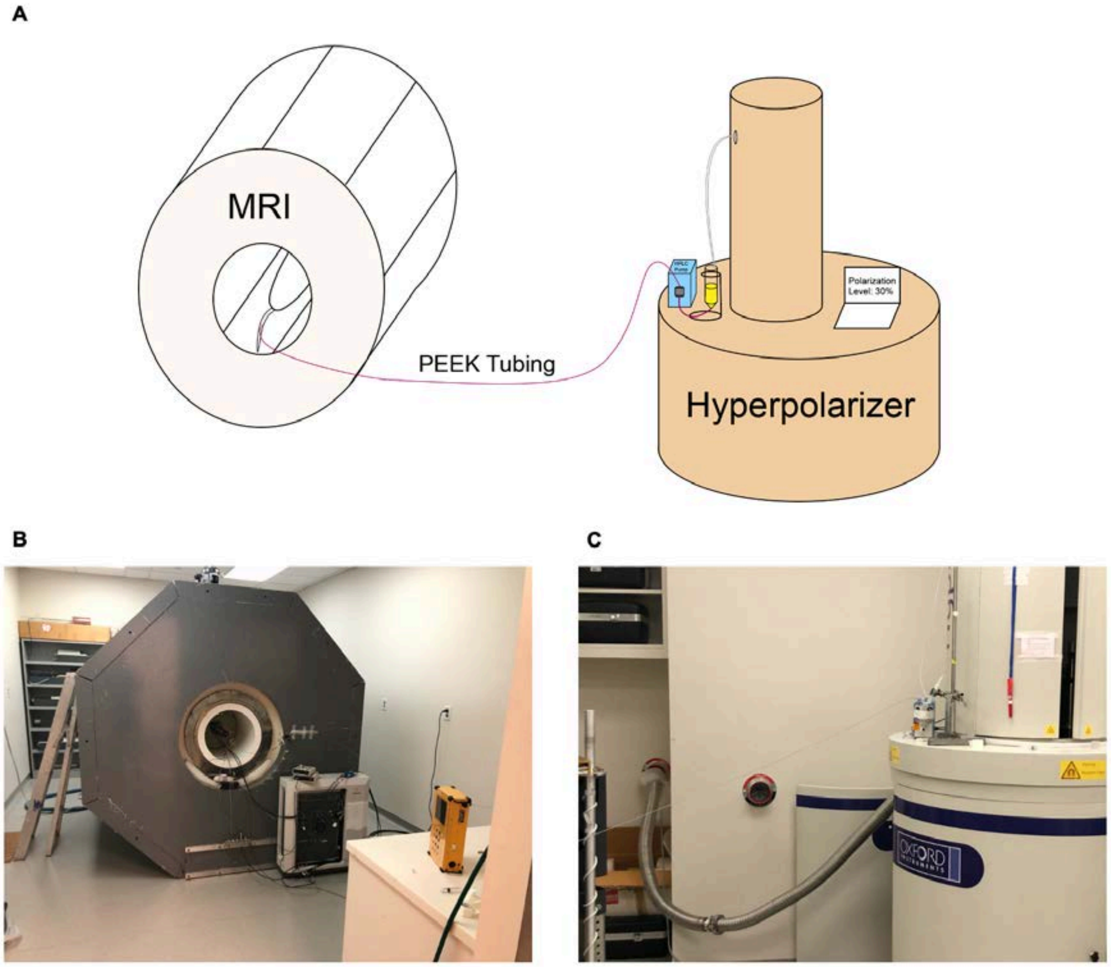

Figure 5.2: System for automated delivery of DNP Substrate
(A) Schematic of the automated injection setup, along with photos of the setup at the magnet (B) and polarizer (C).

cancer[8,9], glioblastoma[10], and breast cancer[11] are specifically measuring local conversion of DNP-[1-^{13}C]-pyruvate to DNP-[1-^{13}C]-lactate. Compared to PET, DNP uses much higher concentrations of metabolites (typically ~30-80 mM) and the signal's half-life is much shorter, as governed by T_1 relaxation. As DNP experiments are frequently used to assess apparent rates of metabolism, the effect of mM concentrations of injected metabolites on measured rates should be considered, particularly for the case of multiple injections in a single session[12]. Prior research has demonstrated that variations in pyruvate dose influence the kinetic parameters describing rates of lactate and alanine formation[13]. Others have shown that transport[14,15] and exogenous metabolite concentrations[16] can affect apparent rates of DNP-quantified metabolism. The subsequently presented experiments leverage an autochthonous rat model of hepatocellular carcinoma (HCC) to characterize the influence of probe concentration, repeat injections, and pharmacologic enzyme modulation on DNP-based measurements of intratumoral metabolism.

5.6: Fidelity of DNP Assessment to Biology: Methods

Rodent model of Hepatocellular Carcinoma (HCC)

All animal experiments were performed according to an institutionally approved protocol (protocol #: 803952) for the safe and humane treatment of animals. Autochthonous HCCs were induced in male Wistar rats with diethylnitrosamine according to established protocols[1,17]. Rats were regularly screened for tumor development, as previously described, with T_2-weighted MRI (FOV: 70 mm x 70 mm, Grid size: 256 x 256, Slice thickness: 2 mm, TR minimum: 1.4 s (respiratory gated), TE: 59.1 ms, Minimum averages: 4) within a Polarean proton-tuned (200.1 MHz) birdcage resonator using an Agilent 4.7T 40 cm horizontal bore MR Spectrometer with a 25 gauss/cm gradient tube interfaced to an Agilent DirectDrive console[1]. Individual HCC lesions of ~100 mm^3 were used for subsequent imaging studies.

DNP-[1-^{13}C]-pyruvate preparation

DNP-[1-^{13}C]-pyruvate was prepared by polarizing a mixture of 14 M [1-^{13}C]-pyruvate (Cambridge Isotopes), 15 mM OX063 radical (GE Healthcare) and 1.5 mM of Dotarem (Guerbet LLC) at ~1.4 K and using an excitation frequency of ~94.080 GHz in a HyperSense hyperpolarizer (Oxford Instruments), as previously described[1]. Upon saturation of polarization transfer, dissolution was performed in a buffer designed to ensure that the final injected solution was iso-osmolar to blood (300 mOsm) at a pH of 7.4 with a final pyruvate concentration of either 80 mM (for LD injections) or 160 mM (for HD injections). All injections were performed with the assistance of a high-pressure liquid chromatography (HPLC) pump through PEEK tubing at a dose of 6.7 mL/kg and speed of 10 mL/min as described above.

DNP-[1-^{13}C]-pyruvate imaging

Prior to imaging, each animal was centered within a Polarean proton-tuned (200.1 MHz) birdcage resonator with a ^{13}C-tuned (50.525 MHz) surface coil positioned over the tumor of interest. Baseline T_2-weighted imaging (as described above) was performed to confirm positioning and facilitate tumor ROI selection in the carbon data[1]. Animals received either LD or HD injections, up to a maximum of three total injections spaced no less than 45 minutes apart. LDHi injections were performed at a concentration of 10 mg/mL and a dose of either 10 mg/kg or 20 mg/kg by hand through tail vein injection at a rate of 1 mL/min and were followed by a 2 mL saline flush[18,19]. As animals received up to three pyruvate injections, data contributing to up to two experimental groups was collected on the same day. LDHi injections (if applicable) occurred between the final two injections.

DNP-^{13}C-MRSI was performed using a 2D spectroscopic imaging (EPSI) sequence with a spectral bandwidth of 1.1kHz and 128 points, enabling detection of a chemical shift range of 22 ppm, as discussed previously[1,20]. The total FOV was 60 mm x 45 mm with 12 phase encoded steps and 16 frequency encoded steps, enabling an in-plane resolution of 3.75 mm x 3.75 mm with a slice thickness matching the thickness of the tumor in the coronal plane (~6-10 mm). Each image was acquired in ~1 s with consecutive images repeated every ~2 s for a minimum of 20 scans per study after an initial delay of ~21 seconds to permit intratumoral accumulation of lactate and alanine.

Image analysis

Acquired proton images and EPSI spectra were reconstructed using MATLAB 2018B (Mathworks, Inc.). To ensure accurate quantification, B_1 correction, point spread function correction, polarization efficiency normalization, and baseline subtraction were performed as described previously and above[1]. A ^{13}C-Urea reference (165.5 ppm) permitted determination of chemical shift. Tumoral ROIs were specified using T_2-weighted images, which were then sampled from adjusted carbon data re-sampled with a cubic convolution and an eight-fold interpolation factor. Reported metabolite values and ratios represent the time-weighted area under the curve of metabolite quantifications (pyruvate: 170.4 ppm, lactate: 183.35 ppm, alanine: 176.5 ppm) from individual images when intratumoral SNR was ≥ 2.

Quantification of pyruvate concentration, LDH activity, and radical in biological samples

For experiments where serum and/or urine pyruvate and/or the radical source was quantified, animals were sedated prior to collection of baseline urine and serum samples. Subsequently animals were injected with LD pyruvate (^{13}C labeled, non-polarized, with 82.8 nM OX063 and 8.28 nM Dotarem) and maintained under anesthesia while subsequent samples were collected. Serum samples were deproteinized prior to quantification of pyruvate concentration with a Deproteinizing Sample Preparation Kit (Abcam, ab204708). Pyruvate measurements were made with the Biovision Pyruvate Assay Kit (K609). Electron paramagnetic resonance was performed on 10 uL urine samples sealed in glass tubes on a Bruker EPR spectrometer (center field = 3518 G, sweep width = 50 G, modulation frequency = 100 kHz, sweep time = 41.94 s).

For experiments in which tumor extracts were collected for analyses of LDH activity, animals were sacrificed by CO_2 euthanasia following the final LD injection. Tumor samples were harvested at necropsy and homogenized in assay buffer. Lactate dehydrogenase activity measurements were made with Biovision Lactate Dehydrogenase Assay Kit (K726).

Statistical Analyses

All statistical analyses were performed in RStudio Desktop 1.1.442; graphical representations of these data were made with RStudio, GraphPad Prism 8.2.1, or Matlab 2018B. Two-group comparisons utilize either two-sided Wilcoxon rank-sum or t tests dependent upon whether the assumption of normality was or was not disproven with the Shapiro-Wilk's test.

5.7: Fidelity of DNP Assessment to Biology: Results

Probe concentration affects apparent metabolic rate

Intratumoral metabolism of DNP-[1-^{13}C]-pyruvate was studied in a diethylnitrosamine-induced autochthonous rodent model of hepatocellular carcinoma. Sequential doses of DNP-[1-^{13}C]-pyruvate at two concentrations—80 mM at 6.7 mL/kg (low dose, LD) or 160 mM at 6.7 mL/kg (high dose, HD)—were used to test the hypothesis that measurements of intratumoral metabolism are sensitive to DNP probe dose. Figure 5.3 provides schematics that describe the relevant anatomy and experimental setup. DNP-[1-^{13}C]-pyruvate was injected through the tail vein using a semi-automated system

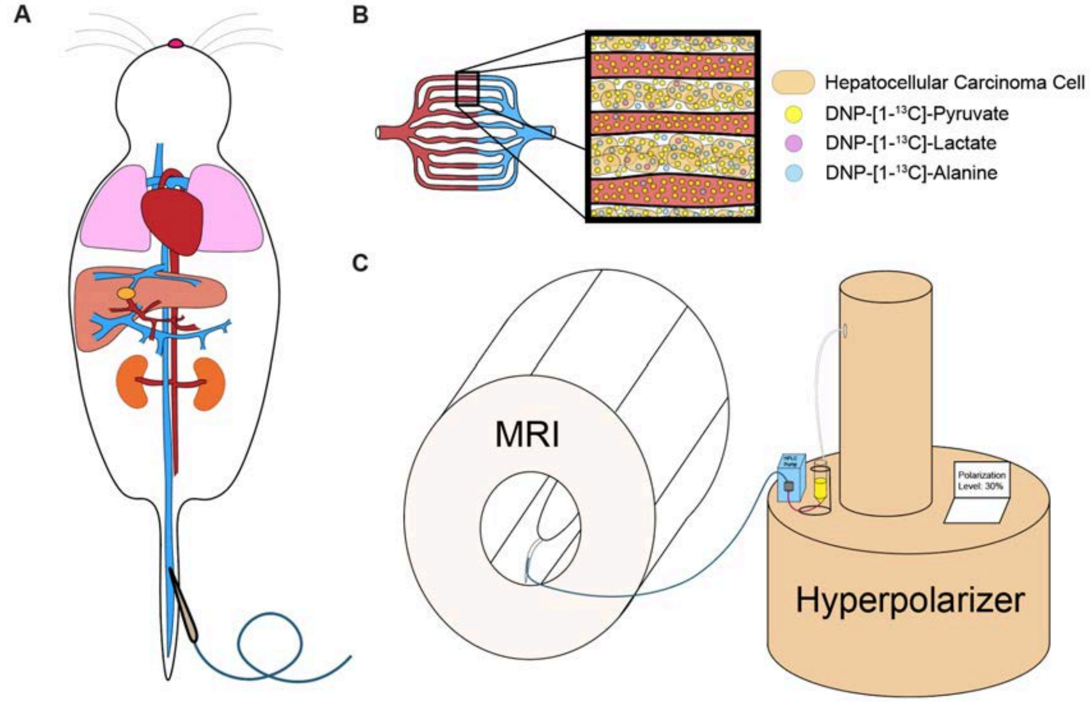

Figure 5.3: Schematics of relevant anatomy and experimental setup
(A) Schematic of relevant rat anatomy highlighting that DNP-^{13}C injections are performed through the tail vein. While the liver is predominantly supplied by the portal vein, HCC is supplied primarily by branches of the hepatic artery. Therefore, pyruvate arriving to the tumor takes the following path after injection: tail vein→inferior vena cava→right heart→pulmonary circuit→left heart/aorta→proper hepatic artery (via celiac artery)→tumor. (B) Schematic of a capillary bed within a tumor in the described model highlighting that the majority of measurable DNP-^{13}C signal is extracellular pyruvate, while the majority of measurable lactate and alanine is produced within tumor cells. (C) Schematic of the experimental setup that highlights a semi-automated method for DNP-[1-^{13}C]-pyruvate injection upon dissolution with the assistance of an HPLC pump.

including a high-pressure liquid chromatography (HPLC) pump to ensure reproducibility as well as to preserve polarization.

Intratumoral quantities of pyruvate, lactate, and alanine were quantified from sequentially acquired spectroscopic images after LD and HD injections. Figure 5.4A-D includes representative DNP-MRSI parametric maps of lactate-to-pyruvate (A, C) and spectra (B, D) comparing LD (A, B) and HD (C, D) injections. As the K_m value for pyruvate flux through monocarboxylate transporter 1 (MCT1)—the principal membrane transporter for pyruvate uptake in HCC cells—is approximately 1 mM, this process was hypothesized to be rate-limiting in both LD and HD injections [21]. At these concentrations, well in excess of that required for V_{max}, the majority of intratumoral ^{13}C signal originates from extracellular pyruvate (Figure 5.3B). Figure 5.4A, C qualitatively confirms a dramatic increase in pyruvate after HD injection relative to LD injection.

In aggregate (n=9), HD injections produced significantly different intratumoral metabolite fractions (relative to LD injections), including for pyruvate (t=3.4, df=8, p=8.83e-3, n=9) and lactate (t=-4.21, df=8, p=2.94e-3, n=9). Hence, the increase in pyruvate dose yielded a disproportionate increase in signal originating from pyruvate relative to its metabolites (Figure 5.4A-E).

Inter-metabolite ratio analysis is a versatile tool to quantify pyruvate metabolism, including forward flux to lactate via the lactate-to-pyruvate ratio [22]. Relative to LD, HD injection produced significantly altered inter-metabolite ratios, including lactate-to-pyruvate (t=-3.10, df=8, p=1.48e-2, n=9) and alanine-to-lactate (t=2.92, df=8, p=1.92e-2, n=9; Figure 5.4E). Figure 5.4A, C highlights the apparent reduction in lactate-to-pyruvate in a representative animal. Hence, a model-free analytic approach using inter-metabolite ratios, demonstrated that the apparent rate of pyruvate metabolism decreased with an increase in pyruvate concentration.

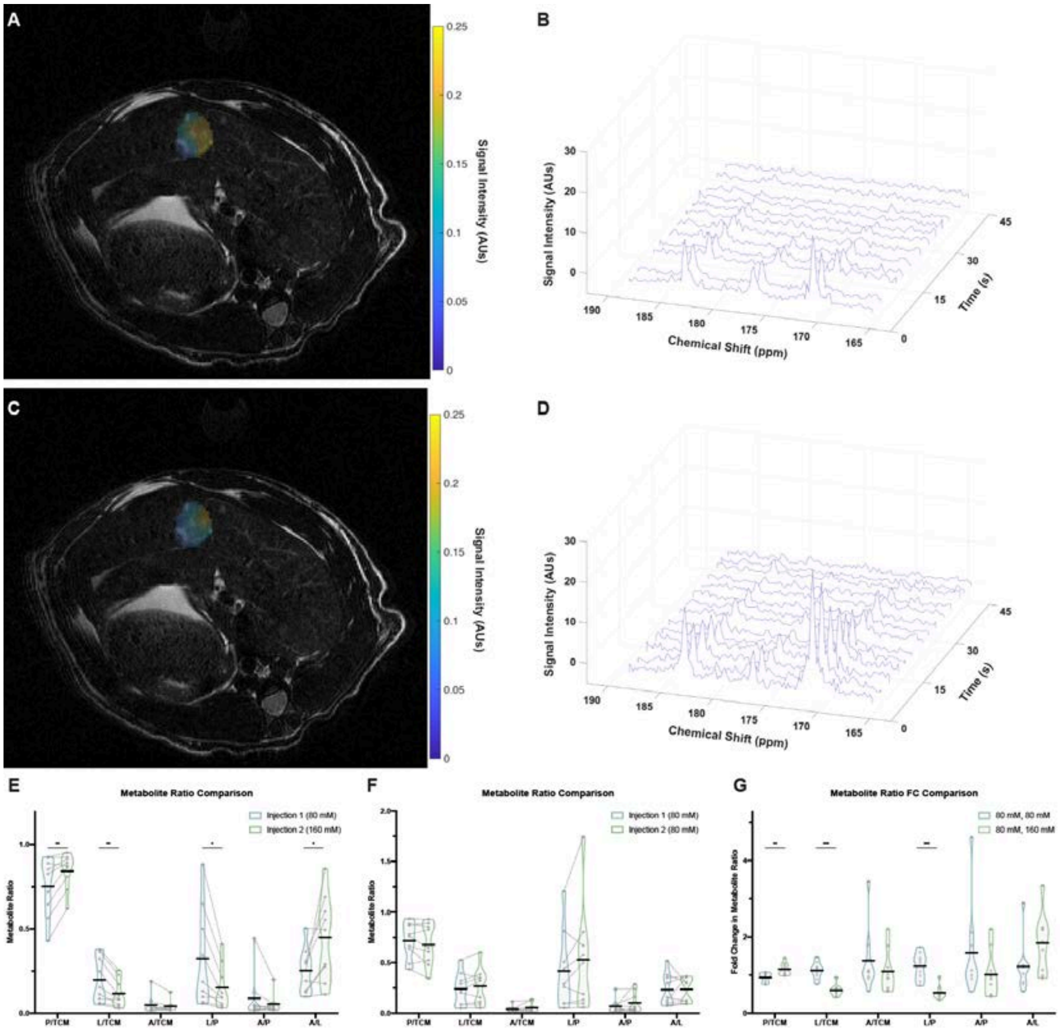

Figure 5.4: Apparent metabolism rates measured by inter-metabolite ratios are sensitive to probe dose.

(A, C) Parametric maps of the intratumoral lactate-to-pyruvate ratio after LD (A) and HD (C) injections in the foreground with a T_2-weighted ^{1}H image in the background. The lactate-to-pyruvate ratio is markedly reduced in the HD injection relative to the LD injection. (B, D) Waterfall plots of intratumoral spectra after an LD (B) and HD (D) injection. Pyruvate (δ: 176.5 ppm) levels increase dramatically after HD injection (relative to LD injection), while lactate (δ: 183.35 ppm) and alanine (δ: 170.4 ppm) amounts remained relatively constant. (E) Comparison of metabolite fractions and inter-metabolite ratios with LD followed by HD pyruvate injections. Significant changes are noted for P/TCM (p=8.83e-3), L/TCM (p=2.94e-3), L/P (p=1.48e-2), and A/L (p=1.92e-2). (F) Comparison of metabolite fractions and inter-metabolite ratios with sequential LD injections. No significant changes were appreciated. (G) Comparison of the fold-change in metabolite fractions and inter-metabolite ratios between an LD followed by HD injection and two sequential LD injections. Significant changes are noted for P/TCM (p=4.93e-3), L/TCM (p=3.60e-5), and L/P (p=1.65-4). [TCM = Total Carbon Metabolites = Pyruvate + Lactate + Alanine]

DNP-assessments of metabolism are repeatable

To verify that the observed variation in metabolism between LD and HD injections was greater than would be expected from variability in two sequential injections at the same concentration, sequential LD injections were performed. No significant changes in intratumoral metabolite fractions or inter-metabolite ratios were observed (Figure 5.4F). Direct comparison of the fold-change in these measurements between an LD and HD injection relative to two LD injections, confirmed that significant changes in the pyruvate fraction (t=-3.31, df=14.8, p=4.93e-3, n=9), the lactate fraction (t=-5.86, df=14.5, p=3.60e-5, n=9) and the lactate-to-pyruvate ratio (W=79, p=1.65-4, n=9) were indeed directly explained by the increase in pyruvate concentration (Figure 5.4G). While the ratio of pyruvate flux to alanine as compared to lactate (A/L) increased after HD injection (t=-2.92, df=8, p=1.92e-2, n=9), the magnitude of this change was not significant after adjusting for the variability observed in sequential LD injections (Figure 5.4E-G).

As a secondary confirmation that DNP-facilitated assessments of metabolism are repeatable, serum was collected at fixed times after an LD injection to quantify the time course for return to equilibrium. Serum pyruvate was significantly elevated five and ten minutes following an LD injection (t=4.17, df=5.18, p=8.07e-3, n=6; t=2.22, df=8.58, p=3.41e-2, n=7), and returned to within 10% of baseline within 45 minutes, the minimum timing between injections for the described studies (Figure 5.5A).

Excess pyruvate and radical are excreted into the urine

To assess for changes in urinary excretion of injected species, urine samples were collected before and after an LD injection, including pyruvate and the radical source (OX063). Pyruvate concentration after an LD injection was significantly elevated as compared to baseline (FC=1.69, t=-4.90, df=6, p=2.72e-3, n=7; Figure 5.5B). Visual comparison of urine collected before and after an LD injection demonstrated a substantial

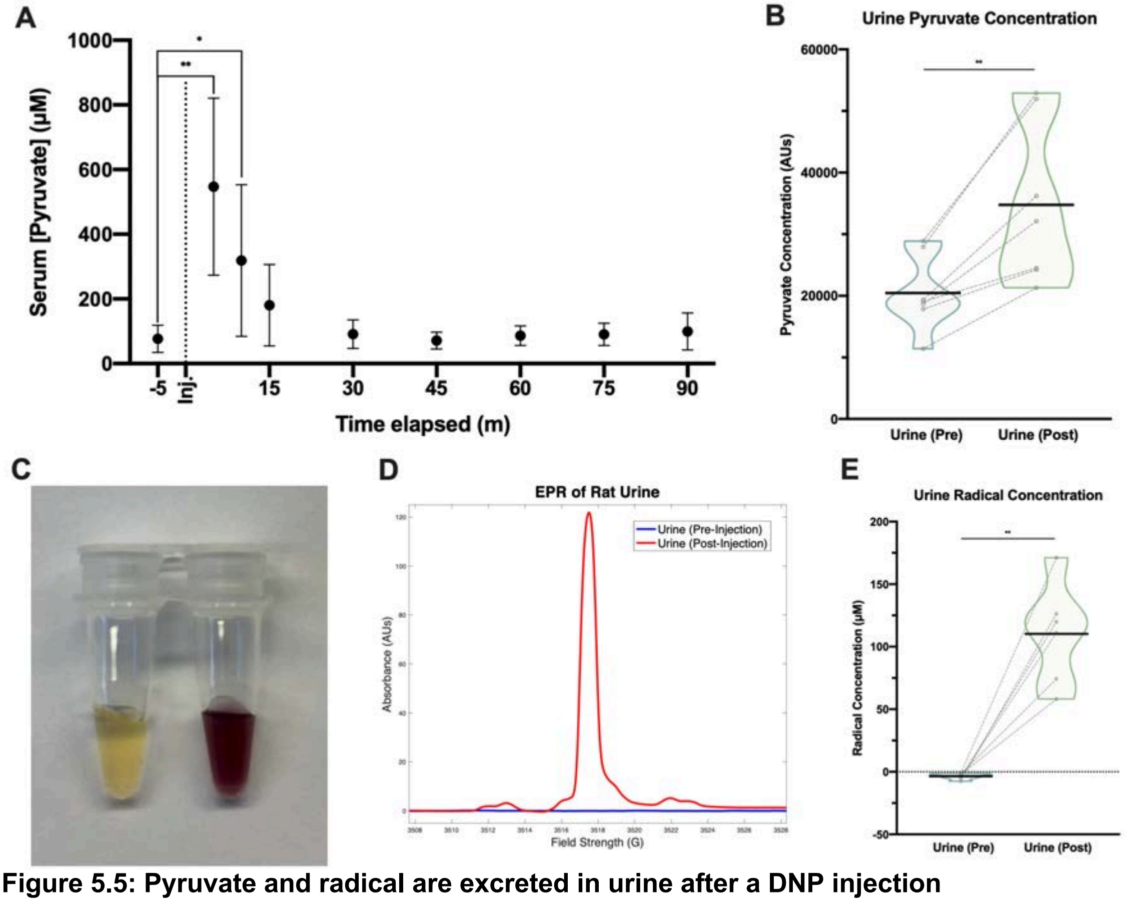

Figure 5.5: Pyruvate and radical are excreted in urine after a DNP injection
(A) Graphical representation of serum concentrations of pyruvate after a single LD injection. Pyruvate concentration is significantly elevated 5- and 10-minutes following injections (p=8.07e-3, 3.41e-2). (B) Urine pyruvate concentration are elevated after a single LD injection (p=2.72e-3). (C) Urine before (left) and after (right) a single LD injection reveals a substantial, qualitative change. (D) EPR of a representative pair of urine samples before and after a single LD injection reveals the presence of the radical source in the urine after injection, as confirmed in (E) by quantification of all samples (p=1.01e-3).

change in color consistent with excretion of the radical source (Figure 5.5C). Analysis by electron paramagnetic resonance confirmed and quantified the presence of the radical source in the urine after injection (average concentration=110.2 μM, t=6.86, df=5, p=1.01e-3, n=6; Figures 5.5D, 5.5E).

DNP-assessments of metabolism are sensitive to pharmacologic enzyme inhibition

An intravenously administered lactate dehydrogenase inhibitor (LDH, LDHi) was leveraged to study the sensitivity of DNP to changes in intracellular metabolism. LD injection and DNP acquisitions were performed both before and after LDHi injection at 20 mg/kg (Figure 5.6). LDHi precipitated a statistically significant change in the pyruvate fraction (t=4.38, df=10, p=1.39e-3, n=9), lactate fraction (t=-5.28, df=10, p=3.57e-4, n=9), lactate-to-pyruvate ratio (t=-4.30, df=10, p=1.55e-3, n=9), and alanine-to-lactate ratio (V=66, p=9.77e-4, n=9; Figure 5.6E). Upon controlling for the variability in these metabolite fractions and the inter-metabolite ratios observed with two LD injections in isolation, the fold-change after LDHi was significantly altered for these same comparisons, including: an increase in the pyruvate fraction (t=3.95, df=14.6, p=1.34e-3), decrease in the lactate fraction (t=8.84, df=16.7, p=1.05e-7), decrease in the lactate-to-pyruvate ratio (t=7.46, df=12.4, p=6.26e-6), as well as an increase in the alanine-to-lactate ratio (W=95, p=1.43e-4).

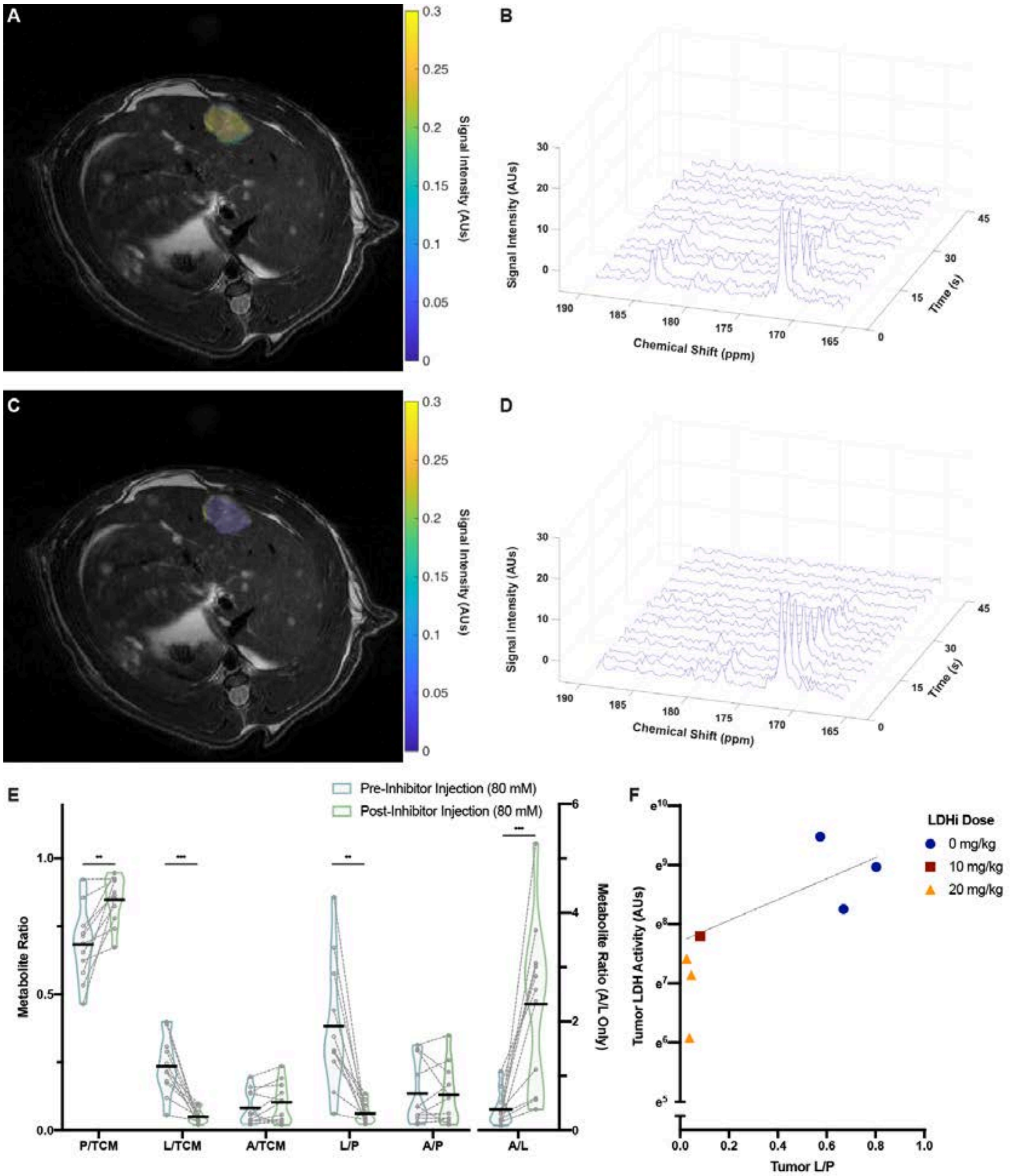

Figure 5.6: DNP quantifications of metabolism are sensitive to changes in intratumoral enzyme activity

(A, C) DNP-MRSI representations of the intratumoral lactate-to-pyruvate ratio before (A) and after (C) a 20 mg/kg LDHi injection in the foreground with a T$_2$-weighted ^{1}H image in the background. The lactate-to-pyruvate ratio is markedly reduced after LDHi. (B, D) Waterfall plots of intratumoral spectra before (B) and after (D) a 20 mg/kg LDHi injection. Lactate (δ: 183.35 ppm) levels increase dramatically after LDHi injection (relative to LD injection), while pyruvate (δ: 176.5 ppm) and alanine (δ: 170.4 ppm) levels rise a small amount. (E) Comparison of metabolite fractions and ratios when a 20 mg/kg LDHi administration is interposed between two sequential LD injections. Significant changes are noted for P/TCM (p=1.39e-3), L/TCM (p=3.57e-4), L/P (p=1.55e-3), and A/L (p=9.77e-4). (F) Measurements of LDH activity in tumor extracts harvested at necropsy significantly correlate with DNP-based measurement of LDH flux according to the L/P ratio (p=2.71e-2).

To assess the correspondence of DNP measured lactate-to-pyruvate ratios to LDH flux, lactate-to-pyruvate measures taken post-inhibition were compared to a biochemical assay of LDH activity performed on corresponding tumor extracts harvested at necropsy shortly after an LD injection. LDH activity in these tumor extracts were significantly correlated with intratumoral lactate-to-pyruvate measurements (p=2.71e-2; Figure 5.6F).

5.8: Fidelity of DNP Assessment to Biology: Conclusions

DNP-^{13}C-MRSI is capable of distinguishing a probe from its derivatives, facilitating quantification of locoregional metabolism. As the technique depends upon supraphysiologic metabolite concentrations, DNP-MRSI interpretation requires careful consideration of concentration-dependent effects on the effected disequilibrium and associated metabolism. While prior work has demonstrated that supraphysiologic concentrations of metabolites impact the apparent rate of metabolism, most of this work has been done in cells, perfused tissues or xenograft models[12–16]. This study extends upon this foundation by using an autochthonous tumor model that more closely mimics the complexity of human disease.

These data confirm that probe dose influences local metabolite fractions, altering apparent metabolism rate according to a model-free approach using the lactate-to-pyruvate ratio. While a multi-compartment model could account for differences in substrate delivery, ratiometric analyses of regional metabolites have been found to approximate these findings in clinically relevant settings where measurement of an input function is challenging[8,22]. Indeed, a recent clinical trial demonstrating a correlation between prostate cancer grade and intratumoral lactate generation utilized model-free analyses to arrive at its principal conclusions[8]. Furthermore, acquisitions initiated after substrate delivery to the tumor—which prolong bulk hyperpolarization and enhance sensitivity to metabolite accumulation—preclude traditional approaches to multi-compartment modeling.

The concentration dependence of metabolite fractions and inter-metabolite ratios principally derives from transport limitation. Intratumoral extracellular pyruvate concentrations following DNP injections are likely well in excess of those necessary for MCT1 to operate at V_{max} ($2*K_m$, ~ 2 mM in humans[21]). Relative increases in injected pyruvate concentration yield minimal increases to the intracellular fraction of pyruvate, and—by extension—intracellularly generated metabolites. The majority of the increase in signal issues from intravascular and extracellular pyruvate. This finding is consistent with the observation that in patients with prostate cancer, lactate generation correlates with MCT1 expression[8]. Small increases in intracellular pyruvate may help explain the mild relative increase in alanine production as compared lactate. Specifically, as the pyruvate specific K_m for ALT (~ 1 – 12.5 mM[23,24]) is larger than that of LDH (~ 0.4 mM[25]), small increases in pyruvate concentration are likely to differentially enhance flux through ALT.

The observed concentration dependence of these analyses highlights that the interpretation of model-free, DNP-based metabolism assessments requires comparison to a baseline—such as a prior scan or nearby tissue. Beyond altering the concentration of injected material, inter-subject specific variations in circulation time, tumor vasculature, and extra-tumoral metabolism/excretion are likely to contribute to variability in intra-tumoral substrate concentration.

Equilibrium restoration is of particular concern for multi-injection studies, including evaluation of treatment response according to a change in imaging findings. The observed concentration dependence of apparent metabolism is independent of hyperpolarization status as elevated concentrations of non-polarized substrate retained in circulation are likely to influence subsequent measures of metabolism if equilibrium is not first restored.

Previously, Hu et al. found regional changes with 3D-MRSI in the liver, muscle, and the GI system when injections were spaced 5 minutes apart[12]. By contrast, in human patients, little difference was noted for two sequential injections an hour apart[8]. This work delineates that pyruvate concentration in the serum remains elevated for at least ten minutes following an injection and is within 10% of baseline within 45 minutes after injection. For repeat LD injections spaced 45 minutes or more apart, no differences in metabolism quantifications were appreciated. Prior to equilibrium restoration, repeated evaluations of metabolism with DNP are likely to be influenced by elevated serum concentration of non-polarized substrate.

Pyruvate concentrations normalize through a combination of metabolism and excretion. Pyruvate is a small organic acid, similar in structure to other small organic acids known to be reabsorbed in the proximal tubule of the nephron; pyruvate that is not reabsorbed from the filtrate is excreted in urine, as demonstrated herein[26]. In addition, the observation that OX063 is excreted in urine is consistent with the findings of those who performed EPR imaging and reclaimed this costly agent[27].

The final series of presented experiments with an LDHi demonstrate a mechanistic strength of DNP as compared to PET. With a direct measure of a substrate's fate, it is possible to delineate changes to intracellular processes in real-time. The experiments present an application of DNP as a means to directly quantify drug pharmacokinetics and pharmacodynamics that are consistent with prior work[28,29]. They extend upon the existing literature to confirm, with an independent measure of LDH activity, that the model-free approach to measuring enzyme flux with the lactate-to-pyruvate ratio is reflective of a change in enzyme activity.

DNP enables non-invasive functional imaging that can aid in the evaluation and treatment of disease. As clinical adoption of this modality grows, it remains essential that interpretation of image quantifications reflect the limitations of the underlying technology. Particularly as new agents and organ systems are studied, analogous studies of excretion and reproducibility in human subjects will facilitate meaningful distinction of spatial and temporal variation in metabolism. This work demonstrates that DNP-MRSI is sensitive to local assessment of metabolism, while underscoring that accurate interpretation requires consideration of probe dose and administration frequency.

5.9: References

1. Perkons, N. R. *et al.* Hyperpolarized Metabolic Imaging Detects Latent Hepatocellular Carcinoma Domains Surviving Locoregional Therapy. *Hepatology* (2019). doi:10.1002/HEP.30970
2. Shukla, A. K. & Kumar, U. Positron emission tomography in medicine: An overview. *J. Med. Phys.* **31**, 13–21 (2006).
3. Keshari, K. R. & Wilson, D. M. Chemistry and biochemistry of 13C hyperpolarized magnetic resonance using dynamic nuclear polarization. *Chem. Soc. Rev.* **43**, (2014).
4. Yen, Y. F. *et al.* Imaging considerations for in vivo 13C metabolic mapping using hyperpolarized 13C-pyruvate. *Magn. Reson. Med.* **62**, 1–10 (2009).
5. Insko, E. K. & Bolinger, L. Mapping of the Radiofrequency Field. *J. Magn. Reson.* **103**, 82–85 (1992).
6. Overhauser, A. W. Polarization of nuclei in metals. *Phys. Rev.* **92**, 411–415 (1953).
7. Abragam, A. & Goldman, M. Principles of dynamic nuclear polarisation. *Reports Prog. Phys.* **41**, 395–467 (1978).
8. Granlund, K. L. *et al.* Hyperpolarized MRI of Human Prostate Cancer Reveals Increased Lactate with Tumor Grade Driven by Monocarboxylate Transporter 1. *Cell Metab.* **31**, 105–114 (2020).
9. Nelson, S. J. *et al.* Metabolic imaging of patients with prostate cancer using hyperpolarized [1-^{13}C]Pyruvate. *Sci. Transl. Med.* **5**, 1–10 (2013).
10. Miloushev, V. Z. *et al.* Metabolic imaging of the human brain with hyperpolarized 13C Pyruvate demonstrates 13C lactate production in brain tumor patients. *Cancer Res.* **78**, 3755–3760 (2018).
11. Gallagher, F. A. *et al.* Imaging breast cancer using hyperpolarized carbon-13 MRI. *Proc. Natl. Acad. Sci.* **117**, 2092–2098 (2020).
12. Hu, S. *et al.* Rapid sequential injections of hyperpolarized [1-13C]pyruvate in vivo using a sub-kelvin, multi-sample DNP polarizer. *Magn. Reson. Imaging* **31**, 490–496 (2013).
13. Zierhut, M. L. *et al.* Kinetic modeling of hyperpolarized13C1-pyruvate metabolism in normal rats and TRAMP mice. *J. Magn. Reson.* **202**, 85–92 (2010).
14. Takado, Y. *et al.* Hyperpolarized 13C Magnetic Resonance Spectroscopy Reveals the Rate-Limiting Role of the Blood-Brain Barrier in the Cerebral Uptake and Metabolism of L-Lactate in Vivo. *ACS Chem. Neurosci.* **9**, 2554–2562 (2018).
15. Balzan, R. *et al.* Pyruvate cellular uptake and enzymatic conversion probed by dissolution DNP-NMR: the impact of overexpressed membrane transporters. *Magn. Reson. Chem.* **55**, 579–583 (2017).
16. Kadlecek, S. *et al.* The effect of exogenous substrate concentrations on true and apparent metabolism of hyperpolarized pyruvate in the isolated perfused lung. *NMR Biomed.* **27**, 1557–1570 (2014).
17. Kiefer, R. M. *et al.* Relative Initial Weight Is Associated with Improved Survival without Altering Tumor Latency in a Translational Rat Model of Diethylnitrosamine-Induced Hepatocellular Carcinoma and Transarterial Embolization. *J. Vasc. Interv. Radiol.* **28**, 1043–1050 (2017).
18. Yeung, C. *et al.* Targeting Glycolysis through Inhibition of Lactate Dehydrogenase Impairs Tumor Growth in Preclinical Models of Ewing Sarcoma. *Cancer Res.* **79**, 5060–5073 (2019).
19. Rai, G. *et al.* Discovery and Optimization of Potent, Cell-Active Pyrazole-Based

Inhibitors of Lactate Dehydrogenase (LDH). *J. Med. Chem.* **60**, 9184–9204 (2017).

20. Basic Practical NMR Concepts : A Guide for the Modern Laboratory. *Max T. Rogers NMR Facility* 1–41 (2013).
21. Hong, C. S. *et al.* MCT1 Modulates Cancer Cell Pyruvate Export and Growth of Tumors that Co-express MCT1 and MCT4. *Cell Rep.* **14**, 1590–1601 (2016).
22. Hill, D. K. *et al.* Model Free Approach to Kinetic Analysis of Real-Time Hyperpolarized 13C Magnetic Resonance Spectroscopy Data. *PLoS One* **8**, 1–9 (2013).
23. McAllister, C. H., Facette, M., Holt, A. & Good, A. G. Analysis of the Enzymatic Properties of a Broad Family of Alanine Aminotransferases. *PLoS One* **8**, 1–9 (2013).
24. Glinghammar, B. *et al.* Detection of the mitochondrial and catalytically active alanine aminotransferase in human tissues and plasma. *Int. J. Mol. Med.* **23**, 621–631 (2009).
25. Pettit, S. M., Nealon, D. A. & Henderson, A. R. Purification of lactate dehydrogenase isoenzyme-5 from human liver. *Clin. Chem.* **27**, 88–93 (1981).
26. Ferrier, B., Martin, M. & Bavarel, G. Reabsorption and secretion of alpha-ketoglutarate along the rat nephron: a micropuncture study. *Am. J. Physiol. Renal Physiol.* **248**, F404–F412 (1985).
27. Serda, M., Wu, Y. K., Barth, E. D., Halpern, H. J. & Rawal, V. H. EPR Imaging Spin Probe Trityl Radical OX063: A Method for Its Isolation from Animal Effluent, Redox Chemistry of Its Quinone Methide Oxidation Product, and in Vivo Application in a Mouse. *Chem. Res. Toxicol.* **29**, 2153–2156 (2016).
28. Oshima, N. *et al.* Dynamic Imaging of LDH Inhibition in Tumors Reveals Rapid in vivo Metabolic Rewiring and Vulnerability to Combination Therapy. *Cell Rep.* **30**, 1798–1810 (2020).
29. Dutta, P. *et al.* Evaluation of LDH-A and glutaminase inhibition in vivo by hyperpolarized13C-pyruvate magnetic resonance spectroscopy of tumors. *Cancer Res.* **73**, 4190–4195 (2013).

Chapter 6: Hyperpolarized Metabolic Imaging Detects Latent Hepatocellular Carcinoma Domains Surviving Locoregional Therapy

6.1: Introduction

This chapter is adopted from an article by Perkons et al. in *Hepatology* that was published in 2019 entitled "Hyperpolarized Metabolic Imaging Detects Latent Hepatocellular Carcinoma Domains Surviving Locoregional Therapy"[1]. The chapter details how metabolic reprogramming after transarterial embolization can be directly imaged with DNP-[1-^{13}C]-pyruvate, demonstrating that functional assessment of pyruvate metabolism predicted therapeutic response on the basis of histologic viability.

6.2: Abstract

Advances in cancer treatment have improved survival; however, local recurrence and metastatic disease—the principal causes of cancer mortality—have limited the ability to achieve durable remissions. Local recurrences arise from latent tumor cells that survive therapy and are not detectable by conventional clinical imaging techniques. Local recurrence after transarterial embolization (TAE) of hepatocellular carcinoma (HCC) provides a compelling clinical correlate of this phenomenon. In response to TAE-induced ischemia, HCC cells adapt their growth program to effect a latent phenotype that precedes local recurrence. In this study, we characterize and leverage the metabolic reprogramming demonstrated by latent HCC cells in response to TAE-induced ischemia to enable their detection *in vivo* using dynamic nuclear polarization magnetic resonance spectroscopic imaging (DNP-MRSI) of ^{13}Carbon-labeled substrates. Under TAE-induced ischemia, latent HCC cells demonstrate reduced metabolism and develop a dependence on glycolytic flux to lactate. Despite the hypometabolic state of these cells, DNP-MRSI of 1-^{13}C-pyruvate

and its downstream metabolites, 1-^{13}C-lactate and 1-^{13}C-alanine, predicted histologic viability. These studies provide a novel paradigm for imaging treatment-refractory cancer cells that are undetectable using existing clinical imaging paradigms suggesting that DNP-MRSI provides a unique technology for this application.

6.3: Introduction

Advances in our understanding of tumor biology and technology have led to the development of novel targeted and locoregional therapies with improved response rates, transforming the prognoses of certain cancers from terminal into chronic diseases[2]. Improved survival has been accompanied by a concomitant increase in the incidence of recurrent local and metastatic disease[3,4]. These recurrences are thought to arise from cancer latency wherein remnant or disseminated cancer cells persist without detectable growth[5]. Given that the large majority of cancer-related deaths result from metastatic disease, the ability to characterize and ultimately target latent cancer cells will prove critical in transforming cancer prognoses again from chronic disease to cure. The central role played by diagnostic imaging in monitoring therapeutic response dictates that this ability will be predicated on the capability to detect latent disease *in vivo*. However, conventional imaging approaches detect features of active tumors, such as tumor growth and vascularity, but have a demonstrated deficiency in ability to distinguish tumor necrosis from latent cancer[2,6,7].

The response of hepatocellular carcinoma (HCC) following treatment with transarterial embolization (TAE) provides a compelling example of this important clinical deficiency. TAE, the most common treatment for HCC in the United States[8], exploits the vascular biology of HCC to deprive tumors of nutrients through the targeted delivery of embolics (with or without chemotherapy) to the hepatic arteries feeding the tumor. The presence of viable tumor cells adjacent to necrotic regions on histopathology of explanted tumors following TAE underscores the adaptive response of HCC to nutrient deprivation[9]. This adaptive response may result in the observed clinical imaging phenotype of latent HCC surviving TAE that is undetectable using current clinical imaging approaches leading to frequent local recurrences that occur within months of treatment after a complete response. As a result, current imaging paradigms fail to guide optimal therapy by informing the need for repeat interventions[7]. Several approaches have been applied in attempts to overcome this limitation including contrast-enhanced (CE) CT[10], CEMRI[11], and diffusion-weighted MRI[12]. However, these measurements may be confounded by the replacement of necrotic tissue with healthy liver parenchyma, the presence of iodized oils on CECT, or granulation tissue on CEMRI. Furthermore, these strategies do not provide direct measures of cellular viability. This deficiency reflects a fundamental mismatch between conventional imaging approaches and the biology they seek to characterize, emphasizing the need for functional imaging paradigms to detect latent cancer.

Previously, we demonstrated that HCC cells surviving TAE-like ischemia activate, and are dependent on, a metabolic stress response underscoring the primary role of altered tumor metabolism in their survival[13]. These data indicate that the changes in overall metabolic flux and intratumoral metabolites associated with the adapted metabolic equilibrium in latent tumor cells may constitute a unique fingerprint that enables their detection. While ^{18}Fluorodeoxyglucose Positron Emission Tomography (^{18}F-FDG-PET) has revolutionized cancer imaging by leveraging the increased glucose utilization that characterizes many cancers to facilitate detection, it has limited potential for multi-parametric measurement and is not effective in all tumor types, including one third of HCCs[14,15]. Nuclear magnetic resonance spectroscopic imaging (MRSI) enhanced by dynamic nuclear polarization (DNP) enables detailed assessment of metabolism *in vivo*.

This technology represents a unique resource to translate advances in our understanding of the metabolic alterations enabling cancer latency for non-invasive diagnostic imaging. Through signal enhancement, DNP-^{13}C-MRSI enables simultaneous spatial and kinetic readouts of metabolic activity in near real-time[16]. Herein, we describe the characterization of metabolic alterations in latent HCC cells surviving TAE-induced ischemia to enable a sensitive and specific DNP-^{13}C-NMRS imaging approach for the non-invasive detection of latent cancer cells *in vivo*.

6.4: Results

Post-TAE-Ischemia Induces Latency In Vivo and In Vitro

In order to characterize ischemia-induced tumor latency, we performed TAE in an autochthonous, diethylnitrosamine (DEN)-induced rat model of HCC as described previously[17,18]. Treated tumors demonstrated a marked reduction in volumetric growth relative to untreated controls (n=3/group, Figure 6.1 A-C), consistent with clinical observations. As compared to untreated tumors, histologic staining of treated tumors demonstrated regions of sustained viability with viable cells showing a decrease in proliferative status as indicated by reduced staining for proliferating cell nuclear antigen (PCNA). This was accompanied by the activation of a metabolic stress response as indicated by an increase in the stabilization of hypoxia-inducible factor 1α (Figure 6.1D, E). The juxtaposition of growth-arrested, latent cancer cells amongst necrotic cells underscored the adaptive response of HCC to nutrient deprivation, which current imaging techniques fail to detect.

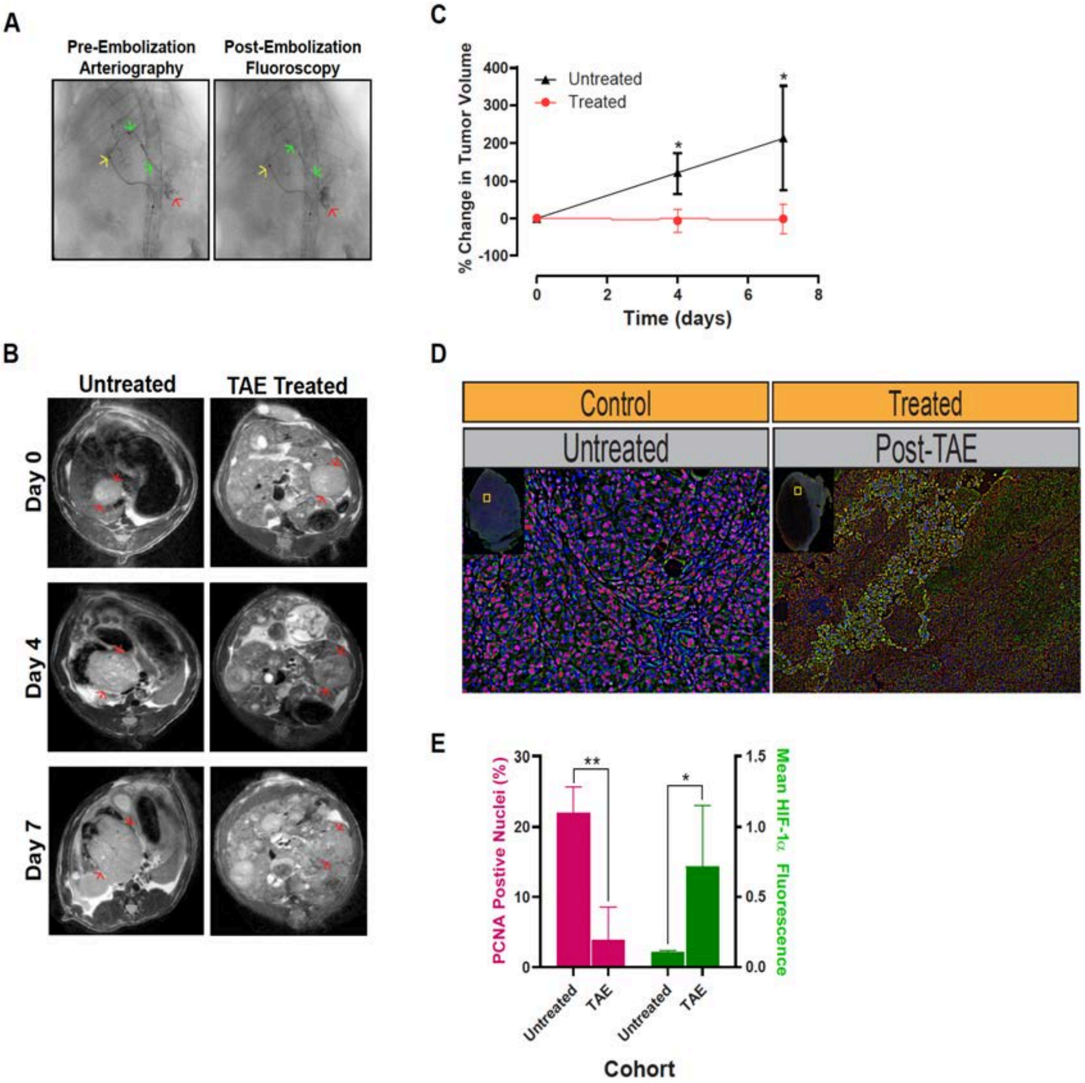
A
Pre-Embolization Arteriography
Post-Embolization Fluoroscopy
B
Untreated
TAE Treated
Day 0
Day 4
Day 7
C
% Change in Tumor Volume
400
300
200
100
0
-100
Untreated
Treated
*
*
0
2
4
6
8
Time (days)
D
Control
Treated
Untreated
Post-TAE
E
PCNA Postive Nuclei (%)
30
20
10
0
**
*
Mean HIF-1α Fluorescence
1.5
1.0
0.5
0.0
Untreated
TAE
Untreated
TAE
Cohort

Figure 6.1 Post-TACE Ischemia Induces Growth Latency *In Vivo*. (A) Representative pre-embolization arteriogram demonstrates positioning of the microcatheter in the left hepatic artery (→) with contrast extending to (→) and staining the tumor (→). Post-embolization fluoroscopy demonstrates stasis of contrast within the left hepatic branch artery feeding the tumor as well as persistent contrast staining the tumor. (B) Representative serial T_2-weighted MR images of untreated, control HCCs and treated HCCs prior to and following TAE. (C) Growth curves derived from MR-based measurements of tumor volume in untreated HCCs and treated HCCs prior to and following TACE demonstrated a significant reduction in growth for TAE-treated tumors ($p = 0.011$ at posttreatment day 4; $p = 0.029$ at posttreatment day 7). Tumor volumes are normalized to the first measurement and reported as the average percent change in volume ± standard deviation. (D) Representative immunofluorescence images of untreated control and TAE treated (post-treatment day 7) tumors stained for PCNA (pink) and HIF-1α (green). (E) Bar graph demonstrating a significant reduction in the percentage of DAPI+ nuclei that are also PCNA+ in treated tumors relative to untreated tumors as well as increase in mean HIF-1α fluorescence intensity per DAPI+ stained nucleus (PCNA: 3.9 ± 4.6% vs 22.0 ± 3.7%, p=.006; HIF-1α: .75 ± .39 vs .11 ± .01, p=.048).

To characterize the metabolic alterations of latent HCC cells, we validated an *in vitro* model of TAE-like ischemia based on these *in vivo* data. Rat HCC (HR2) cells, derived from autochthonous, DEN-induced HCCs in Wistar rats, were cultured under nutrient-limiting conditions. Consistent with our previously described data in human HCC cell lines, rat HR2 cells incubated under severe ischemia (1% O_2 with medium containing 1% serum, 1 mM glucose and 0.5 mM glutamine) mimicked the post-TAE *in vivo* growth delay, demonstrating sustained viability for up to one week without proliferation (Figure 6.S1A, B). Interestingly, in experiments designed to mimic the revascularization that follows TAE, cells incubated under severe ischemia for one week were then incubated under replete conditions. HR2 cells regained an exponential growth kinetic consistent with the clinical imaging phenotype of recurrent HCC following a period of latency after TAE (Figure 6.S1A, B). Consistent with our previously described data in human HCC cell lines, latent HR2 cell populations surviving severe ischemia demonstrated a significant increase in the fraction of non-proliferating cells with 55.4 ± 3.1% of cells in the G_0 phase of the cell cycle versus 18.2 ± 1.1% of cells incubated under standard conditions (Figure 6.S1C, D; $p<.0001$). Latent HCC cells also demonstrated a significant decrease in the fraction of cells in the S phase of the cell cycle (8.4 ± 1%) as compared to cells grown under standard conditions (18.3 ± .4%) in keeping with a reduced proportion of actively dividing cells (Figure 6.S1C, D; $p=.001$). Taken together, these data indicate that ischemia induces a latent and quiescent HCC cell population. This finding was corroborated by increased expression of the cyclin-dependent kinase inhibitor $p27^{Kip1}$ in HR2 cells as we have demonstrated previously in human HCC cell lines (Figure 6.S1E). Consistent with the above-described *in vivo* data, latent HCC cells demonstrated an increase in stabilization of HIF-1α *in vitro* (Figure 6.S1E).

Latent HCC Cells Are Hypometabolic

These data indicate that HCC cells surviving severe ischemia suppress their metabolism and proliferative rate to enable latency. Indeed, HCC cells surviving severe ischemia demonstrated biochemical and molecular alterations consistent with the hypometabolic state seen in latent cancer cells. These cells exhibited activation of AMPK, a master cellular energy sensor that inhibits ATP-consuming anabolic programs and activates ATP-producing catabolic programs, as well as downregulation of mTOR pathway activity, as evidenced by decreased Phospho-S6 despite equivalent levels of mTOR, which stimulates ATP-consuming anabolic processes (Figure 6.2A). Consistent with these findings, latent HCC cells demonstrated profound reductions in the anabolic metabolism that promotes cancer cell growth including nucleotide, lipid and protein biosynthesis (Figure 6.2B, C). HR2 and SNU-387 cells were incubated in either complete or ischemic medium conditions for 48 hours and cell extracts were submitted for global metabolic

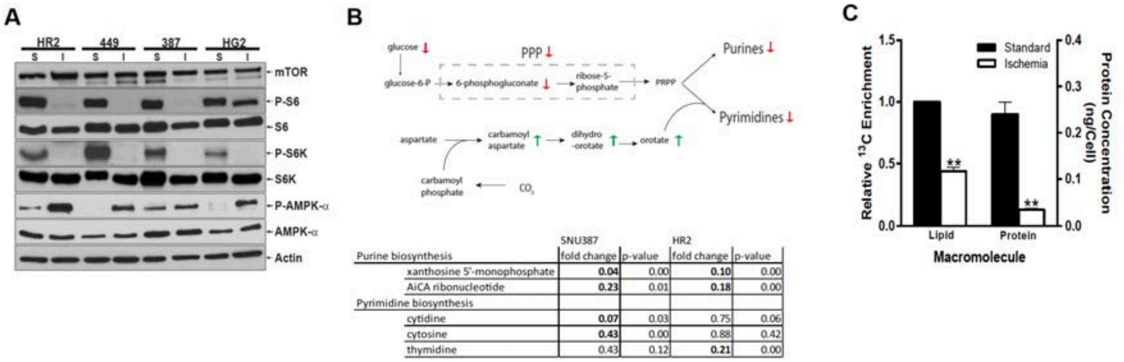

	SNU387		HR2	
Purine biosynthesis	fold change	p-value	fold change	p-value
xanthosine 5'-monophosphate	**0.04**	0.00	**0.10**	0.00
AICA ribonucleotide	**0.23**	0.01	**0.18**	0.00
Pyrimidine biosynthesis				
cytidine	**0.07**	0.03	0.75	0.06
cytosine	**0.43**	0.00	0.88	0.42
thymidine	0.43	0.12	**0.21**	0.00

Figure 6.2 Latent HCC Cells Are Hypometabolic. (A) Western blots demonstrating suppression of the mTOR pathway, as supported by decreased Phospho-S6 levels despite sustained mTOR levels, and activation of the AMPK pathway in three human HCC (449, 387 and HG2) cell lines and one rat (HR2) HCC cell line exposed to ischemic (I) as compared standard conditions (S). (B) Metabolomic profiling of cells grown under ischemic vs. standard conditions demonstrates a reduction in intermediates of purine and pyrimidine biosynthesis in human (SNU387) and rat (HR2) HCC cell lines. (C) NMR extracts of HR2 cells incubated with 1-^{13}C-acetate and surviving ischemic conditions demonstrated significant reductions in the synthesis of de novo lipids as compared to cells grown under standard conditions (p = 0.0013). Similarly, bicinchoninic acid assay protein measurements demonstrated significant reductions in protein synthesis for HR2 cells surviving severe ischemia as compared to cells grown under standard conditions (p = 0.0086).

profiling. Among the many changes observed in ischemic cells compared to their controls, we identified significantly decreased levels of intermediates of purine and pyrimidine biosynthesis (Figure 6.2B). These changes were seen despite elevated levels of orotate, an important precursor, indicating that limited phosphoribosyl pyrophosphate (PRPP) availability attributable to reduced glucose carbon flux through the pentose phosphate pathway may be the cause of reduced purine and pyrimidine biosynthesis**.** Similarly, latent HCC cells demonstrated a significant reduction in de novo lipogenesis and protein synthesis (Figure 6.2C). Each of these metabolic alterations indicate a concerted shift away from cell growth.

Latent HCC Cells Undergo Metabolic Reprogramming to Enable Survival Under Severe Ischemia

These alterations suggest that latent HCC cells surviving severe ischemia effect a deliberate agenda of metabolic reprogramming to enable survival. To test this hypothesis, we performed unbiased proteomic profiling of HR2 cells incubated under standard and ischemic conditions with a stable isotope of glucose (U-$^{13}C_6$-glucose). Consistent with the data described in Figure 6.2C, these data demonstrated a significant reduction in proteins synthesized from glucose (Figure 6.3A); however, while global translation was reduced, we also queried the global proteome to identify proteins that increased, rather than decreased under ischemia. Remarkably, higher peptide levels were detected for almost all enzymes directly involved in glycolysis in HCC cell populations grown under ischemia compared to HCC cells grown under standard conditions (Figure 6.3B). This increase in the synthesis of glycolytic enzymes was accompanied by translational and post-translational alterations in the enzymes that metabolize pyruvate in the final step of glycolysis (Figure 6.3C). Western blots for these proteins demonstrated increases in the levels of lactate dehydrogenase A (LDHA) and the activated, phosphorylated form of LDHA as well as inactivation of pyruvate dehydrogenase through phosphorylation in HCC cells surviving severe ischemia (Figure 6.3C). In addition, these cells demonstrated an increase in the levels of pyruvate carboxylase, likely on the basis of anapleurosis, while no change was observed in the levels of glutamic-pyruvic transaminase (GPT), (aka alanine aminotransferase (ALT)). Consistent with these data, while these alterations were associated with a reduction in glucose uptake (Figure 6.3D), latent HR2 cells surviving severe ischemia demonstrated an increase in conversion of glucose to lactate relative to alanine as compared to cells grown under standard conditions (Figure 6.3E)[19]. Indeed, latent HCC cells were dependent on this metabolic reprogramming as demonstrated by the necessity of LDH for survival. The chemical inhibition of LDH (LDHi, 2.5 μM) resulted in the near complete abrogation of lactate synthesis in HR2 cells grown under standard and ischemic conditions (Figure 6.3F). However, while cells cultured under standard conditions with LDHi demonstrated persistent growth and viability, cells cultured under ischemic conditions with LDHi failed to maintain viability beyond 48 hours (Figure 6.3G)[20,21]. Taken together, these data demonstrate that HCC cells surviving TAE-like ischemia cells undergo metabolic reprogramming of glycolysis to shunt glucose carbons away from anabolic processes and towards lactate. This suggests that metabolic imaging of pyruvate metabolism may provide the sensitivity required to detect this latent cell population (Figure 6.3H).

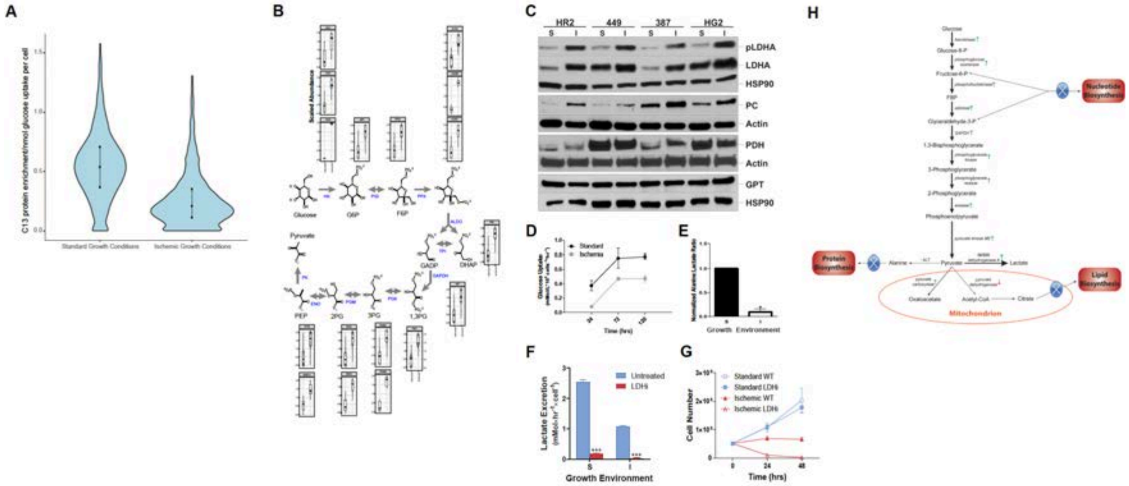

Figure 6.3 Latent HCC Cells Undergo Metabolic Reprogramming. (A) HR2 cells grown under severe ischemia with 1-^{13}C-glucose demonstrated lower C13-labeled protein enrichment as compared to cells grown under standard conditions, indicating reduced translation from glucose-derived alanine ($p<2.2e-16$). (B) Abundance of total peptide (C13 and C12 combined) graphed after normalization to mean peptide abundance for all peptides mapping to glycolytic enzymes reveals consistent increase in abundance of glycolytic enzymes under ischemia, despite overall reduction in translation. (C) Western blots demonstrating translational and post-translational alterations in the enzymes that metabolize pyruvate in the final step of glycolysis in cells surviving severe ischemia (I) relative to cells grown under standard conditions (S), including an increase in the levels of LDHA and its activated, phosphorylated form. In addition, phosphorylation of pyruvate dehydrogenase to its inactive form was observed as a band shift toward a higher molecular weight. (D) Despite these alterations, metabolic analyses demonstrated a reduction in glucose uptake for cells surviving severe ischemia ($p = 0.0004$). (E) NMR spectroscopy of cell extracts incubated with U-13C-glucose demonstrated alterations in glycolytic flux consistent with the above-described changes in protein expression with a significant reduction in the alanine:lactate ratio ($p = 0.03$). (F, G) Chemical inhibition of LDH (LDHi 737, 2.5 μM) resulted in the suppression of lactate excretion for HCC cells grown under standard and ischemic conditions within 24 hours of incubation; however, cells grown under ischemia were unable to survive these conditions when LDH was inhibited ($p < 0.0001$ for comparisons of lactate excretion rate under standard and ischemic conditions). (H) Schematic illustrating metabolic reprogramming of HCC cells surviving severe ischemia to limit anabolism and shunt glucose towards carbons toward lactate.

DNP-13C-NMR Spectroscopy and Spectroscopic Imaging Enable Detection of Latent HCC Cells In Vitro and In Vivo

To test the potential to leverage this metabolic reprogramming for detection of latent HCC cells using hyperpolarized 1-^{13}C-pyruvate, we developed an NMR-compatible, radial flow, cell perfusion bioreactor. In an experiment designed to mimic TAE-induced, severe ischemia, HR2 cells initially perfused with normoxic (0.21 mM/L [21%] O_2), standard medium demonstrated increasing oxygen utilization with increases in the nucleoside triphosphate to inorganic phosphate (NTP/P_i) ratio consistent with sustained proliferation (Figure 6.4A, B). To mimic the ischemic microenvironment induced by TAE, cells were subsequently perfused with anoxic, nutrient depleted medium (1 mM glucose, 1% FBS and 0.5 mM glutamine) for six hours followed by hypoxic (0.017 mM/L [1.7%] O_2), nutrient depleted medium. Concurrent measurements of O_2 utilization and cellular bioenergetics through ^{31}Phosphorus NMRS demonstrated a marked reduction in oxygen utilization with an associated reduction in the NTP/P_i ratio. Interestingly, a subsequent small increase in the inlet oxygen concentration resulted in an increase in oxygen utilization and a delayed increase in the NTP/P_i ratio, confirming that the capacity for metabolic activity was maintained after exposure to severe O_2 deprivation (Figure 6.4A, B). DNP-NMRS of hyperpolarized 1-^{13}C-pyruvate enabled the real time assessment of metabolic reprogramming in HCC cells surviving severe ischemia demonstrating a significant reduction in the alanine-to-lactate ratio (Figure 6.4C, D).

To assess the capability of DNP-NMR to leverage this metabolic reprogramming in order to detect latent, treatment-refractory cellular domains *in vivo*, we performed additional experiments using our rat model of autochthonous HCC and TAE. MR imaging demonstrated characteristic features of HCCs in each animal based on the Liver Imaging and Reporting Data System (LI-RADS) that is used to classify liver lesions in the clinic including arterial phase enhancement and washout of this enhancement on delayed phase images (n=3; Figure 6.5A)[22]. As determined using the modified Response Criteria in Solid Tumors (mRECIST) that are commonly applied to determine therapeutic effect in patients following TAE, each treated HCC (n=6) demonstrated imaging features consistent with a complete radiographic response including a decrease in tumor volumes at day 7 and 14, as well as the disappearance of mass-like arterial phase enhancement (APCE) in the target lesion in keeping with a non-viable tumor (n=3, Figure 6.5B, C)[19]. While four of six treated animals demonstrated persistent radiographic findings of non-viability throughout the tumor for 14 days including stable or reduced size and/or the absence of APCE following TAE, peripheral recurrence was observed after day 4 in two animals identified based mRECIST criteria (Figure 6.5C). Interestingly, DNP-NMRS of hyperpolarized 1-^{13}C-pyruvate enabled the detection of viable cellular domains that were undetectable using conventional, contrast-enhanced MR imaging in combination with mRECIST criteria (Figure 6.5C-F). Despite the absence of growth within the tumor and/or detectable APCE, quantitative analysis of spectroscopic images demonstrated reduced, but persistent, delivery of pyruvate and metabolism to alanine and lactate in regions of tumors considered non-viable based on mRECIST criteria (Figure 6.5D-F). Importantly, and consistent with the metabolic reprogramming observed in our *in vitro* studies of HCC cells surviving severe, TAE-like ischemia, these non-viable tumor regions demonstrated a significant reduction in the alanine-to-lactate ratio following embolization when adjusted for pyruvate levels, as indicated by significant reductions in the coefficient for the generalized regression model (Figure 6.5H). In addition, H&E staining of tumors explanted 14 days following TAE demonstrated persistent viability adjacent to regions of necrosis. In tumors regions that were non-viable based on conventional imaging criteria, there was a significant correlation between the levels of intratumoral pyruvate and percent tumor viability at 14 days following embolization (Figure 6.5G, I; rho = 0.95; p = 0.004). In these regions, histologic viability at day 14 was negatively associated with the change in alanine-to-lactate ratio from day 0 to day 14 (Figure 6.5J; rho = -0.83, p = 0.04). These data indicate that persistent perfusion in combination with metabolic reprogramming are required to enable the survival of HCC under TAE-induced ischemia. Together, these radiographic and histologic findings demonstrate the capability of DNP-MRS to leverage metabolic reprogramming in order to overcome the limitations of conventional imaging strategies and detect latent, treatment-refractory cellular domains in HCC following TAE.

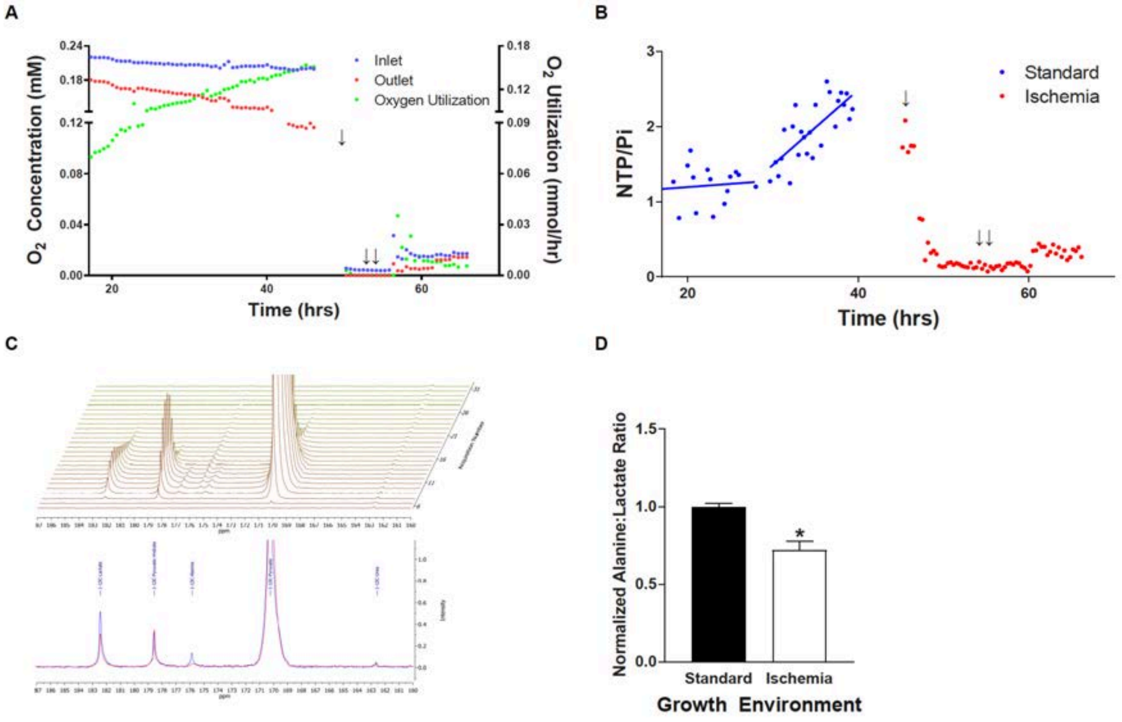

Figure 6.4 DNP-MRS Demonstrates Metabolic Reprogramming in Perfused HCC Cells Surviving Severe Ischemia *In Vitro*. (A, B) HCC cells grown under standard growth conditions demonstrated increasing levels of oxygen utilization and associated nucleoside triphosphate to inorganic phosphate (NTP/P_i) ratios which diminished rapidly when the growth environment is changed to ischemic conditions (anoxia with nutrient depleted medium, single arrow) for 6 hours mimicking TAE. The maintenance of cellular viability under these conditions is underscored by an increase in the oxygen utilization and the NTP/P_i ratio when the oxygen level is increased to 0.017 mM (double arrow). (C, D) DNP-MRS of hyperpolarized 1-^{13}C-pyruvate demonstrates metabolic reprogramming of cells surviving TA(C)E-like ischemia (blue spectrum) with a reduction in the alanine to lactate ratio (n=2 injections per condition; p = 0.023).

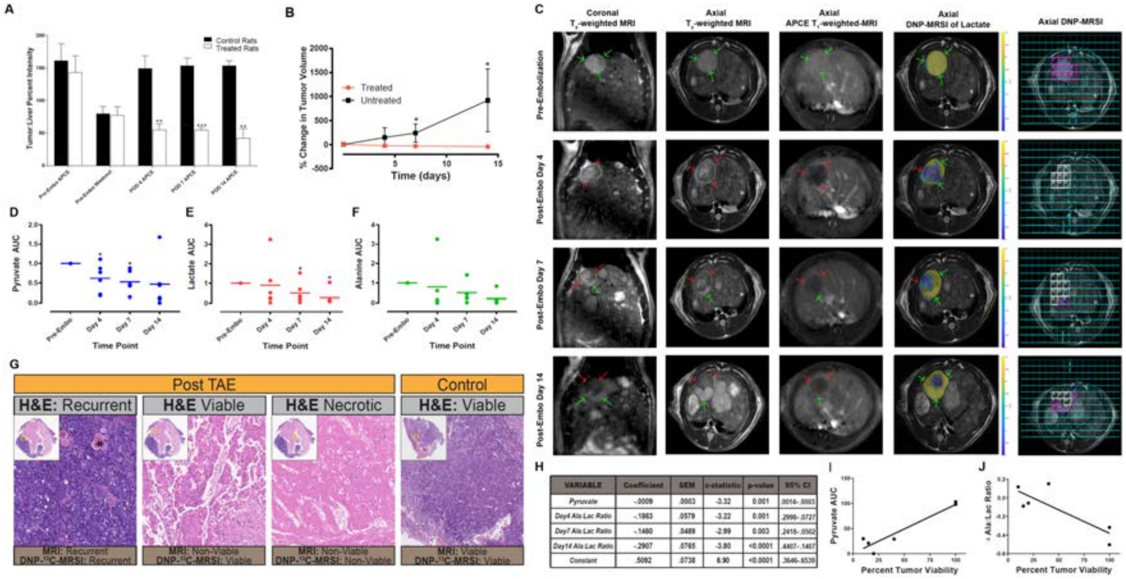
A
Control Rats
Treated Rats
Tumor:Liver Percent Intensity
Pre-Embo APCE
Pre-Embo Washout
POD 4 APCE
POD 7 APCE
POD 14 APCE
B
% Change in Tumor Volume
Treated
Untreated
Time (days)
C
Coronal T2-weighted MRI
Axial T2-weighted MRI
Axial APCE T1-weighted-MRI
Axial DNP-MRSI of Lactate
Axial DNP-MRSI
Pre-Embolization
Post-Embo Day 4
Post-Embo Day 7
Post-Embo Day 14
D
Pyruvate AUC
E
Lactate AUC
F
Alanine AUC
Pre-Embo
Day 4
Day 7
Day 14
Time Point
G
Post TAE
Control
H&E: Recurrent
H&E Viable
H&E Necrotic
H&E: Viable
MRI: Recurrent
DNP-13C-MRSI: Recurrent
MRI: Non-Viable
DNP-13C-MRSI: Viable
MRI: Non-Viable
DNP-13C-MRSI: Non-Viable
MRI: Viable
DNP-13C-MRSI: Viable
H
I
Pyruvate AUC
Percent Tumor Viability
J
Δ Ala:Lac Ratio
Percent Tumor Viability

VARIABLE	Coefficient	SEM	z-statistic	p-value	95% CI
Pyruvate	-.0009	.0003	-3.32	0.001	.0014-.0003
Day4 Ala:Lac Ratio	-.1863	.0579	-3.22	0.001	.2996-.0727
Day7 Ala:Lac Ratio	-.1460	.0489	-2.99	0.003	.2418-.0502
Day14 Ala:Lac Ratio	-.2907	.0765	-3.80	<0.0001	.4407-.1407
Constant	.5092	.0738	6.90	<0.0001	.3646-.6539

Figure 6.5 DNP-MRSI Enables the Detection of Latent HCC Cells Surviving TAE *In Vivo*. (A-C) DEN-induced tumors demonstrate imaging features consistent with the LI-RADS criteria used for image-based diagnosis of HCC in the patients including arterial phase enhancement (APHE) and washout on delayed phase imaging relative to uninvolved liver. Images from a representative animal demonstrate T_2-weighted and post-contrast T_1-weighted imaging features consistent with viable HCC (→ in the top row). Consistent with imaging features observed following a complete response to TAE as assessed using the mRECIST criteria applied to assess treatment response in patients, MR imaging of TAE-treated HCCs demonstrated (i) a >30% reduction in APHE as compared to uninvolved liver (n=3; *p=.001, **p<.0001, ***p=.002) and (ii) a significant reduction in size (n=6; *p=.023, **p=.016). (C) Images from a representative animal demonstrate that while conventional imaging failed to detect viable tumor cells, DNP-MRSI of hyperpolarized 1-^{13}C-pyruvic acid enabled the detection of persistent metabolism at the tumor periphery corresponding to regions of the tumor that appear non-viable on conventional MRI. In these regions reduced levels of pyruvate (D; *p=.046, **p=.028), lactate (E; *p=.046, **p=.046) and alanine (F) were observed. (C,H) At each post-TAE time point, tumor regions considered non-viable (→, NV in final column) using conventional contrast-enhanced MRI demonstrated reduced alanine-to-lactate ratios as evidenced by a reduction in the associated coefficient using a generalized linear model. Interestingly, images from a representative animal demonstrate persistent conversion of pyruvate to lactate on day 4 prior to the development of the development of recurrence on conventional imaging (→, V: Viable voxels, NV: Non-viable voxels). (G) H&E staining of a representative TAE-treated 14 days after embolization demonstrates persistent viability in regions of tumor that are considered non-viable based on mRECIST criteria but exhibit persistent metabolism on DNP-MRSI adjacent to regions of necrosis and recurrent HCC. (I) In the regions of tumor that appeared non-viable on conventional MRI, a linear regression of the percent tumor viability and intra-tumoral pyruvate levels at post-TAE day 14 demonstrates a significant positive correlation (R^2=.90, p=.0041). (J) Linear regression of percent tumor viability and the change in the intra-tumoral alanine-to-lactate ratio 14 days after TAE demonstrates a significant negative correlation (R^2=.69, p=.04).

6.5: Discussion

The presented data demonstrate that latent HCC cells utilized metabolic reprogramming to survive the ischemic conditions induced by TAE, altering expression of glycolytic enzymes to reduce anabolic synthesis and increase lactate production. DNP-^{13}C-MRSI was leveraged to identify these metabolic alterations *in vivo* through quantification of 1-^{13}C-alanine production relative to 1-^{13}C-lactate production following DNP-1-^{13}C-pyruvate administration. This strategy enables the detection of hitherto indiscernible, treatment-refractory cells. These findings address a fundamental deficiency in conventional clinical imaging paradigms for detecting treatment-refractory, latent cellular domains in the poorly perfused microenvironments induced through TAE by applying an innovative approach to the development of imaging biomarkers tailored to the underlying cellular biology.

The integration of the functional measures of metabolism provided by DNP-^{13}C-MRSI in combination with the enhanced glycolytic flux through lactate dehydrogenase in cells surviving severe ischemia overcomes important sensitivity constraints of current imaging paradigms that limit the effectiveness of mRECIST for detecting latent disease. Firstly, these criteria specify a complete imaging response as the absence of residual viable tumor based on the lack of intratumoral contrast enhancement within target lesions on arterial phase imaging (i.e. increased signal due to contrast leaving the arteries and entering the tumor tissue)[23]. However, a minority of lesions undergo complete necrosis and local recurrence of HCC has been shown to be common after a complete imaging response[24]. Indeed, our finding that severe ischemia induces cellular quiescence in surviving HCC cells provides a potential mechanism to explain the clinical phenotype of recurrent disease in the setting of a complete imaging response. Together, these findings indicate that the absence of intratumoral contrast enhancement denotes tissue ischemia with variable necrosis underscoring the limited sensitivity of contrast enhancement on MRI for the detection of tissue-level vascular patency. In each embolized animal, the enhanced sensitivity afforded by DNP-^{13}C-MRSI enabled the detection of intratumoral 1-^{13}C-pyruvate despite the absence of intratumoral arterial-phase contrast enhancement. Secondly, while the intratumoral delivery of 1-^{13}C-pyruvate demonstrates persistent perfusion following TAE, functional imaging biomarkers are required for the direct detection of viable cell populations. As demonstrated by our data, the detection of latent cancer cells represents a unique challenge with respect to sensitivity given their hypometabolic state and limited number. Indeed, HCC cells surviving TAE-like ischemia demonstrated the abrogation of anabolism with an associated reduction in glucose uptake. The shunting of glucose carbons toward lactate provides an opportunity to overcome sensitivity limitations by leveraging this alteration for functional metabolic imaging. DNP-^{13}C-MRSI enabled the direct detection of surviving HCC cells based on their uptake of 1-^{13}C-pyruvate and metabolism to 1-^{13}C-lactate and 1-^{13}C-alanine. The serial measurement of individual metabolites enables the assessment of metabolic flux providing a unique imaging biomarker that is not accessible through other non-invasive imaging modalities and may be integrated with FDG-PET to allow more complete characterization of tumor metabolism[25,26]. Moreover, the positive association of cellular viability following TAE with pyruvate levels as well as the negative association of viability with alanine-to-lactate ratios suggest that DNP-^{13}C-MRSI may be utilized to establish quantitative metrics that predict treatment response and enable interpatient comparisons.

Importantly, the ability to detect treatment-refractory, latent HCC cells following TAE holds important implications for improving outcomes in patients by informing both the timing and type of subsequent therapy. Indeed, optimal therapy with TAE is limited by current imaging measures of residual disease, which fail to guide repeat interventions that can effect a more complete response and mitigate recurrence and/or metastasis. This opportunity is underscored by the fact that a maximal response with TAE is observed following several interventions as well as preclinical data demonstrating that HCC cells surviving TAE-induced ischemia have an increased propensity for invasion and metastasis[27,28]. In addition to improving treatment response through earlier re-treatment, the ability to identify treatment-resistant, latent HCC cells following TAE may overcome limitations of adjunct therapies administered at the time of TAE by informing the selection of these agents. Prospective, randomized trials demonstrate no difference between TAE or TAE in combination with the intra-arterial delivery of chemotherapy (TACE) with respect to survival. These data emphasize the failure of currently administered TACE agents, which include cell-cycle-specific chemotherapeutics targeting proliferating cancer cells, to potentiate the cytotoxicity of embolotherapy-induced ischemia[29–32]. We, and others, have shown that the ischemic microenvironment generated by TAE induces dependencies on metabolic stress responses (MSR) in surviving HCC cells including autophagy[13,33]. These data suggest that the detection of HCC cells surviving poorly perfused, ischemic microenvironments using DNP-^{13}C-MRSI of hyperpolarized 1-^{13}C-pyruvate will enable this constrained phenotype to be leveraged by selecting therapeutics that specifically target MSR dependencies such as autophagy inhibitors[13]. These findings provide the rationale for a phase 1-2 clinical trial studying the application of DNP-^{13}C-MRSI of hyperpolarized 1-^{13}C-pyruvate to assess response to combination therapy using the autophagy inhibitor hydroxychloroquine with TACE for the treatment of unresectable HCC.

Moreover, the described studies applied a translational approach that enhance the likelihood of clinical application. The animal model used for these studies is validated as a translational model of autochthonous HCC and TAE through several publications[13,17,18]. Specifically, the model recapitulates the progression of the human disease wherein patients develop cirrhosis followed by HCC. The TAE procedure precisely mimics the procedure performed in humans including selective embolization of autochthonous tumor feeding vessels. In addition, DNP-^{13}C-MRSI is a clinically relevant technology with established protocols for generating hyperpolarized substrate for injection into animals and humans through a published clinical trial as well as the commercial availability of pre-prepared hyperpolarized 1-13C-pyruvate flow paths[25,34–36]. The concentrations of hyperpolarized 1-13C-pyruvate used for this study match those used for patients. Indeed, the polarization efficiency of clinical hyperpolarizers (~50%) is significantly higher than the preclinical hyperpolarizer used in our studies (~30%) enabling a substantial increase in signal-to-noise. In addition, the scan time required for the acquisition of DNP-^{13}C-MRS images is a fraction of that required for the acquisition of conventional MR images. As such, these images can be acquired in the context of current clinical imaging workflows. In addition, given the fact that the spin-lattice relaxation times are shorter at lower field strengths, the acquisition of hyperpolarized images at field strengths used in the clinic (1.5 and 3.0T) will result in improved image quality due to the longer lifetime of the hyperpolarized spin state.

In summary, the characterization of ischemia-induced metabolic reprogramming in HCC cells enabled the development a DNP-^{13}C-MRS imaging strategy to detect latent, treatment-refractory latent cellular domains following TA(C)E. This approach emphasizes the power of integrating unique aspects of cancer biology with functional imaging technologies to address deficiencies in conventional imaging paradigms.

6.6: Materials and Methods

Cell Lines

Human HCC cell lines were obtained from American Type Culture Collection (HepG2, SNU-449 and SNU-387 Manassas, VA) or Sekisui XenoTech (Huh7, Kansas City, MO). Each cell line was maintained in RPMI medium with 0.3 g/L L-glutamine supplemented with 1.8 g/L D-glucose, 20 mM HEPES, 2 g/L sodium bicarbonate and 10% FBS. Rat hepatocellular carcinoma cells (HR-2) derived from diethylnitrosamine (DEN)-induced HCCs in Wistar rats were a generous gift from Dr. Istvàn Blazsek of Paul Brousse Hospital, Villejuif, France[37]. HR-2 cells were maintained in DMEM medium (DMP52-1LT; Caisson Laboratories, Inc.; Smithfield, UT) supplemented with 3 g/L glucose, 20 mM HEPES, 3.7 g/L Sodium Bicarbonate and 10% FBS. The incubation medium was exchanged for fresh medium every 48 hours.

Cellular Growth Kinetics and Cell Cycle Analyses

1×10^5 cells/6 cm^2 were plated with 3 mL of complete medium on the day prior to the application of experimental conditions. Adherent cells (HepG2, SNU-449, and SNU-387) were incubated under the intended oxygen saturation (O_2) 21%, 3%, 1% O_2 (SNU-449, SNU-387 and SNU-398) or 0.5% O_2 (HepG2) with the relevant medium: (i) standard medium including RPMI 1640 for human HCC cells or DMEM for rat HCC cells supplemented with 10% FBS, 4 mM glutamine and 10 mM glucose or (ii) serum and glucose depleted (SG) medium including RPMI supplemented with 1% FBS and 1mM glucose for human HCC cells or DMEM supplemented with 1% FBS, 1 mM glucose, and 0.5 mM L-glutamine for rat HCC cells. Hypoxic conditions (3%, 1%, 0.5%) were achieved using a HypOxystation H35 (HypOxygen, Frederick, Maryland). The medium in each plate was exchanged daily for fresh medium pre-equilibrated at the relevant oxygen concentration for 24 hours. Cell counting was performed following 24, 72, 120 and 168 hours of incubation (n=3/time point) using a Countess Automated Cell Counter (Life Technologies, Grand Island, NY) as per the manufacturer's instructions. For repletion experiments, cells grown under 1% O_2 with SG medium for 168 hours were subsequently grown under 21% O_2 with standard medium for an additional 168 and cells were similarly counted at 192, 240, 288 and 336 hours following the start of incubation (n=3/time point). Cellular growth kinetics for rat HCC (HR2) cells were similarly measured under standard and ischemic conditions with 2.5 µM of the 737-lactate dehydrogenase (generous gift of Len Neckers, National Cancer Institute).

Cell cycle assays were performed following 48 hour incubations under 21% O_2 with standard medium or 1% O_2 with SG medium as described previously[13]. Cell cycle phase was determined using flow cytometry following cell staining for the nuclear protein Ki-67 and Hoechst dye.

Metabolomic Analyses

Unlabeled Metabolite Profiling: Glucose and lactate concentrations were measured from medium collected during the above-described growth kinetic experiments using a YSI 2950 Biochemistry Analyzer (YSI, Inc., Yellow Springs, Ohio). Cellular glucose uptake was calculated using the MATLAB-based software package, Extracellular Time-Course Analysis (ETA)[38].

Labeled Metabolite Profiling: 4.0 x10^6 HR2 cells were incubated in 15 cm plates under standard conditions and 2.0 x10^6 HR2 cells were incubated in 15 cm plates under ischemic conditions. Following 48-hour incubations, the medium was exchanged for medium containing U-^{13}-C-glucose at the relevant concentration. Following a 4-hour incubation, the medium was removed from the plates and each plate was washed with 1X PBS 3 successive times. The cells were collected by scraping cold perchloric acid (12%). These extracts were then sonicated for 60 seconds of cycles pulsing 3 seconds on, 7 seconds off at an amplitude of 37% using a Fisher Scientific™ Model 120 Sonic Dismembrator (Thermo Fisher Scientific (Waltham, MA) and spun down at 7,500x g at 4°C for 10 minutes in an ultra-centrifuge. The supernatant was then collected and neutralized using KOH to pH 7.0. This solution was then ultra-centrifuged and the supernatant was collected and lyophilized using a FreeZone 2.5L Benchtop Freeze Drying System (Labconco, Kansas City, Missouri). Metabolite levels were then determined by ^{13}Carbon NMR spectroscopy using 400MHz on a Bruker Avance III™ operating at 400 MHz. Prior to spectral acquisition, each lyophilized cell extract was dissolved in 0.300ml of D2O with 0.05% dioxane and the pH was re-adjusted to 7.0. Proton decoupled carbon spectra (Waltz 16) were obtained at 100.62 MHz using a 5mm Bruker BBO probe and the following spectral parameters: 30° flip angle (FA), 1.6s repetition time (TR), 24 kHz spectral width (SW) and 64k data points (TD). After ^{13}Carbon NMR spectroscopy, the solution was diluted to 0.6 ml by adding 0.3 ml of D_2O and a trimethylsilylpropionic acid in D2O external reference standard was introduced into the NMR tube for use as chemical shift reference and quantitation standard. Water suppressed proton spectra were then acquired using the following spectral parameters: FA 45°, TR 8.8s, SW 6775 Hz ad TD 64k. Resonance integrals were quantified using the MestreNova software (Mestrelab Research, Santiago de Compostela, Spain).

Pan Metabolomic Profiling: 3.0 x10^6 HR2 or SNU-387 cells were incubated in 15 cm plates under standard or ischemic conditions for 28 hours with daily medium exchanges. Following 48-hour incubations, the medium was removed from the plates and each plate was washed with 1X PBS 3 successive times. Pan metabolomic analysis was performed on the collected cells and medium with the assistance of Metabolon. Samples were prepared using the automated MicroLab STAR® liquid handling system (Hamilton Co., Reno, NV). Prior to analysis, a cocktail of standards was spiked into every analyzed sample. The resulting extracts were divided into five fractions: two for analysis by two separate reverse phase Reverse Phase/Ultra-High Performance Liquid Chromotography-Tandem Mass Spectrometery ((RP)/UPLC-MS/MS) methods with positive ion mode electrospray ionization (ESI), one for analysis by RP/UPLC-MS with negative ion mode ESI, one for analysis by Hydrophilic Interaction Chromotography (HILIC)/UPLC-MS/MS with negative ion mode ESI, and one sample reserved for backup. All methods utilized a Waters ACQUITY ultra-performance liquid chromatography (UPLC) and a Thermo Scientific Q-Exactive high resolution/accurate mass spectrometer interfaced with a heated electrospray ionization (HESI-II) source and Orbitrap mass analyzer operated at 35,000 mass resolution. The sample extract was dried then reconstituted in solvents compatible to each of the four methods. Each reconstitution solvent contained a series of standards at fixed concentrations to ensure injection and chromatographic consistency. One aliquot was analyzed using acidic positive ion conditions, chromatographically optimized for more hydrophilic compounds. In this method, the extract was gradient eluted from a C18 column (Waters UPLC BEH C18-2.1x100 mm, 1.7 µm) using water and methanol, containing 0.05% perfluoropentanoic acid (PFPA) and 0.1% formic acid (FA). Another aliquot was also analyzed using acidic positive ion conditions; however, it was chromatographically optimized for more hydrophobic compounds. In this method, the extract was gradient eluted from the same afore mentioned C18 column using methanol, acetonitrile, water, 0.05% PFPA and 0.01% FA and was operated at an overall higher organic content. Another aliquot was analyzed using basic negative ion optimized conditions using a separate dedicated C18 column. The basic extracts were gradient eluted from the column using methanol and water, however with 6.5mM Ammonium Bicarbonate at pH 8. The fourth aliquot was analyzed via negative ionization following elution from a HILIC column (Waters UPLC BEH Amide 2.1x150 mm, 1.7 µm) using a gradient consisting of water and acetonitrile with 10mM Ammonium Formate, pH 10.8. The MS analysis alternated between MS and data-dependent MS^n scans using dynamic exclusion. Compounds were identified by comparison to library entries of purified standards or recurrent unknown entities. More than 3300 commercially available purified standard compounds have been acquired and registered on all platforms for determination of their analytical characteristics. Peaks were quantified using area-under-the-curve. For studies spanning multiple days, a data normalization step was performed to correct variation resulting from instrument inter-day tuning differences. Each compound was corrected by registering the medians to equal one (1.00) and normalizing each data point proportionately.

Protein/Proteomic Profiling

Western Blot Analysis: To prepare whole cell extracts, cells were plated the day before at 1-2 x 10^6 cells/ 10 cm^2 and then exposed to standard medium under 21% O_2 or SG medium under 1% (SNU-449, SNU-387 and HR2) or 0.5% (HepG2) for 48 hours with the prescribed medium replaced at 24 hours. Cells were harvested using a cell scraper, lysed in RIPA whole cell lysis buffer and sonicated to affect membrane disruption. Protein quantitation was performed using a BCA Protein Assay Kit (Thermo Fisher Scientific). Anti-GAPDH, Anti-PKM2, Anti-phospho (Tyr105) PKM2, Anti-LDH-A, Anti-phospho (Tyr10) LDH-A, Anti-PC, Anti-β-Actin, Anti-mTOR, Anti-S6, Anti-phospho-S6, Anti-S6 Kinase, Anti-phospho-S6 Kinase, Anti-AMPK-α, and Anti-phospho-AMPK-α were purchased from Cell Signaling Technology Inc. (Danvers, Massachusetts). Anti-P27, Anti-HSP90, and Anti-GPT were purchased from Santa Cruz Biotechnology Inc. (Dallas, Texas). Anti-HIF-1α was purchased from Cayman Chemical (Ann Arbor, Michigan). Gel and blotting materials were purchased from Bio-Rad Laboratories (Hercules, CA). Pierce ECL Western Blotting Substrate from Thermo Fisher Scientific (Waltham, MA) is the chemiluminescent substrate used for immunoblotting detection for exposing x-ray film on a Konica SRX-101A Medical Film Processor (Konica Minolta, Ramsey, NJ).

Labeled Proteomic Profiling: HR2 cells were grown as described above for the labeled metabolic profiling experiments. After 48 hours of growth, the medium was exchanged for medium containing U-C^{13}-Glucose-labelled at the relevant concentration. After 24 additional hours of incubation, the cells were scraped and pelleted with a small sample utilized to acquire cell counts for normalization purposes. Proteins were subsequently extracted from the cell pellets using standard methodologies and eluted protein solutions were then dried and reconstituted with 8M urea. Denaturation/reduction of the sample was performed in 8 M urea/5 mM dithiothreitol/25 mM NH_4HCO_3 (pH 8.0) for over 60 minutes at 52°C. The solution was stored at room temperature in 25 mM iodoacetamide in the dark for 60 min. The urea was diluted to a concentration of 1 M with 25 mM NH_4HCO_3 and then digested with trypsin (1:50 ratio) at 37°C and shaking for 16 hrs. Desalted peptides were analyzed on a Q Exactive Orbitrap Mass Spectrometer (Thermo Scientific) attached to an EasyLC system run at 400 nL/min. Peptides were eluted with a 150 min gradient from 3% to 32% ACN (140 min) and to 90% ACN over 10 min in 0.1% formic acid. Data dependent acquisition mode with a dynamic exclusion of 45 s was enabled. In every 2 s cycle, one full MS scan was collected with scan range of 350 to 1200 *m*/*z*, resolution of 70 K, maximum injection time of 50 ms and AGC of 1e6. Then, a series of MS2 scans were acquired for the most abundant ions from the MS1 scan (top 12). Ions were filtered with charge 2–4. An isolation window of 2.0 *m*/*z* was used with quadruple isolation mode. Ions were fragmented using higher-energy collisional dissociation (HCD) with collision energy of 27%. Orbitrap detection was used with scan range of 200 to 2000 *m*/*z*, resolution of 17.5 K, maximum injection time of 60 ms and AGC of 5e4.

The Uniprot rat database was used for database searching (the version of May 2017 with 35,891 entries). Search parameters were set with the database search engine pFind 3.1 including precursor mass tolerance of 20 ppm, fragment mass tolerance of 20 ppm, trypsin cleavage and up to 3 mis-cleavage. Carbamidomethyl [C] was set as a fixed modification, while Oxidation [M] and 3C(3) [A] were set as variable modifications. The target-decoy approach was used to filter the search results, in which the false discovery rate was less than 1% at the peptide and protein level. Then, the peptides with heavily labeled alanine were used for quantification. The unique peptides with heavy Alanine were obtained with precursor m/z, charge state, retention time, search score, sequence, modification, and protein information. For each heavy Alanine peptide, an isotopic cluster was obtained, including the unlabeled monoisotopic peak (noted as M0), the M+3 peak, and the M+6 peak, the M+9 peak (depending on the number of heavy Alanine). For each RAW file, these peaks were extracted with a close retention time. The area under curve (AUC) for each peak was calculated. The isotopic influence of the former peak on the later peak (i.e. M0 on M+3, M+3 on M+6, and M+6 on M+9) was subtracted. Finally, the sum of M+3 AUC, M+6 AUC, and M+9 AUC divided by total AUC (M0, M+3, M+6, M+9) was calculated as the C13/(C13+C12) ratio or relative distribution.

Immunohistochemistry

After deparaffinization and rehydration of 4-μm-thick tissue sections, heat induced epitope retrieval was performed in 10 mM sodium citrate buffer (pH 6.0) using a pressure cooker for 20 min. The slides were then blocked for 30 min in StartingBlock™ T20. Anti-PCNA (Abcam, ab29, 1:1000) and anti- HIF-1α (Abcam, ab2185, 1:650) primary antibodies diluted in 5% bovine serum albumin diluted in PBS with 0.2% Triton-X were incubated with sections overnight at 4°C. Secondary antibodies of the appropriate species conjugated to Alexa fluorophores (488, 568, ThermoFisher) were then applied for 30 min at room temperature together with DAPI (300 nM) to label cell nuclei. Slides were then coversliped using ProLong Diamond Antifade aqueous mounting medium (ThermoFisher) and imaged using a Nikon E600 microscope with Stereoinvestigator software (MicroBrightField).

Analysis of immunofluorescence images was performed using Keyence Analysis (Osaka, Japan) software. Briefly, at least 4 different regions of viable tumor were outlined within each tissue section. The number of DAPI+ and/or PCNA+ nuclei in each region were quantified. For HIF-1α staining, the mean fluorescence intensity of these regions was measured using Keyence Hybrid Cell Count Software. The percentage of DAPI+ nuclei that were also PCNA+ was calculated within each region, and the resulting proliferation index as well as the mean HIF-1α fluorescence intensity per DAPI+ nucleus (N=3/group).

Autochthonous rat model of HCC and TAE

Animal studies were conducted according to institutionally approved protocols for the safe and humane treatment of animals. Autochthonous HCCs were induced in male Wistar rats using an established protocol including ad libitum oral intake of 0.01% diethylnitrosamine (DEN) for 12 weeks[16]. Rats with tumors 0.5-1.0 cm in maximal diameter on T_2-weighted MRI were selected for treatment. Using fluoroscopic guidance, segmental catheterization and embolization with 0.1 mL of 40–120 µm Embosphere particles (Merit Medical, South Jordan, Utah) diluted in 0.1 mL iopamidol contrast medium (Isovue 370; Bracco, Monroe Township, New Jersey) was performed as previously described previously[16]. Pre- and post-embolization arteriography was performed using an AngioStar Plus Imaging System (Siemens, Malvern, Pennsylvania).

Dynamic Nuclear Polarization ^{13}Carbon Magnetic Resonance Spectroscopy and Spectroscopic Imaging

DNP of 1-^{13}C-pyruvate: Dynamic Nuclear Polarization of 1-^{13}C-pyruvate was performed using a HyperSense DNP polarizer (Oxford Instruments, Abingdon, UK) at an excitation frequency of 94.080 GHz and temperature of ~1.4 K. DNP was performed on a stock mixture of 14 M [1-^{13}C]-pyruvate (Cambridge Isotopes; Tewksbury, MA), 15 mM OX063 radical (GE Healthcare, Chicago, IL) and 1.5 mM of Dotarem (Guerbet LLC, Princeton, NJ). 22 µL of stock solution were melted in 4 mL or 8 mL of dissolution buffer (80 mM NaOH, 40 mM Trizma (pH = 7.6), 50 mM NaCl and 0.42 mM EDTA), for *in vivo* or *in vitro* experiments for *in vivo* or *in vitro* experiments respectively, at 10-bar pressure and 180 °C to yield 80 mM isotonic neutral hyperpolarized 1-^{13}C-pyruvate. For *in vitro experiments*, 6.3 mL of hyperpolarized 1-^{13}C-pyruvate was pumped into the cell mass at 7 mL/min. For *in vivo* studies, 6.7 mL/kg of the sample was administered through a tail vein catheter over 13 seconds by hand injection, followed by a 300-µL saline administration over 2 seconds to flush the pyruvate from the catheter's dead volume.

MRS: MR spectroscopy was performed on perfused HR-2 cells inside an Oxford 9.4 Tesla, 8.9 cm bore magnet interfaced to an Agilent Direct Drive Console (Wilmington, DE). The cell perfusion apparatus used to perfuse cells inside the NMR spectrometer was similar to that described previously with modifications to maintain carefully controlled hypoxic conditions and the injection of hypoxic hyperpolarized substrates[39]. These modifications included the design of a radial flow bioreactor as well as the addition of the Oxycyte perfluorocarbon (5%, Aurum Biosciences, Glasgow, UK) to the perfusion medium for ischemic conditions. The NMR tube contained a packed bed of microcarriers that was continuously perfused with cell culture medium. In-line polarographic oxygen probes (Mettler-Toledo, Columbus, OH) were used at the inlet and outlet of the NMR tube. A 20-mm broadband liquids probe was used to acquire ^{31}P and ^{13}C spectra (Doty Scientific: Columbia, SC). For ^{31}P spectra, 60° pulses were used with a repetition time of 1000 ms. For ^{13}C NMR, spectra were acquired with 12° pulses to limit radiofrequency-induced relaxation of the hyperpolarized spin state, a repetition time of 3 s, 8192 points, and a spectral width of 25000 Hz. WALTZ-16 decoupling was used during signal acquisition to improve spectral resolution. Resonance intensities were determined with MestreNova NMR software.

MRI and MRSI: MR images were acquired using an Agilent 4.7T, 40 cm horizontal bore MR Spectrometer with a 25 gauss/cm gradient tube interfaced to an Agilent DirectDrive console. Each animal was positioned within a Polarean proton-tuned (200.1 MHz) birdcage resonator with quadrature polarization with a Polarean ^{13}Carbon-tuned (50.525 MHz) surface coil positioned over the right upper quadrant (Polarean: Durham, NC). T_2-weighted MRI (FOV: 70 mm x 70 mm, Grid size: 256 x 256, Slice thickness: 2 mm, TR minimum: 1.4 s (respiratory gated), TE: 59.1 ms, Averages: 8), T_1-weighted pre- and post-contrast MRI (FOV: 70 mm x 70 mm, Grid size: 256 x 256, Slice thickness: 2 mm, TR: 250 ms, TE: 4.596, α=80°, Averages: 8), Contrast- Enhanced MRI (FOV: 50 mm x 50 mm, Grid size: 96 x 96, Slice thickness: 5 mm, TR: 10.184 ms, TE: 2.564 ms, α=80°, Averages: 1, Images acquired in series: 96), were then performed. Contrast-enhanced MRI required the bolus administration of 0.3 mL gadolinium contrast material (MultiHance; Bracco, Monroe Township, New Jersey) mixed in 0.7 mL saline via tail vein catheterization and was always performed after DNP-^{13}C-MRSI. DNP-^{13}C-MRSI was acquired using a 2D (slab thickness = 10 mm) echoplanar spectroscopic imaging (EPSI) sequence using a spectral bandwidth of 1.1kHz with 128 points, enabling detection of chemical shifts of 22 ppm [40]. The FOV was 60 mm x 45 mm with 12 phase encode steps and 16 frequency encode steps, enabling an in-plane resolution of 3.75 mm x 3.75 mm. This sequence required ~2 s to complete and was repeated every ~4 s for a minimum of 10 scans per study. Image acquisition was initiated 25 s following the commencement of the injection to maximize observed lactate.

Acquired proton images and EPSI spectra were reconstructed in MATLAB 2018B (Mathworks, Inc.). MR images were interpreted by a board-certified radiologist (TPG) with more than 10 years of experience using established Liver Imaging and Reporting Data System (LI-RADS) criteria in order to provide a diagnosis for each identified liver lesion [22]. Treated response was assessed modified Response Evaluation Criteria in Solid Tumors to identify regions of viable and non-viable tumor[19]. Carbon voxels corresponding to tumor voxels were identified based upon the overlay of the 12x16 grid upon the T2-weighted images.

To ensure accurate quantitation of the carbon data for longitudinal comparisons, several corrections to the raw signal were required consistent with the analysis of spectroscopic data: (i) B_1 correction, (ii) point spread function correction, (iii) polarization efficiency correction, (iv) baseline subtraction, and (v) normalization to a known standard. These corrections are discussed at length in Chapter 5 of this dissertation. T1 correction of this data was not performed given the experimental observation of similar T1 decay of pyruvate, lactate, and alanine in serum.

To generate metabolite maps, integrals of pyruvate (δ**:** 170.4**)**, lactate (δ**:** 183.35**)**, and alanine (δ**:** 176.5**)** were utilized. For kinetic analyses the spectra from tumor voxels were summed for each of 10 images in a study. Absolute metabolite amounts were quantified by integrating pyruvate, lactate, and alanine peaks fitted to a Lorentzian line shape [41]. To reduce bias introduced from poor fits, an in-house algorithm was developed to qualify metabolite quantifications as: either (A) detectable (observable peak, non-representative fit), (B) quantifiable (observable peak, representative fit), or (C) non-detectable (non-observable peak). A receiver operating curve was utilized to identify optimal r^2 and peak-height thresholds for distinguishing these categories. This analyses determined that the optimal threshold for detection was an $r^2 > 0.44$ and a raw peak height >1.46X the root-mean square of the baseline signal. Metabolites were deemed quantifiable if they met the standard for detection and the raw peak height was >2.64X the root-mean square of the baseline signal. If neither of these criteria were met, a metabolite signal was deemed non-detectable. For AUC and ratio analyses, data that was integrals of non-detectable metabolites were replaced with zeros and those of detectable, non-quantifiable metabolites were replaced with NaNs.

Histology

Treated and untreated tumors were harvested from rats following CO_2 euthanasia using institutionally approved protocols. Tissues were subsequently formalin fixed for staining and the percentage of viable HCC was estimated from hematoxylin and eosin (H&E) stained sections by a hepatobiliary pathologist with extensive experience in HCC (EEF).

Statistical analyses

Statistical analyses were performed with the use of GraphPad Prism version 6.02 (GraphPad Software, San Diego, CA), R 3.4.4, and STATA 15. Tumor viability is reported as the average percent viability of all targeted tumors on H&E stained histologic sections.

Mean values are reported as mean ± SD of the mean. Data were analyzed using the Shapiro-Wilk test for normality. For normally distributed data, two-tailed *t* test was performed to assess the statistical significance of differences in mean values. For the case of individual metabolite levels before and after embolization, data were not normally distributed, and the Wilcoxon signed rank test was used to compare metabolite measures between time points. Quasi-least squares (QLS) regression was used to model the alanine-to-lactate ratio over time adjusted for pyruvate. The regression models were implemented using the xtqls function in STATA 15.0. QLS is an alternative method for estimating the correlation parameters within the framework of the generalized estimating equation (GEE) approach. It allows for implementation of the autoregressive correlation structure among repeated measures that are unequally spaced in time.

6.7: Supplementary Figures

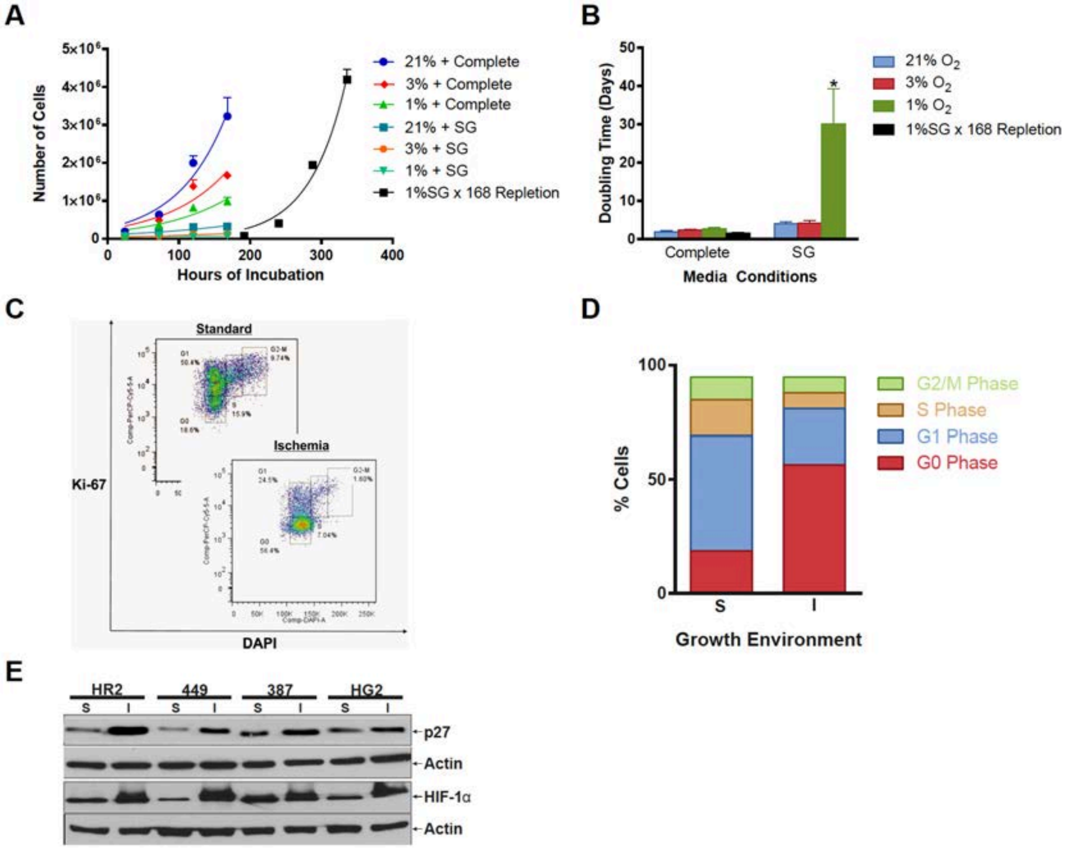

Figure 6.S1 Post-TACE Ischemia Induces Growth Latency *In Vitro*. (A, B) HR2 cells grown under standard conditions (21% O_2 and standard medium), moderate and severe hypoxia (3% O_2 and 1% O_2 with standard medium), nutrient-limited conditions (21% O_2 and SG medium), and moderate ischemia (3% O_2 and SG medium) all demonstrated persistent growth. Cells grown under severe ischemia (1% O_2 and SG medium) demonstrated no growth with a linear regression demonstrating a slope that was not significantly different than zero. The median estimated doubling time (30.1 ± 5.2 days) is included for the purpose of comparison (*p=.03). Cells initially grown under severe ischemia (1% O_2 + SG) for 1 week followed by standard conditions for an additional week (1% SG x 168 hr repletion) demonstrated a period of latency followed by persistent growth. (C) Representative FACS plot of HR2 cells stained with DAPI and a fluorescent antibody to Ki-67 nuclear antigen demonstrating a significant increase in the percentage of cells in the G0 phase and a decrease in the percentage of cells in the S phase of the cell cycle for cells incubated under severe ischemia as compared to cells incubated under standard conditions (G0 phase: 55.5 ± 1.8% vs. 18.2 ± 0.6%, p<.0001; S phase: 8.4 ± 1.8% vs. 18.3 ± 0.6%, p=.001, respectively). (D) Analysis of flow cytometry data demonstrates an increase in the proportion of G0 phase cells and a decrease in the proportion of S phase cells following incubations under standard [S] versus severely ischemic [I] growth conditions. (E) Western blots of lysates from rat (HR2) and human (SNU-449, SNU-387, HG2) cells confirmed the induction of quiescence and a metabolic stress response based on the increased expression of $p27^{kip1}$ as well as increased stabilization of HIF-1α for cells surviving severe ischemia [I] as compared to cells incubated under standard conditions [S] consistent with *in vivo* data.

6.8: References

1. Perkons, N. R. *et al.* Hyperpolarized Metabolic Imaging Detects Latent Hepatocellular Carcinoma Domains Surviving Locoregional Therapy. *Hepatology* (2019). doi:10.1002/HEP.30970
2. Stegmeier, F., Warmuth, M., Sellers, W. R. & Dorsch, M. Targeted cancer therapies in the twenty-first century: lessons from imatinib. *Clin. Pharmacol. Ther.* **87**, 543–552 (2010).
3. Pfitzenmaier, J. *et al.* Telomerase activity in disseminated prostate cancer cells. *BJU Int.* **97**, 1309–1313 (2006).
4. Karrison, T. G., Ferguson, D. J. & Meier, P. Dormancy of mammary carcinoma after mastectomy. *J. Natl. Cancer Inst.* **91**, 80–85 (1999).
5. Aguirre-Ghiso, J. A. Models, mechanisms and clinical evidence for cancer dormancy. *Nat. Rev. Cancer* **7**, 834–846 (2007).
6. Desar, I. M. E. *et al.* Beyond RECIST: Molecular and functional imaging techniques for evaluation of response to targeted therapy. *Cancer Treat. Rev.* **35**, 309–321 (2009).
7. Forner, A. *et al.* Evaluation of tumor response after locoregional therapies in hepatocellular carcinoma: Are response evaluation criteria in solid tumors reliable? *Cancer* **115**, 616–623 (2009).
8. Shah, S. a. *et al.* Underutilization of therapy for hepatocellular carcinoma in the medicare population. *Cancer* **117**, 1019–1026 (2011).
9. Higuchi, T., Kikuchi, M. & Okazaki, M. Hepatocellular Carcinoma after Transcatheter Hepatic Arterial Embolization: A Histopathologic Study of 84 Resected Cases. *Cancer* **73**, 2259–2267 (1994).
10. Monsky, W. L. *et al.* Semiautomated segmentation for volumetric analysis of intratumoral ethiodol uptake and subsequent tumor necrosis after chemoembolization. *Am. J. Roentgenol.* **195**, 1220–1230 (2010).
11. Kim, S. *et al.* Hepatocellular Carcinoma: Assessment of Response to Transarterial Chemoembolization With Image Subtraction. *Analysis* **31**, 348–355 (2010).
12. Kamel, I. R. *et al.* Role of Diffusion-Weighted Imaging in Estimating Tumor Necrosis After Chemoembolization of Hepatocellular Carcinoma. *Am. J. Radiol.* **181**, 708–710 (2003).
13. Gade, T. P. F. *et al.* Ischemia Induces Quiescence and Autophagy Dependence in Hepatocellular Carcinoma. *Radiology* (2017). doi:10.1148/radiol.2017160728
14. Pantel, A. R., Ackerman, D., Lee, S. C., Mankoff, D. A. & Gade, T. P. F. Imaging Cancer Metabolism: Underlying Biology and Emerging Strategies. *J. Nucl. Med.* **59**, 1340–1349 (2018).
15. Chen, R., Li, J., Zhou, X., Liu, J. & Huang, G. Fructose-1,6-bisphosphatase 1 reduces 18F FDG uptake in hepatocellular carcinoma. *Radiology* **284**, 844–853 (2017).
16. Ardenkjær-Larsen, J. H. *et al.* Increase in signal-to-noise ratio of >10,000 times in liquid-state NMR. *Proc. Natl. Acad. Sci.* **100**, 10158–10163 (2003).
17. Gade, T. P. F. F. *et al.* Segmental Transarterial Embolization in a Translational Rat Model of Hepatocellular Carcinoma. *J. Vasc. Interv. Radiol.* **26**, 1229–1237 (2015).
18. Kiefer, R. M. *et al.* Relative Initial Weight Is Associated with Improved Survival without Altering Tumor Latency in a Translational Rat Model of Diethylnitrosamine-Induced Hepatocellular Carcinoma and Transarterial Embolization. *J. Vasc. Interv. Radiol.* **28**, 1043–1050 (2017).

19. Lencioni, R. & Llovet, J. M. Modified RECIST (mRECIST) assessment for hepatocellular carcinoma. *Semin. Liver Dis.* **30**, 52–60 (2010).
20. Rai, G. *et al.* Discovery and Optimization of Potent, Cell-Active Pyrazole-Based Inhibitors of Lactate Dehydrogenase (LDH). *J. Med. Chem.* **60**, 9184–9204 (2017).
21. Yeung, C. *et al.* Targeting Glycolysis through Inhibition of Lactate Dehydrogenase Impairs Tumor Growth in Preclinical Models of Ewing Sarcoma. *Cancer Res.* **79**, 5060–5073 (2019).
22. Mitchell, D. G., Bruix, J., Sherman, M. & Sirlin, C. B. LI-RADS (Liver Imaging Reporting and Data System): Summary, discussion, and consensus of the LI-RADS Management Working Group and future directions. *Hepatology* **61**, 1056–1065 (2015).
23. Llovet, J. M. *et al.* Design and endpoints of clinical trials in hepatocellular carcinoma. *J. Natl. Cancer Inst.* **100**, 698–711 (2008).
24. Jin, Y.-J. *et al.* Predisposing factors of hepatocellular carcinoma recurrence following complete remission in response to transarterial chemoembolization. *Dig. Dis. Sci.* **58**, 1758–65 (2013).
25. Day, S. E. *et al.* Detecting tumor response to treatment using hyperpolarized 13C magnetic resonance imaging and spectroscopy. *Nat. Med.* **13**, 1382–1387 (2007).
26. Gutte, H. *et al.* Simultaneous hyperpolarized 13C-pyruvate MRI and 18F-FDG-PET (HyperPET) in 10 canine cancer patients. *J. Nucl. Med.* **56**, 1786–92 (2015).
27. Liu, L. *et al.* Influence of hepatic artery occlusion on tumor growth and metastatic potential in a human orthotopic hepatoma nude mouse model: relevance of epithelial-mesenchymal transition. *Cancer Sci.* **101**, 120–8 (2010).
28. Farinati, F. *et al.* Unresectable hepatocellular carcinoma in cirrhosis: survival, prognostic factors, and unexpected side effects after transcatheter arterial chemoembolization. *Dig. Dis. Sci.* **41**, 2332–9 (1996).
29. Kawai, S. *et al.* Prospective and randomized clinical trial for the treatment of hepatocellular carcinoma--a comparison of lipiodol-transcatheter arterial embolization with and without adriamycin (first cooperative study). The Cooperative Study Group for Liver Cancer Treat. *Cancer Chemother. Pharmacol.* **31**, S1-6 (1992).
30. Llovet, J. M. *et al.* Arterial embolisation or chemoembolisation versus symptomatic treatment in patients with unresectable hepatocellular carcinoma: a randomised controlled trial. *Lancet* **359**, 1734–9 (2002).
31. Chang, J. M., Tzeng, W. S., Pan, H. B., Yang, C. F. & Lai, K. H. Transcatheter arterial embolization with or without cisplatin treatment of hepatocellular carcinoma. A randomized controlled study. *Cancer* **74**, 2449–53 (1994).
32. Marelli, L. *et al.* Transarterial therapy for hepatocellular carcinoma: which technique is more effective? A systematic review of cohort and randomized studies. *Cardiovasc. Intervent. Radiol.* **30**, 6–25 (2007).
33. Gao, L. *et al.* Chloroquine promotes the anticancer effect of TACE in a rabbit VX2 liver tumor model. *Int. J. Biol. Sci.* **9**, 322–30 (2013).
34. Nelson, S. J. *et al.* Metabolic imaging of patients with prostate cancer using hyperpolarized [1-^{13}C]Pyruvate. *Sci. Transl. Med.* **5**, 1–10 (2013).
35. Bohndiek, S. E. *et al.* Detection of tumor response to a vascular disrupting agent by hyperpolarized 13C magnetic resonance spectroscopy. *Mol. Cancer Ther.* **9**, 3278–88 (2010).
36. Keshari, K. R. & Wilson, D. M. Chemistry and biochemistry of 13C hyperpolarized magnetic resonance using dynamic nuclear polarization. *Chem. Soc. Rev.* **43**,

(2014).
37. Thièry, J. P. *et al.* Hepatocellular carcinoma cell lines from diethylnitrosamine phenobarbital-treated rats. Characterization and sensitivity to endothall, a protein serine/threonine phosphatase-2A inhibitor. *Hepatology* **29**, 1406–1417 (1999).
38. Murphy, T. a. & Young, J. D. ETA: Robust software for determination of cell specific rates from extracellular time courses. *Biotechnol. Bioeng.* **110**, 1748–1758 (2013).
39. Mancuso, a *et al.* Real-time detection of 13C NMR labeling kinetics in perfused EMT6 mouse mammary tumor cells and betaHC9 mouse insulinomas. *Biotechnol. Bioeng.* **87**, 835–48 (2004).
40. Basic Practical NMR Concepts : A Guide for the Modern Laboratory. *Max T. Rogers NMR Facility* 1–41 (2013).
41. Wells, J. lorentzfit. *MATLAB Central File Exchange* (2015).

Chapter 7: Conclusions & Future Investigations

7.1: Conclusions

This work demonstrates the utility of dynamic nuclear polarization (DNP) ^{13}C magnetic resonance spectroscopic imaging (MRSI) as a tool for functional molecular imaging *in vivo*. The described experiments were guided by the fundamental hypothesis that the capability of DNP-^{13}C-MRSI to quantify metabolic variation non-invasively provides unique insights into cancer biology. Genetic screening proved to be a powerful, unbiased technique for probe selection. CRISPR-Cas9 functional genetic screens identified enzymatic dependencies of 17 unique cancer types that can be directly imaged using existing DNP-^{13}C probes, while also suggesting potential novel probes in 4 additional cancer types. Follow-up screening in hepatocellular carcinoma (HCC) cell lines, including one derived directly from a patient biopsy, confirmed that lactate dehydrogenase (LDH) is a specific vulnerability of HCC. These findings suggest that MRSI assessment of DNP-[1-^{13}C]-pyruvate metabolism facilitates HCC evaluation *in vivo*. Indeed, DNP-^{13}C-MRSI enabled direct quantification of intratumoral LDH activity that predicted therapeutic response to LDH inhibition, which slowed tumor growth in a rodent model. This highlights DNP-^{13}C-MRSI's unique capacity to quantify drug pharmacodynamics and pharmacokinetics directly. Additional studies in HCC with DNP-[1-^{13}C]-pyruvate demonstrated that persistent metabolism after locoregional treatment of HCC is a more sensitive readout of viability than conventional standard-of-care imaging. In pursuit of clinical translation, key assumptions and limitations were tested experimentally, and the analysis pipeline was discussed extensively.

In sum, this thesis outlines a high-throughput and translatable approach to mobilize existing DNP-^{13}C probes, and potentially identify novel targets, by leveraging target biology to guide probe selection. The examples provided demonstrate the importance of LDH in HCC, underscoring the utility of DNP-[1-^{13}C]-pyruvate for evaluation of response to systemic and locoregional therapy. Beyond the presented applications in HCC, this work provides a foundation for a novel functional molecular imaging paradigm to assess metabolic variation in cancer.

7.2: Future Investigations

Investigation of DNP as a tool to study cell state

Ongoing and recently completed CRISPR-Cas9 screens with the discussed DNP focused library seek to elucidate the utility of DNP-^{13}C-MRSI to distinguish cell populations on the basis of their growth phenotype. To date, these screens have been performed by varying nutrient and oxygen availability to simulate variations in extracellular growth environments. These early investigations have identified that glutaminase and several NADPH-dependent reductases are differentially essential under low nutrient and low oxygen growth conditions, suggesting a potential role for DNP-[1-^{13}C]-dehydroascorbate, DNP-[1-^{13}C] glutamine or DNP-[1-^{13}C]-gluconolactone to distinguish nutrient abundant from nutrient deplete growth environments. Future work will further examine this potential relationship with *in vitro* and *in vivo* models of nutrient and oxygen depletion in HCC.

Standardization and synchronization of DNP experiments

With the assistance of a 3D printer and an Arduino microcontroller, ongoing efforts seek to automate control of all elements of DNP-MRSI experiments. The Arduino currently coordinates and standardizes delivery of the substrate to the subject in the spectrometer through a high-pressure liquid chromatography pump. Future work will enable this microcontroller to detect dissolution completion and initiate acquisitions on the spectrometer(s) thereby enhancing the robustness of planned experiments.

Development of a high-throughput pipeline for testing DNP-^{13}C probes

Current efforts in the lab have led to the development of a molecular simulation tool that estimates a nucleus' T_1 relaxation time. Moving forward this tool will be used to evaluate the polarizability of potential DNP-^{13}C probes *in silico* before attempting chemical synthesis and polarization. Substrates that are successfully polarized will be tested in a perfusion apparatus designed to assess the sensitivity of MRSI to metabolic variation in the cell type or state under study.

Investigating DNP-[1-^{13}C]-pyruvate as a tool to monitor response to TAE in HCC

As a follow-up to the findings in Chapter 6, a clinical trial has been planned to evaluate the capacity of DNP-[1-^{13}C]-pyruvate metabolism to detect persistent viability and tumor recurrence in human patients who have undergone transarterial embolization (TAE).

Implementation of an analogous approach with positron emission tomography

Future work will include implementation of a similar approach to guide selection of positron emission tomography probes in addition to, and in conjunction with, DNP-^{13}C probes.

Appendix 1: Electrolytic ablation enables cancer cell targeting through pH modulation

A1.1: Introduction

This chapter is principally adopted from an article by Perkons et al. in *Communications Biology* that was published in 2018 entitled “Electrolytic ablation enables cancer cell targeting through pH modulation,” outlining the mechanism of electrolytic ablation as a locoregional therapy for solid tumors[1]. This initial work served as the motivation for a subsequent manuscript by Stein, Perkons et al. published in 2020 demonstrating that the progress of electrolytic ablation could be monitored with magnetic resonance[2].

A1.2: Abstract

Minimally invasive ablation strategies enable locoregional treatment of tumors. Electrolytic ablation functions through the local delivery of direct current, without thermal effects, facilitating enhanced precision. However, the clinical application of electrolytic ablation is limited by an incompletely characterized mechanism of action. Here we show that acid and base production at the electrodes precipitates local pH changes causing the rapid cell death that underlies macroscopic tumor necrosis at pH > 10.6 or < 4.8. The extent of cell death can be modulated by altering the local buffering capacity and antioxidant availability. These data demonstrate that electrolytic ablation is distinguished from other ablation strategies via its ability to induce cellular necrosis by directly altering the tumor microenvironment. These findings may enable further development of electrolytic ablation as a curative therapy for primary, early stage tumors.

A1.3: Introduction

Tissue ablation—a technique used to destroy pathological tissues—is one of several locoregional treatments used in the management of a variety of cancers, most commonly hepatocellular carcinoma (HCC). Ablation is distinguished among locoregional therapies by its capability to effect a cure for solitary, primary lesions[3,4]. Ablation modalities can be classified by their primary mechanism of action, which includes thermal-dependent and thermal-independent modalities. Thermal-dependent modalities include radiofrequency ablation, microwave ablation, laser interstitial therapy, high-intensity focused ultrasound, and cryoablation. The most commonly utilized thermal-independent modality for tissue ablation is irreversible electroporation (IRE)[3,5,6]. Choice of modality in the clinic is primarily determined by the site of a lesion and the desired mechanism of cellular injury[7].

Among the thermal-dependent modalities, the majority (radiofrequency ablation, microwave ablation, laser interstitial therapy, and high-intensity focused ultrasound) deposit energy, which causes hyperthermia and subsequent cell death through two mechanisms—direct and indirect injury. Direct injury describes the nearly immediate effect of locoregional heat application at or above 60°C. Indirect injury describes the disruption of normal cellular processes, leading to delayed cell death[6]. At temperatures above 42°C, cell injury occurs more frequently in tumor cells than healthy cells with higher temperatures significantly increasing this therapeutic ratio and decreasing the requisite ablation times[8]. Analogous to the temperature dependence of hyperthermic ablation modalities, cryoablation relies upon cooling tissue below -40°C to induce cell death[5,6]. At temperatures below freezing, ice forms in either the intracellular or extracellular space, inducing osmotic gradients that damage the integrity of the cellular membrane[5,9].

While an understanding of their mechanisms has led to the clinical application of these technologies for locoregional cancer therapy, their efficacy has been mitigated by important intrinsic limitations of thermal ablation. The primary limitation of thermal ablation is poor precision in defining the zone of ablation. Vessels traversing an ablation zone serve as heat sinks or sources, which can distort the temperature gradients within the ablation zone and lead to undesirable treatment margins[5,6]. This imprecision, in combination with safety considerations stemming from off-target toxicity, emphasizes the importance of developing non-thermal ablation strategies to treat cancer.

In comparison to thermal-dependent modalities, IRE kills cancer cells by disrupting membrane integrity[10,11]. IRE applies microsecond pulses of high electric potential (up to 3000 V) between two or more electrodes[5]. While the tendency for heat to be generated scales with the amplitude of the voltage applied, IRE does not mechanistically depend upon hyperthermia to cause cell death[10]. It is believed that this cell death instead proceeds from the induced transmembrane potential which irreversibly disrupts the integrity of the lipid bilayer; specifically, a potential of 1-2 V across a cell membrane is required for cell death to occur[12–15]. A distinct benefit of this technique is that the extracellular matrix remains mostly intact. The primary drawbacks of IRE are secondary side effects associated with the high magnitude of applied voltages. The voltages of the delivered pulses have the potential to induce cardiac arrhythmias and muscle contractions, which necessitate the use of general anesthesia[5,16]. Further, precise electrode alignment is required to ensure adequate charge deposition and to mitigate thermal injury to non-target tissues[5,16,17].

Electrochemotherapy and gene electrotransfer are techniques that are related to IRE but are distinguished by their use of either fewer electrical pulses or lower voltage magnitudes, respectively. These modalities induce a temporary and sublethal permeabilization of cell membranes that facilitates delivery of cargo to cells. Electrochemotherapy is used in cancer therapy to enhance uptake of chemotherapeutic agents, such as bleomycin or cisplatin. Gene electrotransfer is analogous to electrochemotherapy, but instead facilitates the delivery of a gene or genes to cells to enable the downstream production of a therapeutic protein[18–20]. While these techniques demonstrate similar limitations to those seen with IRE, their utility issues from their selectivity and well-characterized mechanisms of action.

Electrolytic ablation, also known as electrochemical treatment, causes necrosis through the application of a direct current between multiple electrodes at relatively low electric potentials compared to IRE, often less than 50 V. In so doing, this technique offers unique advantages compared to other ablation methods[21]. Specifically, electrolytic ablation may permit the creation of precisely defined, shapeable ablation zones, uninfluenced by heat sink effects, which can be monitored and adjusted in real-time using magnetic resonance imaging (MRI)[22–25]. Electrolytic ablation has been utilized for the treatment of a variety of human malignancies; however, its development has been limited by uncertainty regarding the underlying mechanism of the induced cell death[21,26–28]. While it is well established that electrolytic ablation induces electrolysis, a variety of potential mechanisms have been identified that may underlie the observed cell death. These include deposition of electric charge, the creation of a cellular transmembrane potential, production of toxic substances, extraction of water through electroosmosis, and alteration of microenvironmental pH[29–40]. Mechanistic understanding of the cell death induced by electrolytic ablation is required to enable its further development for widespread clinical application. Furthermore, understanding cellular changes induced by electrolytic ablation will enhance parameter selection for related electrochemical therapies, including IRE, electrochemotherapy, and gene electrotransfer, which may have synergistic effects when combined with electrolytic ablation[41,42].

In this study, we endeavored to define the mechanism by which electrolytic ablation causes cell death using an *in vitro* cell-encapsulation assay. After embedding living HCC cells in low melting temperature agarose, electrolytic ablation was performed, and patterns of cell death were measured. We demonstrate that following sustained exposure to a low amplitude direct current, cell death from electrolytic ablation proceeds primarily via a pH-dependent mechanism. Importantly, temperature change and transmembrane voltage gradient did not explain cell death, confirming a non-thermal ablation mechanism that is distinct from IRE. These findings confirm earlier *in vitro* and *in silico* observations of pH changes following electrolysis during electrolytic ablation and gene electrotransfer[39,42,43]. These findings hold important implications for the development of electrolytic ablation as an alternative to existing ablation strategies.

A1.4: Results

In vitro assay development

To evaluate the mechanism of cell death in electrolytic ablation, we developed an *in vitro* cell encapsulation assay in which HCC cells (Huh-7, unless otherwise specified) were embedded in low melting temperature agarose (Figure A1.1A). We confirmed the viability of cells following encapsulation with a Live/Dead viability reporter pair. Fluorescent staining following assay preparation confirmed cellular viability (Figure A1.1B) while cell death was observed following boiling of the preparation (Figure A1.1C).

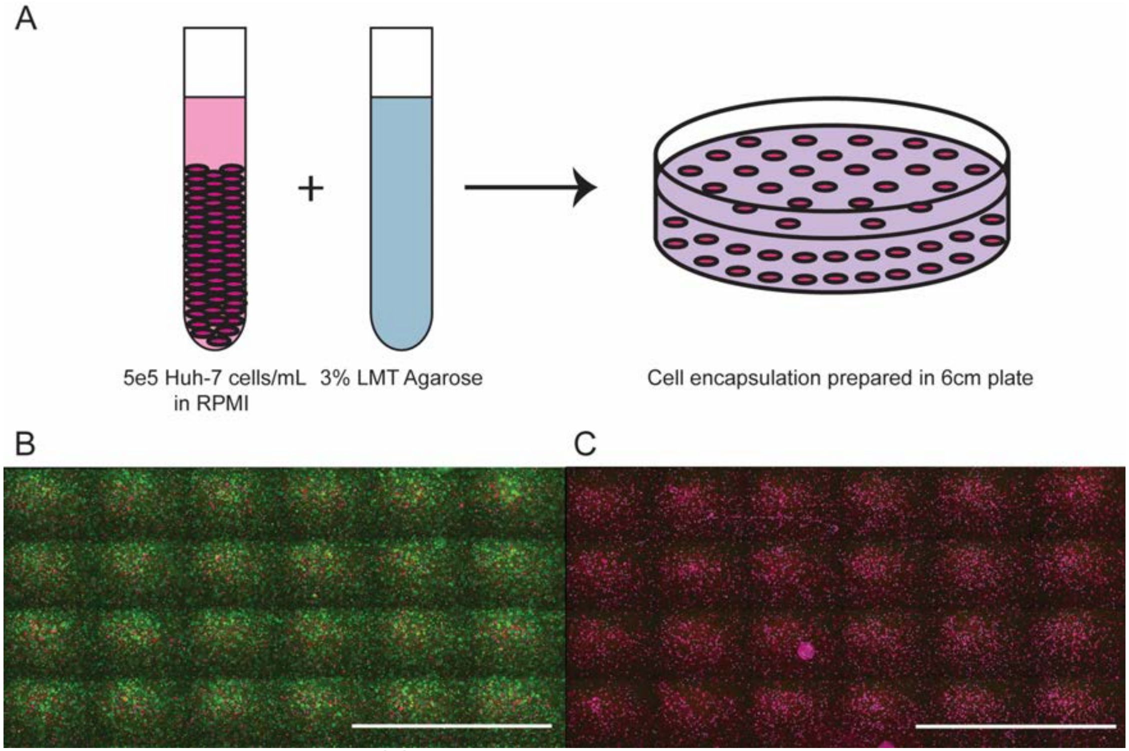
A
+
5e5 Huh-7 cells/mL in RPMI
3% LMT Agarose
Cell encapsulation prepared in 6cm plate
B
C

Figure A1.1: Model system: HCC cells embedded in low melting temperature agarose with viability assessment using a dual reporter assay
(A) The cell-encapsulation matrix was prepared as a 1:1 mixture of Huh-7 HCC cells and 3% low melting temperature agarose. (B) Staining with a pair of fluorescent viability reporters demonstrates that the encapsulation procedure does not impair cell viability (green fluorescence). [Scale bar = 5 mm] (C) Boiling of the preparation resulted in complete cell death (red fluorescence [recolored to appear magenta] in the absence of green fluorescence). [Scale bar = 5 mm]

Electrolytic ablation was performed by applying a direct current between two inert needle electrodes placed 1.5 cm apart within encapsulation assays prepared in 6 cm tissue culture dishes (Figure A1.2A, E). Initial investigation revealed that cell death occurred following ablation in the region surrounding both electrodes immediately following electrolytic ablation (Figure A1.2B). The total area of cell death was dependent upon the total time of ablation as well as the potential applied between the two electrodes.

Anode	22°C (n = 5, SD = 0)
Cathode	22°C (n = 5, SD = 0.45)
Midpoint of electrodes	22°C (n = 5, SD = 0.45)
Gel periphery	21°C (n = 5, SD = 0)

Table A1.1: Temperature measurements following electrolytic ablation reveal a temperature-independent mechanism of action
Temperature measurements were made immediately following ablation at four sites surrounding the two electrodes (Figure A1.2F).

For the subsequent analyses, ablations were performed at a potential of 10 V with an electrode spacing of 1.5 cm. The duration of electrolytic ablation and the applied voltage were selected to ensure that appreciable cell death was observed between the cathode and anode; these settings corresponded to a total charge deposition of 726 mC for 90 s ablations (n = 3, SD = 41 mC) (Figure A1.2B, A1.4K). At the viability margin, indicated by the fluorescent reporter pair, a corresponding change in the morphologic appearance of cells was appreciated on brightfield imaging where cells within the ablation margin appeared elongated, flattened, and pale in comparison to cells outside of this margin (Figure A1.2C, D). These results were recapitulated in two additional HCC cell lines, SNU-449 and HEPG2, for which no significant difference in ablation area was observed [F: 2.29 on 2 and 11 DF, p = 0.15] (Figure A1.S1).

Characterization of the mechanism of cell death

Prior work led us to hypothesize that the cell death pattern observed after electrolytic ablation could be a function of temperature, transmembrane potential, or local changes in pH[32,38–40]. To further elucidate the mechanism of cell death following electrolytic ablation, we measured and analyzed these parameters independently within our model system either during or immediately following an ablation (Table A1.1, Figure A1.3).

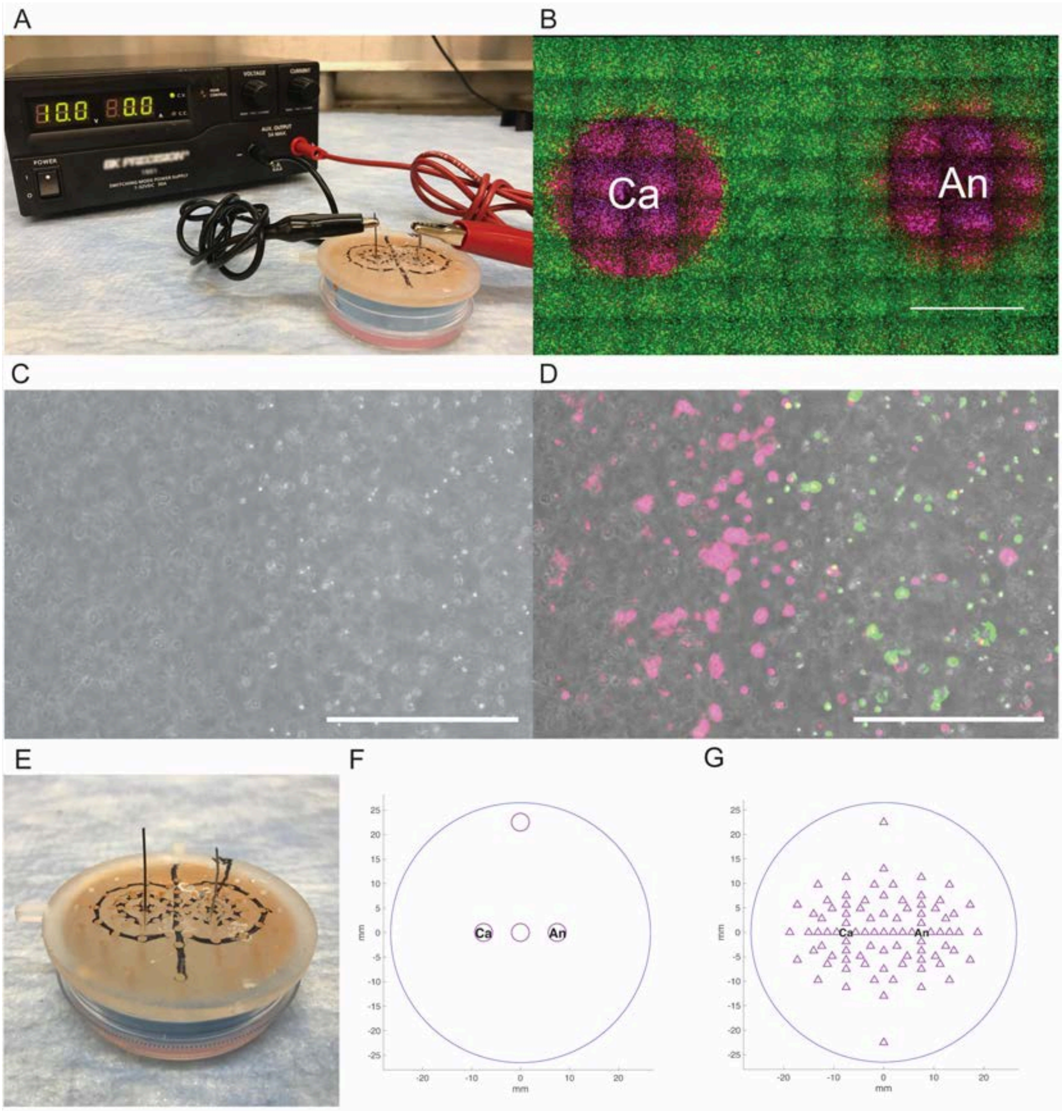

Figure A1.2: Cell encapsulation assay enables the spatial resolution of electrolytic ablation-induced changes in temperature, transmembrane potential, and pH
(A) Electrolytic ablation was performed by the application of direct current between a nitinol cathode (left) and platinum anode (right) held in place by a 3D-printed spacer sitting atop the cell encapsulation matrix that was cast in a 6 cm tissue culture dish. (B) Electrolytic ablation performed in this assay led to the observation of cell death in the regions surrounding the cathode (Ca) and anode (An). [Scale bar = 5 mm] (C, D) 10x magnification brightfield image with and without fluorescence reporter overlay at an increased cell density of 3 x 10^6 cells mL^{-1} to highlight changes at the border of the ablation zone. [Scale bar = 400 μm] (E) A custom insert was 3D-printed to sit atop the encapsulation assay prepared in a 6 cm dish. The insert holds the electrodes at a spacing of 1.5 cm and enables precise measurement of temperature, pH, and voltage potential (relative to the midpoint between the two electrodes). (F) Temperature measurement sites (circles). (G) pH and voltage potential measurement sites (triangles).

Measurements of temperature at the anode, cathode, electrode midpoint, and a control measurement site outside of the zone of ablation were all found to fall between 21°C and 23°C (Figure A1.2F, Table A1.1). Given the observation of cell death under these conditions without a corresponding change in temperature in the range expected of thermal ablation techniques, we concluded that temperature was not mechanistically responsible for the pattern of death observed[5,6,8]. This finding is consistent with prior work and distinguishes this ablation technique from thermal-dependent modalities[40].

Independent of temperature effects, transmembrane potential has been implicated as the cause of cell death in IRE with a transmembrane potential in excess of 1 V necessary to induce permanent membrane damage[12–15]. To calculate transmembrane potential, we first recorded the voltage potential at 85 sites surrounding the cathode and anode relative to the potential at the midpoint between the two electrodes (Figure A1.2E, G, A1.3A). Next, the magnitude of a linearly discretized potential gradient was interpolated from these recorded measurements across a distance equal to the cell diameter, 14.2 μm. The maximum recorded gradient was 12 mV and none of the regions of the cell encapsulation assay reached the threshold transmembrane potential of 1 V (Figure A1.3B). Taken together, the absence of temperature change and electroporation-range transmembrane potentials distinguishes the mechanism of cell death in electrolytic ablation from that observed in thermal-based ablation modalities or IRE.

Given prior work demonstrating that electrolysis can yield reactive oxygen species (ROS), we subsequently investigated the potential role of ROS-mediated cell death in a modified version of our cell encapsulation platform[33,44]. Consistent with this prior work, we observed the formation of ROS surrounding both the anode and cathode. Treatment with 5 mM n-acetylcysteine (NAC), an antioxidant, led to an 88% decrease in this ROS burden. Viability assessments revealed a 23% decrease in the area of cell death after ablation with

NAC treatment that did not reach statistical significance (t: 2.76 on 3.3 DF, p = 0.06) (Figure A1.S2). This suggests that ROS may contribute to the cell death observed following electrolytic ablation but is not the primary driver of this phenomenon.

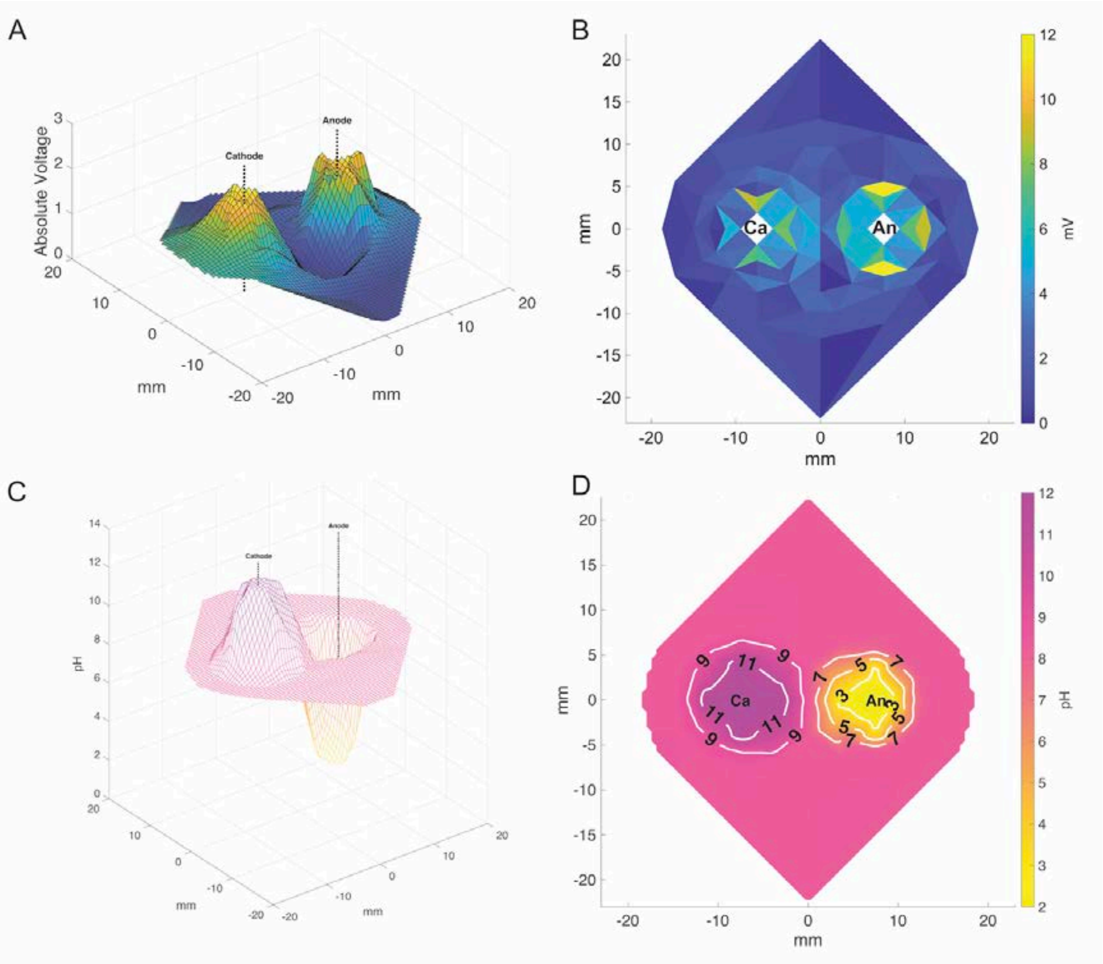

Figure A1.3: Measurement of voltage and pH in the encapsulation assay suggests the generation of acid and base as the mechanism of death following electrolytic ablation
(A) 3D surface plot of 2D linear interpolation of voltage potential measurements. (B) 2D linear interpolation contour plot of transmembrane potential calculated from voltage potential measurements via linear interpolation of the gradient magnitude across the width of an HCC cell. None of the regions of the assay reached the threshold voltage of 1 V necessary for electroporation. (C) 3D surface plot of 2D linear interpolation of pH measurements. (D) 2D linear interpolation contour plot of pH measurements recorded surrounding the cathode and anode, revealing basic changes surrounding the cathode [Ca] and acidic changes surrounding the anode [An].

In order to determine the primary driver of cell death following electrolytic ablation, we investigated the relationship of pH changes to the pattern of cell death in our assay. Measurements of pH were made immediately following ablation in 85 sites surrounding the anode and cathode (Figure A1.2E, G). Reduction at the cathode leads to the generation of base, primarily via the generation of hydroxide ions (A1.E1). Oxidation at the cathode leads to the generation of acidic species, primarily via the generation of hydronium ions (A1.E2). These pH changes were observed in our system and are consistent with prior *ex vivo* investigations of electrolytic ablation[31,38] (Figure A1.3C, D). Upon comparison to the viability data collected, we observed that pH contours paralleled the regions of cell death observed following viability staining of the cell encapsulation assay (Figure A1.3C, D, Figure A1.4).

Cathode half reaction: $2H_2O + 2e^- \rightarrow H_2 + 2OH^-$ (A1.E1)

Anode half reaction: $6H_2O \rightarrow 4H_3O^+ + O_2 + 4e^-$ (A1.E2)

Validation of pH modulation as the driver of cell death

To further examine the role of pH change in electrolytic ablation-mediated cell death and macroscopic tumor necrosis, we modified the buffering capacity of the encapsulation assay prior to ablation. Initial experiments were performed with a 10 mM concentration of HEPES, a buffering agent used in cell culture to maintain a physiologic pH. We increased this buffering capacity of the system by factors of 5 and 20, preparing cell encapsulation assays with final concentrations of 50 mM and 200 mM HEPES respectively, and repeated the measurements of pH and viability following electrolytic ablation (Figure A1.4). The area of cell death was found to be significantly different in the three conditions (F: 75.96 on 2 and 9 DF, $p < 1 \times 10^{-5}$). Increased buffering capacity led to a contraction of the region of cell death (Figure A1.4J). This change in viability correlated with a corresponding change in pH contours, whereby a reduced change in pH was associated with increased buffering capacity. Total charge delivery during electrolytic ablation also differed across the three experimental conditions, with increased buffering capacity leading to a reduced total charge delivery via an apparent increase in electrical impedance (F: 72.38 on 2 and 6 DF, $p < 1 \times 10^{-4}$; Figure A1.4K). Paired comparison of viability and pH data from the three conditions revealed the range of pH that was compatible with cellular viability. This range was observed to remain constant despite differences in the total ablated area following electrolytic ablation. pH above 10.6 (SD = 0.4) around the cathode or below 4.8 (SD = 0.6) around the anode was found to be incompatible with cellular viability (Table A1.2).

	Cathode Viability Boundary (pH)	Anode Viability Boundary (pH)
10 mM HEPES	11.0	4.6
50 mM HEPES	10.2	4.2
200 mM HEPES	10.7	5.4
	10.6 (SD = 0.4)	**4.8 (SD = 0.6)**

Table A1.2: Electrolytic ablation performed with differing buffering capacities reveals pH-dependent viability boundaries surrounding the two electrodes
The viability boundary for each experimental condition was calculated by determining the average pH along the boundary of an ellipse fitted to the viability images analyzed for each condition. pH below the level achieved at anode viability boundary or above the level achieved at the cathode viability boundary was found to induce cell death in the encapsulation assay.

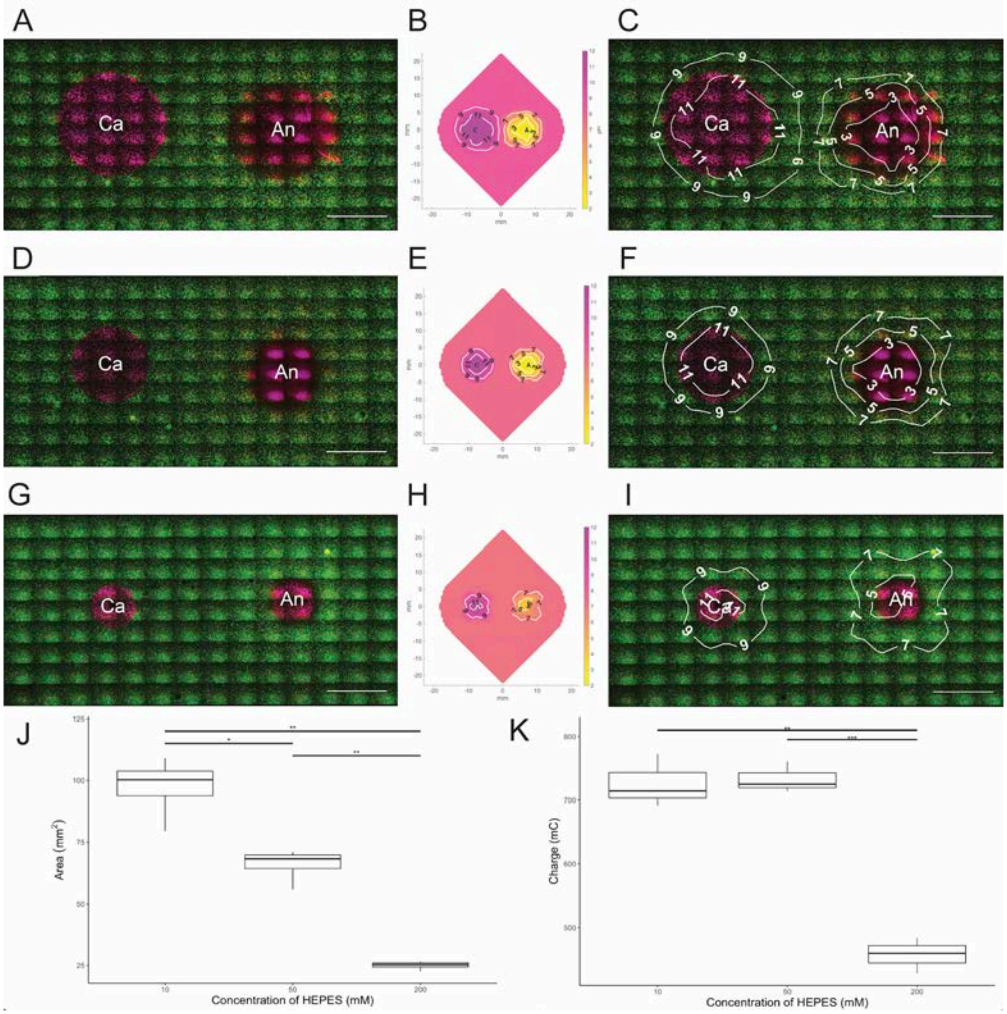

Figure A1.4: Modification of the buffering capacity confirms a pH-dependent mechanism of cell death in electrolytic ablation

(A, D, G) Viability images in the region surrounding the cathode and anode following electrolytic ablation with HEPES concentrations of 10 mM, 50 mM, and 200 mM. [Scale bar = 5 mm] (B, E, H) pH contour maps in the region surrounding the cathode and anode following electrolytic ablation with HEPES concentrations of 10 mM, 50 mM, and 200 mM. (C, F, I) pH contour maps overlaid upon viability images in the region surrounding the cathode and anode following electrolytic ablation with HEPES concentrations of 10 mM, 50 mM, and 200 mM, respectively. [Scale bar = 5mm] (J) Comparison of the total area of cell death in the three conditions reveals a decreasing area of cell death with increased assay buffering capacity (n = 4 for all tests; [ANOVA] F: 75.96 on 2 and 9 DF, p < 1 x 10-5; [10 mM v 50mM] t: 4.39 on 4.59 DF, Bonferroni adjusted p < .05; [10 mM v 200mM] t: 11.36 on 3.10 DF, Bonferroni adjusted p < .01; [50 mM v 200mM] t: 11.75 on 3.34 DF, Bonferroni adjusted p < .01) (K) Comparison of total charge deposition in the three conditions reveals a decreasing quantity of charge deposition with increased buffering capacity (n = 3 for all tests; [ANOVA] F: 72.38 on 2 and 6 DF, p < 1 x 10-4; [10 mM v 50mM] t: -0.25 on 3.25 DF, Bonferroni adjusted p: 1.0; [10 mM v 200mM] t: 9.36 on 3.48 DF, Bonferroni adjusted p < 0.01; [50 mM v 200mM] t: 12.95 on 3.95 DF, Bonferroni adjusted p < 0.001).

To examine the relative roles of pH and electrical charge in electrolytic ablation-induced cell death, we assessed the propagation of the ablation zone following the termination of the direct current application. While in the initial experiments, encapsulation assays were neutralized to a pH of 7.4 immediately prior to microscopy, we performed a subsequent experiment (n = 4) in which we allowed the assay to incubate at 37°C for 60 minutes before neutralizing and staining of the assay. Compared to the initial experimental condition, we observed an expansion in the total area of cell death consistent with diffusion of acidic and basic species in the absence of differences in electrical impedance or electric charge deposition (t: 7.32 on 3.42 DF, $p < 0.01$; Figure A1.5A). These findings indicate that electroosmosis is not responsible for cell death as the margins of the cellular necrosis propagate in the absence of an electric field. This propagation further supports the role of pH modulation as the primary driver electrolytic ablation-induced cell death as the expanded zone of cell death is consistent with the diffusion of acid and base generated at the electrodes.

Leveraging the pH-dependent mechanism for HCC treatment

A primary advantage of electrolytic ablation is the enhanced precision it provides to shape ablation margins for the treatment of complex tumor geometries. The described experiments demonstrate that cell death induced through pH modulation can propagate within the encapsulation assay by diffusion of acidic and basic species. By accounting for tissue electric resistance and buffering capacity, electrolytic ablation could be designed to tailor the diffusion of pH fronts to the boundaries of interest. To further facilitate enhanced precision and demonstrate the capacity of electrolytic ablation to shape an ablation zone, we next performed a multi-cathode ablation with eight cathodes surrounding a central anode. We observed regions of cell death surrounding each of the nine electrodes in the geometry prescribed by the electrode arrangement, thus confirming the potential to shape the ablation zone (Figure A1.5A, B).

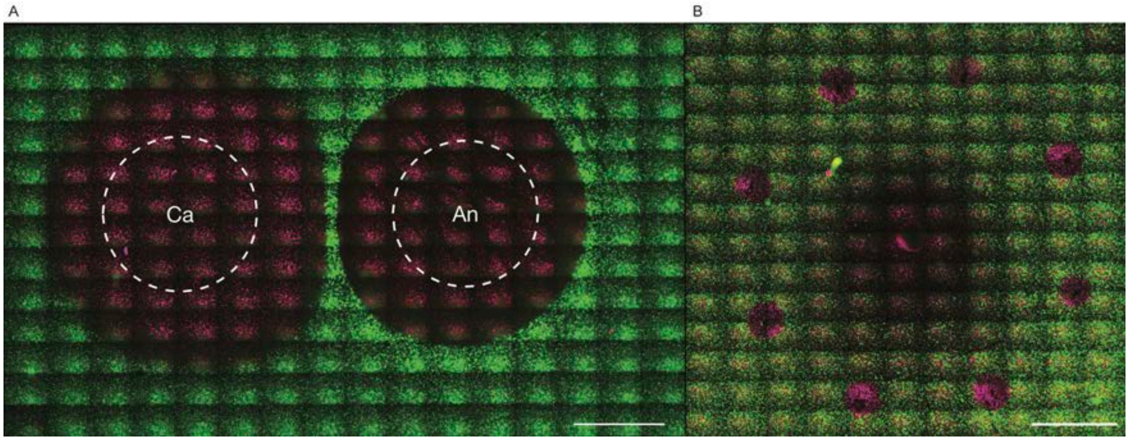

Figure A1.5: By permitting diffusion or using multiple cathodes, precise ablation geometries may be achieved with electrolytic ablation
(A) An increased area of cell death was observed after allowing 60 minutes of diffusion following electrolytic ablation (dashed white lines indicate ablation margin immediately after treatment; t: 7.32 on 3.4 DF, $p < 0.01$). [Scale bar = 5 mm] (B) A multi-cathode design allows the prescription of the volume in which cell death occurs as demonstrated by performing electrolytic ablation at 10 V for 10 seconds resulting in cell death surrounding the 9 electrodes. [Scale bar = 5 mm]

A1.5: Discussion

These results demonstrate that electrolytic ablation-mediated cell death results primarily from the introduction of toxic acid and base. This occurs without evidence of significant temperature change or sufficient transmembrane potential to induce cell rupture, confirming a unique mechanism of action and distinguishing electrolytic ablation as the only ablation technology to induce its therapeutic effect through alteration of the tumor microenvironment[32,38,39,45,46]. Though not statistically significant, the reduction in the area of cell death following electrolytic ablation performed in the presence of an antioxidant suggests a potential secondary role of ROS in electrolytic ablation-induced cell death. However, the relatively low magnitude of this change affirms pH as the primary driver of cell death during electrolytic ablation. Moreover, we demonstrate that a pH below

4.8 or above 10.6 is toxic to cancer cells, consistent with the range of pH changes observed in the region surrounding the cathode and anode in prior *in vitro* and *in vivo* studies[39,47]. The observation that increased buffering capacity led to the contraction of ablation zones in the setting of decreased charge deposition suggests that increased buffering capacity may slow ablation progress by increasing impedance. However, the observation that ablation proceeds following the cessation of electrolytic ablation in the absence of charge deposition underscores the primary role of pH modulation in causing cell death through the diffusion of acidic and basic species. This observation of expanding ablation zones in the absence of an electric field further confirms that cell death occurs independently of possible electroosmotic effects. Thus, the contraction of the ablation zone for assays with increased buffering capacity is due in part to the pH neutralizing the influence of the buffer. *In vivo,* it is expected that physiologic buffering will limit the spread of acidic and basic species following the completion of treatment. This implies that knowledge of tissue impedance and local buffering capacity may be leveraged to sculpt the zone of ablation.

Thermal ablation is a curative therapy for solitary, primary tumors and is a treatment of choice in HCC for patients who are not surgical candidates[48,49]. RFA is the most widely implemented modality; however, like other hyperthermic techniques, it has limited success for tumors greater than 3 cm in diameter[50,51]. The primary drawback of hyperthermic ablation is the heat sink phenomenon whereby traversing vessels lead to non-spherical ablation zones and the need for increased ablative power yields off-target effects on the nearby healthy tissue[52,53]. This limitation contributes more broadly to the risk of ablation failure, local tumor progression, and post-treatment recurrence. Existing hypothermic and non-thermal ablation modalities, including cryoablation and IRE, are not limited by this phenomenon but are associated with potentially serious side effects.

Cryoablation has been shown to precipitate a cryoshock phenomenon, a devastating condition that can lead to disseminated intravascular coagulation, acute respiratory distress syndrome, or liver failure [54]. IRE is technically difficult to perform and has the potential to induce cardiac arrhythmias and muscle contractions[5].

Electrolytic ablation represents a promising non-thermal ablation strategy that is immune to the heat sink effects that limit thermal approaches. It uses relatively low electric potentials compared to IRE, which may improve the expected side effect profile[5]. Moreover, we have demonstrated that electrolytic ablation enables the unique capability to sculpt the zone of ablation based upon the structure and arrangement of electrodes, permitting complex ablation margins with a single treatment. Clinically, this provides the potential to ablate lesions close to structures that may preclude heat-based ablation therapies—such as the gallbladder, porta hepatis, and bile ducts[32]. According to a model developed through simulations of pH front tracking, future work will be directed at developing a closed-loop system that evaluates ablation progress as a function of delivered charge and measured tissue impedance[31,39,42]. This may hold important implications for the implementation of gene electrotransfer, where knowledge of pH front patterns is necessary to optimize delivery[42].

The primary limitation of the present work is that it was conducted in an *in vitro* tissue culture assay. As a result, *in vivo* ablations may not take place under the voltage, current, and temporal parameters described herein. In the present study, when buffering capacity was increased, deposited charge decreased for equivalent ablation lengths (Figure A1.4). The extent of physiologic buffering and electrical resistance encountered *in vivo* may increase the duration of ablation required. Finally, the described assays do not assess the effect of tumor vasculature on ablation effectiveness. The flow of blood through a tissue may reduce the extent of ablation due to the delivery of additional buffering species and removal of generated acidic and basic ions. As such, the impact of blood flow *in vivo* is an important consideration for future translation.

In summary, we demonstrate that electrolytic ablation generates tumor cell kill through modulation of the tumor microenvironment primarily involving a pH-dependent mechanism that mitigates the limitations of leading ablation modalities. Our data further demonstrate a pH-threshold viability phenomenon wherein cancer cells placed in an environment at a pH below 4.8 or above 10.6 undergo cell death. These unique insights will be essential for leveraging cancer cell susceptibility to altered microenvironments as well as furthering the development of electrolytic ablation for clinical application.

A1.6: Methods

Cell encapsulation

All studies were conducted with Huh-7, HepG2 or SNU-449 HCC cells grown to confluence with RPMI growth medium. Using 0.25% trypsin, cells were brought into a single cell suspension at a concentration of 5e5 cells mL^{-1}. A homogenous 3% solution of low melting temperature agarose (Sigma A4018 2-Hydroxyethylagarose; Type VII) in water was prepared by heating. When the agarose cooled to a temperature of 45°C, a 4 mL 1:1 mixture of cell suspension in RPMI and low melting temperature agarose was cast in 6 cm cell culture plates at room temperature. Initial mechanistic evaluation experiments were performed with a total HEPES concentration of 10 mM. Subsequent experiments included conditions with final HEPES concentrations of 50 mM or 200 mM.

Electrolytic ablation

Ablations were performed within the cell encapsulation assay between a platinum anode (Surepure Chemetals #1981, 0.5 mm diameter) and nitinol cathode (Alfa

Aesar 44950G6, 0.5 mm diameter) at an electrode spacing of 1.5 cm. For the experiment described in Figure A1.5, 8 cathodes were radially oriented around a central anode at a radius of 1 cm. Ablations were performed using a BK Precision® 1901 D.C. power supply set to a constant potential of 10 V. All ablations were performed for 90 seconds, with the exceptions of those performed for evaluation of ROS (45 seconds) and evaluation of diffusion (10 seconds).

Viability assessment

Viability was assessed and quantified with the ThermoFisher LIVE/DEAD® Viability/Cytotoxicity Kit, for mammalian cells (L3224). Conversion of non-fluorescent, cell-permeable calcein AM to green-fluorescent calcein by intracellular esterases distinguishes living cells. Dead cells are distinguished by a red fluorescence when Ethd-1 enters cells with damaged membranes and binds to nucleic acid.

Following electrolytic ablation, 3 mL of 1M HEPES (pH = 7.4) was added on top of the cell encapsulation gels, which were then incubated for 30 minutes at 37°C to allow for equilibration, that was verified with the pH probe described below. Upon removal of the buffer, 550 μL of staining solution composed of 2 μM calcein AM and 4 μM EthD-1 suspended in phosphate-buffered saline (PBS) was added to the gels, which were again incubated for 30 minutes at 37°C. Fluorescence imaging was then performed on a Leica DMI6000B inverted light and fluorescent microscope. Using tiled acquisition, a series of fluorescence images were taken to capture the viability of the area surrounding both electrodes. Raw image files were prepared for quantification using Adobe Photoshop. Identical modifications were made to all acquired images. Quantification of the area of necrosis in the different experimental conditions was performed using ImageJ software.

For the reported analyses, there were 4 replicates of each of the 10 mM, 50 mM, and 200 mM HEPES conditions. There were three replicates of the assessment of viability in the presence or absence of NAC. The brightfield and corresponding fluorescence images of Figure A1.2C & A1.2D were acquired using a ThermoFisher EVOS FL Cell Imaging System. Green/red fluorescence was recolored green/magenta using Adobe Photoshop for use in the presented figures.

pH measurement

To determine the potential impact of pH on cellular viability in the described experiments, pH measurements were collected from 85 sites surrounding the two electrodes immediately following electrolytic ablation using a 3D printed part. pH was measured with the Orion™ 9863BN Micro pH Electrode (ThermoFisher) on an A211 Benchtop meter (ThermoFisher). Immediately following electrolytic ablation, the pH probe was used to measure the pH of up to 10 sites. Given the concern for rapid pH changes secondary to diffusion, measurements of pH within a single assay were performed within the first minute following the conclusion of ablation. This process was repeated on multiple assays to sample all 85 points described at least twice for each of the three experimental conditions.

Local voltage and transmembrane potential

Analogous to pH measurements, voltage potentials within the cell encapsulation assay were collected from 85 sites surrounding the two electrodes. Voltage recordings were taken on the Peakmeter PM18C multimeter relative to the platinum anode with a second nitinol needle electrode. At the time of voltage measurement, the two electrodes of the assay were connected to the 10 V power supply. Up to 10 measurements were collected from each assay, and all 85 sites were sampled at least four times. Raw measurements of potential were then re-centered around the midpoint connecting the two electrodes. The magnitude of this re-centered measurement has been reported as the potential of a site within the assay relative to the midpoint between the two electrodes. Transmembrane potential was estimated by 2D linear interpolation of voltage between measured points followed by numerical calculation of gradient magnitude over a distance corresponding to the average diameter of a cell used in the encapsulation assay, 14.2 μm. This size was determined using a Countess II FL Automated Cell Counter.

Current measurement

Current measurements were acquired with the TACKlife DM01M digital multimeter. Measurements of current were recorded every 10 s during electrolytic ablation and the total charge delivered was subsequently calculated. These measurements were repeated three times for each experimental condition.

Temperature measurement

The temperature was recorded using the Peakmeter PM18C multimeter. Measurements of temperature were taken immediately following electrolytic ablation at the anode, cathode and the midpoint connecting the two electrodes. These measurements were repeated five times for the baseline experimental condition (10 mM HEPES, Huh7 cells).

Reactive oxygen species (ROS) assessment

Huh7 cells were grown and encapsulated as described above with the exception that 2 mLs, as opposed to 4 mLs, of the 1:1 mixture of encapsulated cells was plated onto

6 cm plates. Control plates were prepared with 1 mM H_2O_2 in PBS (positive control), 1 mM H_2O_2 with 5 mM n-acetyl cysteine (NAC) in PBS (negative control), or bland PBS (negative control) and were then incubated at 37°C for 30 minutes. Subsequently, CellRox® Green (Invitrogen, Carlsbad, CA) was added to the PBS fraction at a final concentration of 17.5 µM. The plate was gently agitated and incubated at 37°C for 30 minutes. The liquid was aspirated and replaced with PBS, followed by a 15 minute incubation at 37°C. Finally, the liquid was aspirated and replaced with PBS.

To evaluate ROS generation, electrolytic ablation was performed at a potential of 10 V for 45 seconds. Prior to electrolytic ablation, assays were pre-incubated with 1 mL of PBS with or without 5 mM NAC and these solutions were aspirated prior to ablation. Immediately after electrolytic ablation, assays were incubated in 3 mL of 1M HEPES (pH = 7.4). After equilibration, this solution was replaced with 1 mL of PBS supplemented with CellRox® Green to a final concentration of 17.5 µM with 5 mM NAC for those which had previously received NAC. Plates were incubated at 37°C for 30 minutes. Assays were then washed once with PBS at 37°C for 30 minutes. There were three replicates of the assessment of ROS in the presence or absence of NAC.

Fluorescence imaging was then performed on a Leica DMI6000B inverted light and fluorescent microscope. Using tiled acquisition, a series of fluorescence images were taken to capture the ROS in the area surrounding both electrodes. Raw image files were prepared for quantification using Adobe Photoshop. Identical modifications were made for all acquired images. For the reported analyses, fluorescence from the areas corresponding to both electrodes was compared with respect to the background of the image excluding the areas of the electrodes as a log fold change. This quantification was performed using ImageJ software.

Statistical analyses and figure generation

Statistics were performed in R. T-tests between conditions were performed with two-tails assuming unequal variance between the different conditions with a Bonferroni correction for multiple t-tests. The results of F-tests and t-tests are reported above with corresponding statistics, degrees of freedom, and p-values. Quantitative displays were prepared in R and Matlab, with use of the export_fig plug-in <https://www.mathworks.com/matlabcentral/fileexchange/23629-export-fig>. Figures were compiled using Adobe Illustrator. Adobe Photoshop was used to insert pH map overlays produced in Matlab.

A1.7: Supplementary Figures

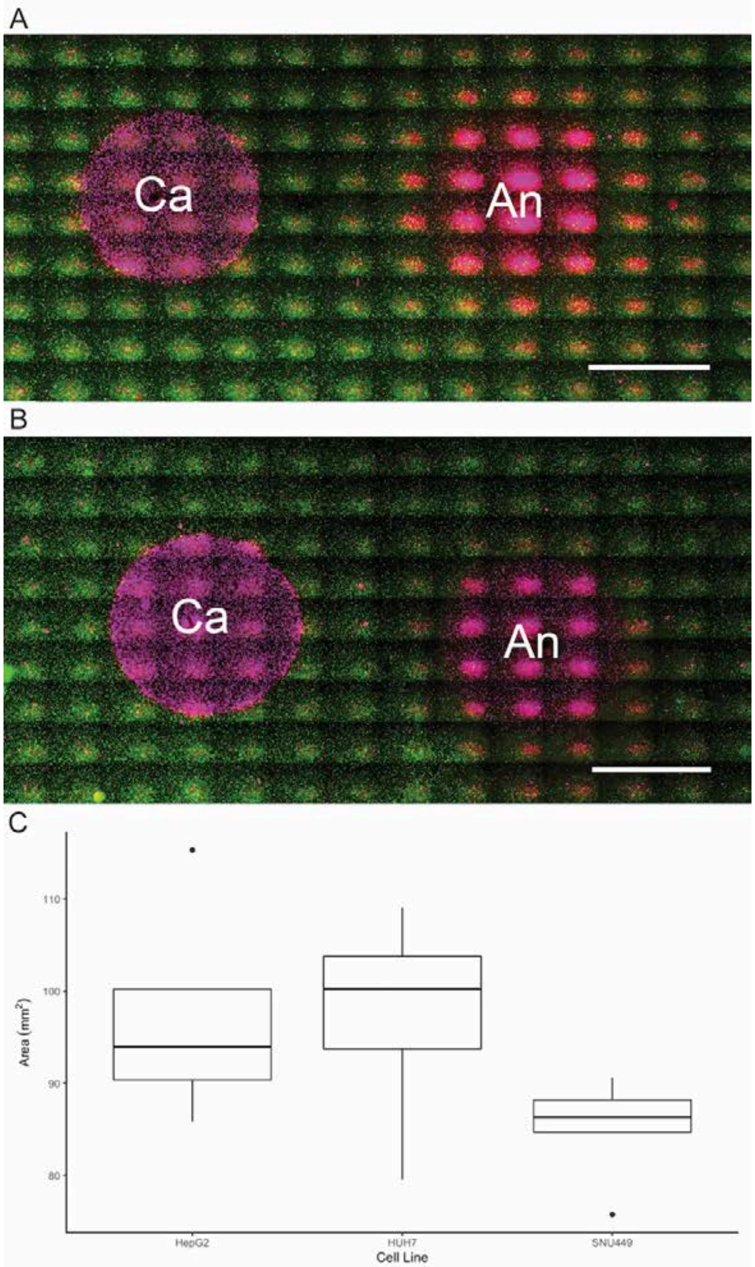

Figure A1.S1: Electrolytic ablation is found to induce cell death in multiple HCC cell lines (A) Electrolytic ablation demonstrates evidence of cell death surrounding the cathode (Ca) and anode (An) in SNU-449 cells [Scale bar = 5 mm]. (B) Electrolytic ablation demonstrates evidence of cell death surrounding the cathode (Ca) and anode (An) in HepG2 cells [Scale bar = 5 mm]. (C) Comparison of the area of cell death observed in three HCC cell lines reveals no significant difference in response to electrolytic ablation (F: 2.29 on 2 and 11 DF, p = 0.15).

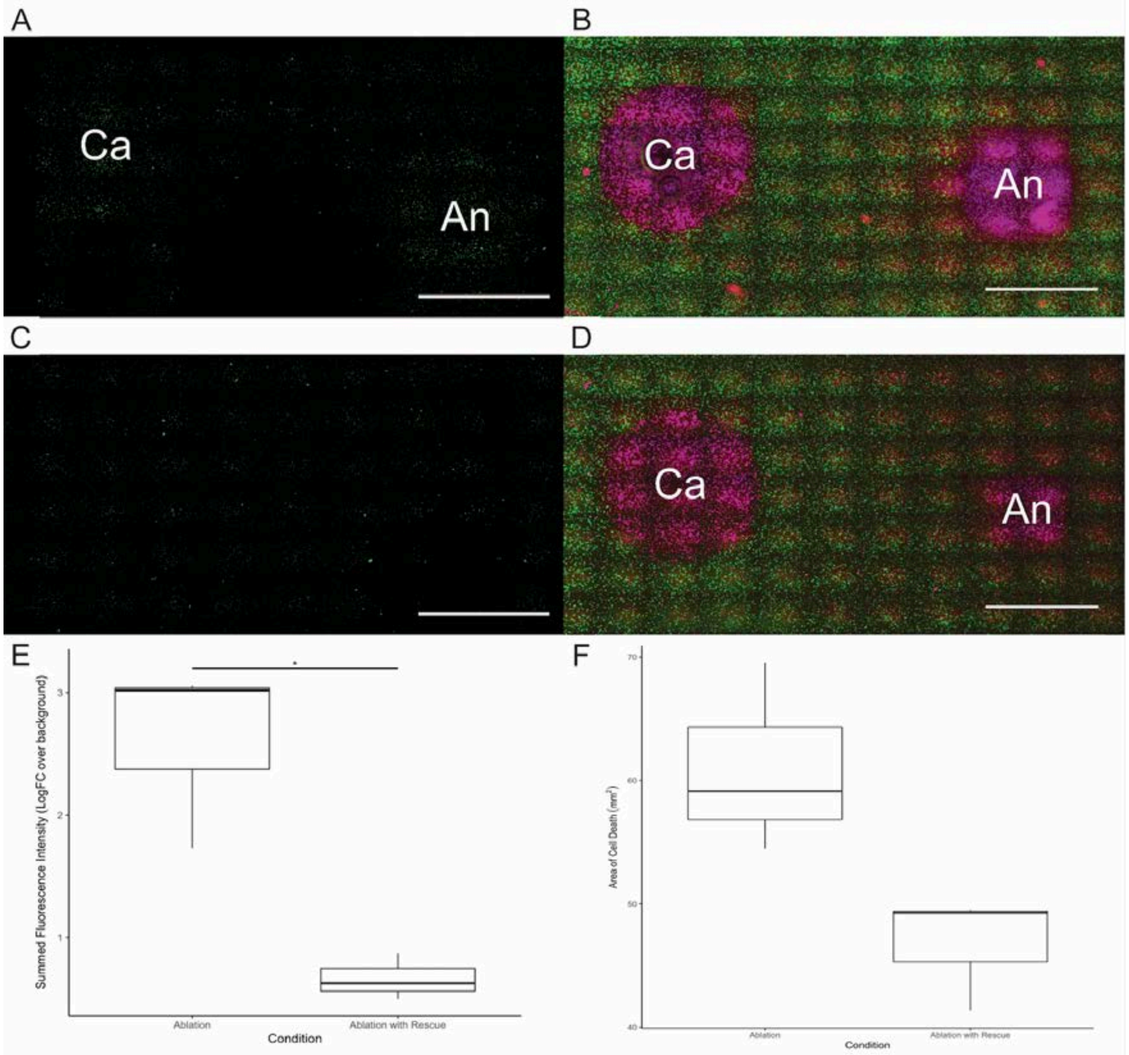

Figure A1.S2: Reactive oxygen species are present following electrolytic ablation
(A) Following electrolytic ablation, assays stained with CellRox® Green demonstrated areas of fluorescence in the regions surrounding the cathode (Ca) and anode (An), suggesting the presence of ROS. [Scale bar = 5 mm] (C) Exposure to 5 mM NAC, an antioxidant, reduced the amount of fluorescence detected from the regions surrounding the electrodes. [Scale bar = 5 mm] (B, D) Viability staining with Calcein/Ethd-1 reveals cell death in the absence (B) or presence (D) of NAC. [Scale bar = 5 mm] (E) Summed fluorescence intensity around the two electrodes, compared according to the natural log fold change with respect to the background of the image, demonstrated a significant decrease in ROS detection (t: 4.32 on 2.2 DF, $p < 0.05$). (F) The mean area of cell death observed after electrolytic ablation following rescue with NAC decreased by 23%, though this change did not reach statistical significance (t: 2.76 on 3.3 DF, $p = 0.06$).

A1.8: References

1. Perkons, N. R. *et al.* Electrolytic ablation enables cancer cell targeting through pH modulation. *Commun. Biol.* **1**, 1–10 (2018).
2. Stein, E. J. *et al.* Magnetic Resonance Imaging Enables Real-Time Monitoring of In Vitro Electrolytic Ablation of Hepatocellular Carcinoma. *J. Vasc. Interv. Radiol.* **31**, Manuscript Accepted for Pub (2019).
3. Chu, K. F. & Dupuy, D. E. Thermal ablation of tumours: biological mechanisms and advances in therapy. *Nat. Rev. Cancer* **14**, 199–208 (2014).
4. Allaire, M. & Nault, J. Advances in management of hepatocellular carcinoma. **29**, 288–295 (2017).
5. Knavel, E. M. & Brace, C. L. Tumor ablation: Common modalities and general practices. *Tech. Vasc. Interv. Radiol.* **16**, 192–200 (2013).
6. Nikfarjam, M., Muralidharan, V. & Christophi, C. Mechanisms of focal heat destruction of liver tumors. *J. Surg. Res.* **127**, 208–223 (2005).
7. Vroomen, L. G. P. H., Petre, E. N., Cornelis, F. H., Solomon, S. B. & Srimathveeravalli, G. Irreversible electroporation and thermal ablation of tumors in the liver, lung, kidney and bone: What are the differences? *Diagn. Interv. Imaging* **98**, 609–617 (2017).
8. Overgaard, J. & Suit, H. D. Time-temperature relationship th hyperthermic treatment of malignant and normal tissue in vivo. *Cancer Res.* **39**, 3248–3253 (1979).
9. Gage, A. A. & Baust, J. Mechanisms of tissue injury in cryosurgery. *Cryobiology* **37**, 171–186 (1998).
10. Faroja, M. *et al.* Irreversible electroporation ablation: is all the damage nonthermal? *Radiology* **266**, 462–470 (2013).
11. Miller, L., Leor, J. & Rubinsky, B. Cancer cells ablation with irreversible electroporation. *Technol. Cancer Res. Treat.* **4**, 699–705 (2005).
12. Davalos, R. V., Mir, L. M. & Rubinsky, B. Tissue ablation with irreversible electroporation. *Ann. Biomed. Eng.* **33**, 223–231 (2005).
13. Bastianpillai, C. *et al.* Harnessing the immunomodulatory effect of thermal and non-thermal ablative therapies for cancer treatment. *Tumor Biol.* **36**, 9137–9146 (2015).
14. Kurata, K., Matsushita, M., Yoshii, T., Fukunaga, T. & Takamatsu, H. Effect of irreversible electroporation on three-dimensional cell culture model. *Conf. Proc. IEEE Eng. Med. Biol. Soc.* **2012**, 179–82 (2012).
15. Zimmermann, U. & Neil, G. A. *Electromanipulation of Cells*. (1996).
16. Thomson, K. R. *et al.* Investigation of the safety of irreversible electroporation in humans. *J. Vasc. Interv. Radiol.* **22**, 611–621 (2011).
17. Adeyanju, O., Al-Angari, H. & Sahakian, A. The optimization of needle electrode number and placement for irreversible electroporation of hepatocellular carcinoma. *Radiol. Oncol.* **46**, 126–135 (2012).
18. Mir, L. M. Bases and rationale of the electrochemotherapy. *Eur. J. Cancer, Suppl.* **4**, 38–44 (2006).
19. Orlowski, S., Belehradek, J., Paoletti, C. & Mir, L. M. Transient electropermeabilization of cells in culture. Increase of the cytotoxicity of anticancer drugs. *Biochem. Pharmacol.* **37**, 4727–4733 (1988).
20. Mir, L. M., Banoun, H. & Paoletti, C. Introduction of definite amounts of nonpermeant molecules into living cells after electropermeabilization: Direct access to the cytosol. *Exp. Cell Res.* **175**, 15–25 (1988).

21. Ciria, H. *et al.* Antitumor effects of electrochemical treatment. *Chinese J. Cancer Res.* **25**, 223–234 (2013).
22. Nilsson, E. *et al.* Electrochemical treatment of tumours. *Bioelectrochemistry Bioenerg.* **51**, 1–11 (2000).
23. Ge, B. H. *et al.* Magnetic Resonance-Monitored Coaxial Electrochemical Ablation--Preliminary Evaluation of Technical Feasibility. *J. Vasc. Interv. Radiol.* **26**, 1238–46 (2015).
24. Von Euler, H., Nilsson, E., Olsson, J. M. & Lagerstedt, A. S. Electrochemical treatment (EChT) effects in rat mammary and liver tissue. In vivo optimizing of a dose-planning model for EChT of tumours. *Bioelectrochemistry* **54**, 117–124 (2001).
25. Wemyss-Holden, S. A., Dennison, A. R., Finch, G. J., De La Hall, P. M. & Maddern, G. J. Electrolytic ablation as an adjunct to liver resection: Experimental studies of predictability and safety. *Br. J. Surg.* **89**, 579–585 (2002).
26. Wang, H. Electrochemical therapy of 74 cases of liver cancer. *Eur. J. Surgery. Suppl.* **574**, 55–7 (1994).
27. Xin, Y. *et al.* Electrochemical treatment of lung cancer. *Bioelectromagnetics* **18**, 8–13 (1997).
28. Wu, G., Zhou, X. & Huang, M. Electrochemical therapy and implanted ports treatment for unresectable carcinoma of body and tail of pancreas. *Chinese J. Surg.* **39**, 596–8 (2001).
29. Yen, Y. *et al.* Electrochemical treatment of human KB cells in vitro. *Bioelectromagnetics* **20**, 34–41 (1999).
30. Kotnik, T. & Miklavčič, D. Theoretical Evaluation of Voltage Inducement on Internal Membranes of Biological Cells Exposed to Electric Fields. *Biophys. J.* **90**, 480–491 (2006).
31. Nilsson, E. & Fontes, E. Mathematical modelling of physicochemical reactions and transport processes occurring around a platinum cathode during the electrochemical treatment of tumours. *Bioelectrochemisty* **53**, 213–224 (2001).
32. Ge, B. H. *et al.* Magnetic resonance-monitored coaxial electrochemical ablation - Preliminary evaluation of technical feasibility. *J. Vasc. Interv. Radiol.* **26**, 1238–1246 (2015).
33. von Euler, H., Söderstedt, A., Thörne, A., Olsson, J. M. & Yongqing, G. Cellular toxicity induced by different pH levels on the R3230AC rat mammary tumour cell line. An in vitro model for investigation of the tumour destructive properties of electrochemical treatment of tumours. *Bioelectrochemistry* **58**, 163–70 (2002).
34. Vijh, A. Phenomenology and Mechanisms of Electrochemical Treatment (ECT) of Tumors. *Mod. Asp. Electrochem.* **39**, 231–274 (2006).
35. Czymek, R. *et al.* Intrahepatic radiofrequency ablation versus electrochemical treatment in vivo. *Surg. Oncol.* **21**, 79–86 (2012).
36. Veiga, V. F. *et al.* Exposure of human leukemic cells to direct electric current: generation of toxic compounds inducing cell death by different mechanisms. *Cell Biochem. Biophys.* **42**, 61–74 (2005).
37. Ciria, H. & González, M. Antitumor effects of electrochemical treatment. *Chinese J. …* **25**, 223–234 (2013).
38. Nilsson, E., Berendson, J. & Fontes, E. Impact of chlorine and acidification in the electrochemical treatment of tumours. 1321–1333 (2000).
39. Turjanski, P. *et al.* pH front tracking in the electrochemical treatment (EChT) of tumors: Experiments and simulations. *Electrochim. Acta* **54**, 6199–6206 (2009).

40. Olaiz, N. *et al.* Electrochemical treatment of tumors using a one-probe two-electrode device. *Electrochim. Acta* **55**, 6010–6014 (2010).
41. Phillips, M., Krishnan, H., Raju, N. & Rubinsky, B. Tissue Ablation by a Synergistic Combination of Electroporation and Electrolysis Delivered by a Single Pulse. *Ann. Biomed. Eng.* **44**, 3144–3154 (2016).
42. Marino, M. *et al.* pH fronts and tissue natural buffer interaction in gene electrotransfer protocols. *Electrochim. Acta* **255**, 463–471 (2017).
43. Luján, E. *et al.* Optimal dose-response relationship in electrolytic ablation of tumors with a one-probe-two-electrode device. *Electrochim. Acta* **186**, 494–503 (2015).
44. Guitaya, L., Drogui, P. & Blais, J. F. In situ reactive oxygen species production for tertiary wastewater treatment. *Environ. Sci. Pollut. Res.* **22**, 7025–7036 (2015).
45. Czymek, R. *et al.* Intrahepatic radiofrequency ablation versus electrochemical treatment Ex vivo. *J. Surg. Res.* **174**, 106–113 (2012).
46. Gravante, G. *et al.* Changes in acid-base balance during electrolytic ablation in an ex vivo perfused liver model. *Am. J. Surg.* **204**, 666–670 (2012).
47. Li, K. *et al.* Effects of direct current on dog liver: possible mechanisms for tumor electrochemical treatment. *Bioelectromagnetics* **18**, 2–7 (1997).
48. Wells, S. A. *et al.* Liver Ablation: Best Practice. *Radiol. Clin. North Am.* **53**, 933–971 (2015).
49. Llovet, J. M., Bru, C. & Bruix, J. Prognosis of hepatocellular carcinoma: the BCLC staging classification. *Semin. Liver Dis.* **19**, 329–338 (1999).
50. Kim, Y. sun, Rhim, H., Cho, O. K., Koh, B. H. & Kim, Y. Intrahepatic recurrence after percutaneous radiofrequency ablation of hepatocellular carcinoma: Analysis of the pattern and risk factors. *Eur. J. Radiol.* **59**, 432–441 (2006).
51. Bruix, J., Gores, G. J. & Mazzaferro, V. Hepatocellular carcinoma: clinical frontiers and perspectives. *Gut* **63**, 844–855 (2014).
52. Lu, D. S. K. *et al.* Influence of Large Peritumoral Vessels on Outcome of Radiofrequency Ablation of Liver Tumors. *J. Vasc. Interv. Radiol.* **14**, 1267–1274 (2003).
53. Yu, N. C. *et al.* Microwave Liver Ablation: Influence of Hepatic Vein Size on Heat-sink Effect in a Porcine Model. *J. Vasc. Interv. Radiol.* **19**, 1087–1092 (2008).
54. Chapman, W. C. *et al.* Hepatic cryoablation, but not radiofrequency ablation, results in lung inflammation. *Ann. Surg.* **231**, 752–61 (2000).